nature neuroscience

Article

https://doi.org/10.1038/s41593-025-01973-8

Myelin–axon interface vulnerability in Alzheimer's disease revealed by subcellular proteomics and imaging of human and mouse brain

Received: 5 October 2023

Accepted: 4 April 2025

Published online: 13 June 2025

Check for updates

Yifei Cai[1] ✉, Iguaracy Pinheiro-de-Sousa[2,17], Mykhaylo Slobodyanyuk[3,4,17], Fuyi Chen[1,17], Tram Huynh[1], Jean Kanyo[5], Peiyang Tang[1], Lukas A. Fuentes[6], Amber Braker[7], Rachel Welch[7], Anita Huttner[8], Lei Tong[1], Peng Yuan[1,16], TuKiet T. Lam[5,9,10], Evangelia Petsalaki[2], Jüri Reimand[3,4,11], Angus C. Nairn[10,12,13] & Jaime Grutzendler[1,14,15] ✉

Myelin ensheathment is essential for rapid axonal conduction, metabolic support and neuronal plasticity. In Alzheimer's disease (AD), disruptions in myelin and axonal structures occur, although the underlying mechanisms remain unclear. We implemented proximity labeling subcellular proteomics of the myelin–axon interface in postmortem human brains from AD donors and 15-month-old male and female 5XFAD mice. We uncovered multiple dysregulated signaling pathways and ligand–receptor interactions, including those linked to amyloid-β processing, axonal outgrowth and lipid metabolism. Expansion microscopy confirmed the subcellular localization of top proteomic hits and revealed amyloid-β aggregation within the internodal periaxonal space and paranodal/juxtaparanodal channels. Although overall myelin coverage is preserved, we found reduced paranode density, aberrant myelination and altered paranode positioning around amyloid-plaque-associated dystrophic axons. These findings suggest that the myelin–axon interface is a critical site of protein aggregation and disrupted neuro-glial signaling in AD.

Oligodendrocytes ensheath axons with myelin to enable efficient conduction of electrical signals and support axonal metabolism[1,2]. Myelination is a life-long dynamic process[3,4] essential for neuronal plasticity, learning and memory[5–8]. Myelin disruption contributes to the pathogenesis of various neurological disorders[9]. In Alzheimer's disease (AD), recent single-cell transcriptomics and bulk proteomics studies have highlighted oligodendrocyte and myelin pathology as important contributors to disease progression[10–19].

Myelin features specialized domains, including the internode, juxtaparanode and paranode[1,20–22]. The myelin–axon interface includes the cytosolic compartment of the myelin inner loops and the periaxonal space[23,24]. Unlike compact myelin, these compartments are rich in ion channels, transporters and neurotransmitter receptors[1] and play critical roles in metabolic support and axonal–glial interactions[23]. However, how these myelin compartments and their axonal interactions are disrupted in AD remains unclear.

In this study we present a comprehensive subcellular proteomics and imaging investigation of the myelin–axon interface. We developed an antibody-based proximity labeling proteomics workflow in postmortem AD brains, enabling precise molecular characterization of

A full list of affiliations appears at the end of the paper. ✉e-mail: yifei.cai@yale.edu; jaime.grutzendler@yale.edu

paranodes and internodes with high cell-type and subcellular specificity. Using computational and integrated pathway analysis, we identified ligand–receptor pairs and signaling pathways enriched at the myelin–axon interface in AD. We uncovered striking abnormalities in the distribution of proteins involved in AD-associated dysregulated signaling, including amyloid processing, axonogenesis and lipid metabolism, revealing a complex interplay between amyloid pathology, axonal remodeling and metabolic perturbations at the myelin–axon interface.

Using expansion microscopy (ExM), we revealed the subcellular localization of key proteomic hits at myelin and axons in AD brains. We also observed distinct amyloid deposition patterns, including spiral fibers around axons and dense helical coils at paranodal/juxtaparanodal loops, indicating amyloid infiltration within the myelin–axon interface at paranodes, juxtaparanodes and internodes. Additionally, we found aberrant myelination and disrupted paranodes on amyloid-plaque-associated dystrophic axons, a hallmark of AD known to impair action potential conduction and disrupt neuronal networks[25]. Despite no significant difference in overall myelin coverage, we noted greater paranode loss in AD brains compared with age-matched controls, consistent with our reanalysis of recent transcriptomic and proteomic datasets, indicating dysregulation of myelin-related signaling rather than a net loss of myelin.

Altogether, this study uncovered the subcellular molecular architecture of the myelin–axon interface, shedding light on molecular and cellular mechanisms that may drive myelin and axon disruption in AD. These findings and associated datasets will serve as valuable resources for future mechanistic and therapeutic investigations into myelin–axonal interactions in health and disease.

Results

Paranode pathology in the absence of myelin loss in the AD human frontal cortex

Myelin abnormalities are a key feature of brain aging and AD[4,26–30]. Recent transcriptomics and proteomics studies in postmortem AD human brains have revealed unique oligodendrocyte and myelin changes[10,11,14,16]. We reanalyzed four recent datasets from the AD human frontal cortex[10,11,14,16] and found that despite dysregulation in various oligodendrocyte and myelin proteins, the messenger RNA and protein levels of major markers (PLP1, CNP and MBP) remained largely unchanged between AD and age-matched controls (Extended Data Fig. 1). This suggests that AD pathology may disrupt myelin structure and function without overt myelin loss.

To further investigate this, we implemented an artificial intelligence (AI)-guided quantitative imaging pipeline to analyze tens of thousands of myelin internodes and paranodes in postmortem human brain (Fig. 1a, Supplementary Fig. 1 and Supplementary Video 1). We performed immunofluorescence confocal imaging of frontal cortex, assessing myelin (PLP1), axons (SMI312) and paranodes (contactin associated protein 1 (CASPR)), followed by high-confidence segmentation of individual structures for density and size quantification (Fig. 1a–c,f,g,j). Our analysis revealed no significant differences in myelin or axon density between AD and control brains, whether measured through segmentation (Fig. 1d,h) or mean fluorescence intensity (Fig. 1e,i). These results align with our reanalysis of published transcriptomic and proteomic data, showing no major changes in key myelin proteins (Extended Data Fig. 1)[10,11,14,16].

In contrast to the unchanged myelin coverage, CASPR immunofluorescence revealed a significant reduction in paranode density (Fig. 1j–l) and enlargement of paranodes (Fig. 1m–o) in AD humans. Notably, paranodes near amyloid deposits exhibited distinct morphological alterations, with increased separation between CASPR staining layers compared with their more linear pattern in controls (Fig. 1n), suggesting paranodal myelin decompaction and/or underlying axonal enlargement. Consistent with human findings, 5XFAD mice displayed similar amyloid-associated myelin changes (Fig. 1p and Extended Data Fig. 2), with overall myelin quantity remaining unchanged in the cortex and hippocampus (Fig. 1q,r and Extended Data Fig. 2).

Antibody-based proximity labeling of the myelin–axon interface

Oligodendrocytes and neurons interact through direct myelin–axon contact and extracellular vesicle-mediated signaling[31]. To investigate disruptions in AD, we developed a strategy to map the molecular architecture of the myelin–axon interface at subcellular resolution by adapting proximity biotinylation for protein isolation in human postmortem brains[32–34]. For selective protein enrichment, we used anti-CASPR and anti-(myelin-associated glycoprotein) MAG antibodies as baits (Fig. 2a). CASPR, a neuronal adhesion protein anchoring the paranodal region[1,35], was used to biotinylate paranodal proteins, while MAG, a myelin membrane protein at the periaxonal space[36–38] that is highly expressed at internodes and low at paranodes[38], was used to capture internodal proteins. We immunostained fixed human and mouse brain sections with these antibody baits, followed by horseradish peroxidase (HRP)-conjugated secondary antibody labeling and biotinylation with Biotin-XX-Tyramide and H_2O_2. Biotinylated proteins were enriched from brain lysates using streptavidin beads and validated by western blot. High specificity and spatial precision were confirmed by colocalization of streptavidin with CASPR or MAG signals in high-resolution confocal images (Fig. 2b(a–f),c(a–c)) and by stimulated emission depletion (STED) microscopy, which showed a 50-nm biotinylation radius (Extended Data Fig. 3). Control experiments without antibodies, H_2O_2 or Biotin-XX-Tyramide yielded negligible

Fig. 1 | AI-guided confocal imaging analysis revealed myelin paranode pathology in AD human postmortem brains. a, Workflow for paranode, myelin and axon analysis in human postmortem brains. **b**, Immunofluorescence labeling of myelin (PLP1, gray) in AD human brains and age-matched controls. Scale bar, 200 µm. **c**, Raw immunofluorescence staining of myelin (PLP1, gray) and AI-generated masks (yellow) and myelin objects (blue). **d**,**e**, Quantification of normalized myelin volume (**d**) and mean gray intensity (**e**) comparing AD human brains ($n = 6$) with controls ($n = 9$). Mann–Whitney test. **f**, Immunofluorescence of axons (SMI312, green) in AD brains and controls. Scale bar, 200 µm. **g**, Raw immunofluorescence of axons (SMI312, green) and AI-generated masks (yellow) and axon objects (blue). **h**,**i**, Quantification of normalized axon volume (**h**) and mean gray intensity (**i**) comparing AD brains ($n = 7$) versus controls ($n = 6$). Mann–Whitney test. **j**, Raw immunofluorescence of paranodes (CASPR, green) in AD brains and controls. Scale bar, 50 µm. Raw paranode staining (CASPR, green) and AI-generated mask (yellow) and paranode objects (blue). **k**,**l**, Quantification of paranodes in AD brains ($n = 10$) and controls ($n = 8$). Paranodes were binned into three categories according to their length: 0–5 µm, 5–10 µm and >10 µm. **k**, To compare paranode density between human AD versus control, unpaired *t*-test (two-tailed) was performed: '0–5 µm': $P = 0.002$; '5–10 µm': $P = 0.008$; '10+': $P = 0.711$ (NS). To compare the number of paranodes in human AD or control, respectively, one-way ANOVA was performed. In human controls, the number of paranodes of '0–5 µm' versus '5–10 µm' ($P = 0.043$), '0–5' versus '10+' ($P < 0.0001$) and '5–10 µm' versus '10+' ($P < 0.0001$). In human AD, '0–5' versus '5–10 µm' ($P = 0.896$), '0–5' versus '10+' ($P < 0.0001$) and '5–10 µm' versus '10+' ($P < 0.0001$). **l**, To compare the fluorescence intensity of paranode labeling between human AD versus control, unpaired *t*-test (two-tailed) was performed: '0–5 µm': $P = 0.103$; '5–10 µm': $P = 0.272$; '10+': $P = 0.743$. **m**, Paranode labeling (green, CASPR-labeled) in human AD and controls. Scale bar, 5 µm. **n**, Abnormal separation of paranode (gray, CASPR-labeled) compared with normal paranode in AD human brains. Scale bar, 5 µm. **o**, Quantile–quantile (Q-Q) plot shows comparison of paranode size (volume) between human AD versus control. Welch *t*-test (two-tailed) was performed. **p**–**r**, Quantification of myelin density in Cnp-EGFP-5XFAD mice ($n = 4$) and control ($n = 5$) (**p**). Normalized myelin volume (**q**) and mean gray intensity (**r**). Mann–Whitney test was performed. Error bars indicate s.e.m. and quantifications were performed two-sided in all experiments. Ctrl, control; NS, not significant.

https://doi.org/10.1038/s41593-025-01973-8

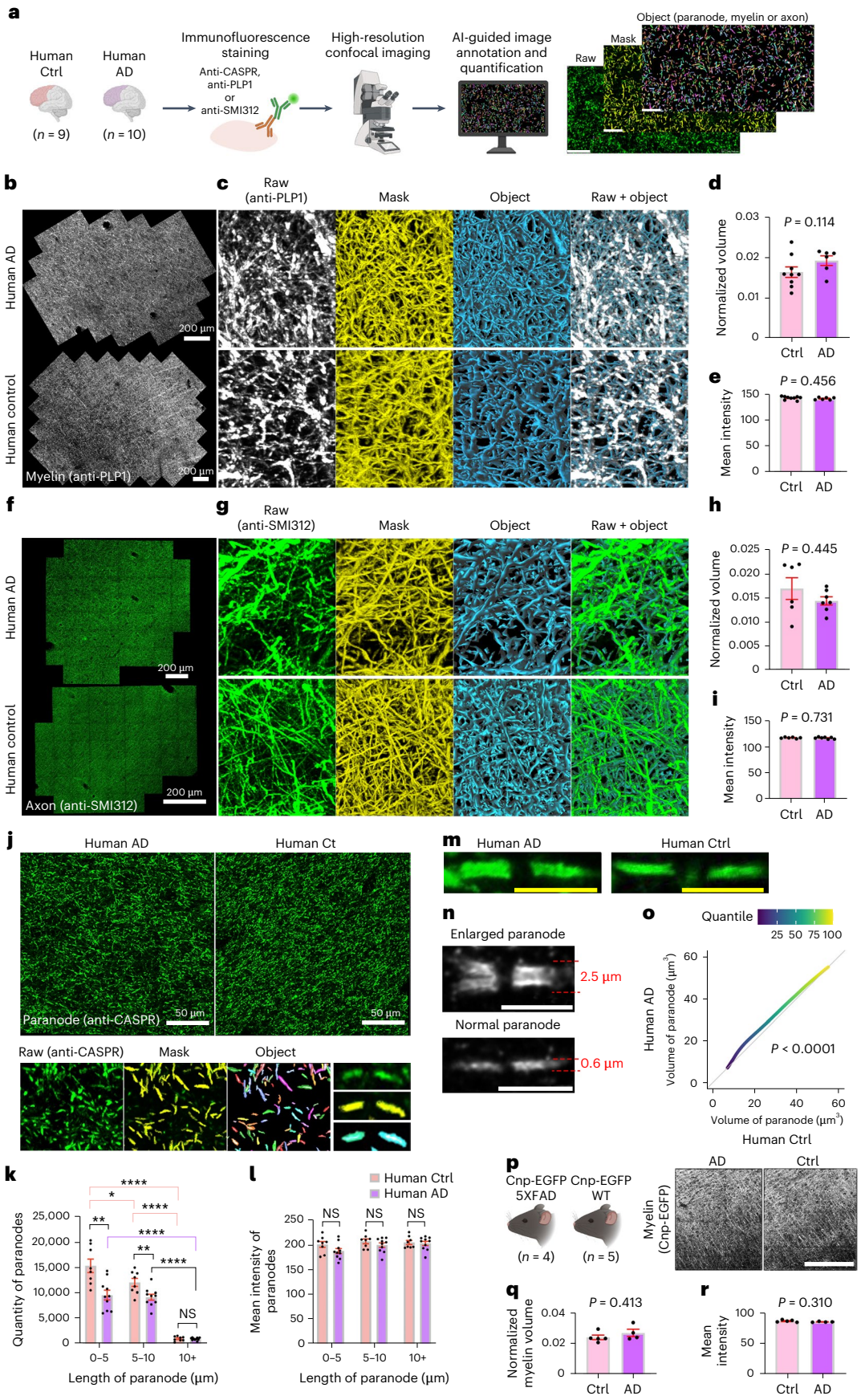

https://doi.org/10.1038/s41593-025-01973-8

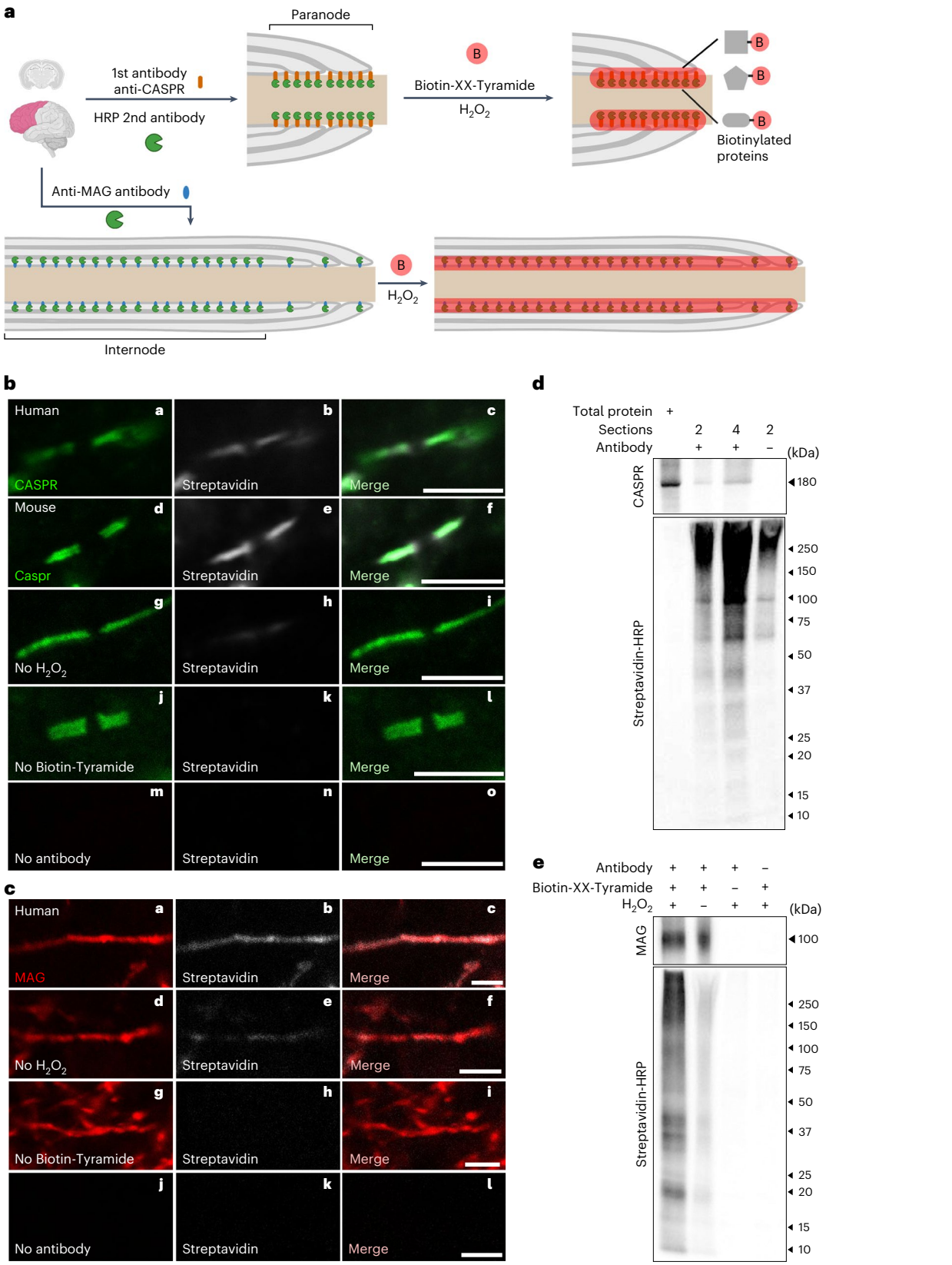

Fig. 2 | Proximity labeling of paranodes and the myelin–axon interface in AD human brains and mice. a, Schematic of the proximity labeling pipeline showing biotinylation of paranode-enriched (anti-CASPR) and myelin–axon interface (anti-MAG) proteins in human postmortem brains and mice. Postmortem human frontal cortex (highlighted in pink) was used. **b**,**c**, Representative confocal images of proximity labeling for paranodes (**b**) and myelin–axon interface (**c**). Biotinylated proteins are visualized by streptavidin (gray). Controls without H_2O_2 Biotin-XX-Tyramide or antibody showed no streptavidin signal. Scale bar, 5 µm. **d**,**e**, Western blots showing detection of the bait proteins: CASPR (**d**) and MAG (**e**), as well as the pulled down biotinylated proteins revealed by streptavidin-HRP. CASPR and MAG were not detected in the no-antibody controls (**d**,**e**), or in the no-biotinylation control (**e**).

https://doi.org/10.1038/s41593-025-01973-8

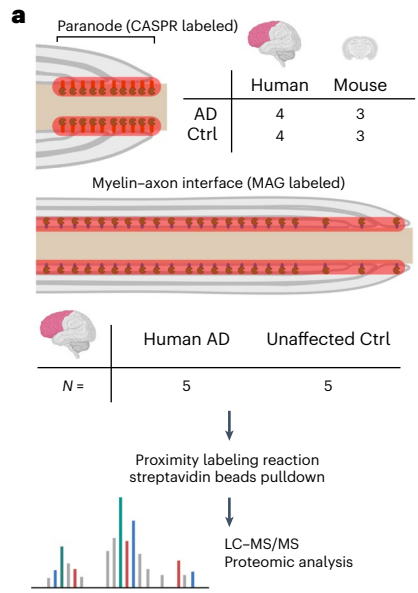

b

Anti-CASPR labeled	versus	No antibody labeled
	Human Ctrl	Human AD	5XFAD
Protein labeled	2,771	2,803	6,566
Quantification	Precursor intensity and spectra counts shared hits were included		
Cutoff	Cutoff analysis plus statistical cutoff: fold change > 3.5		
	FDR < 0.05	FDR < 0.05	FDR < 0.1
Paranode enriched	179	804	745

Anti-MAG labeled	versus	No antibody labeled
	Human Ctrl	Human AD
Protein labeled	2,393	2,407
Quantification	Precursor intensity and spectra counts only shared hits were included	
Cutoff	$P < 0.05$, FDR < 0.1, fold change > 1.5	
Myelin–axon interface enriched	176	229

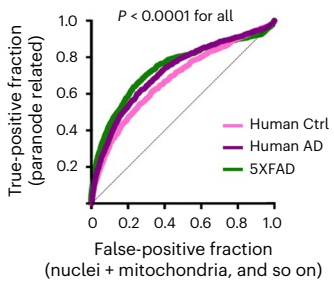

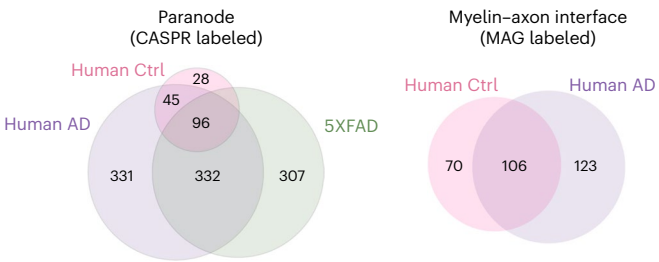

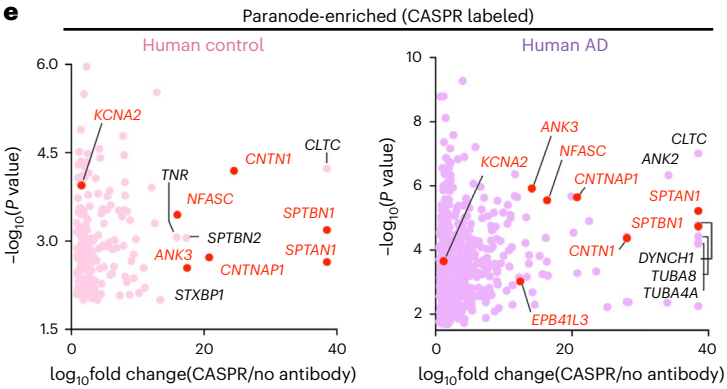

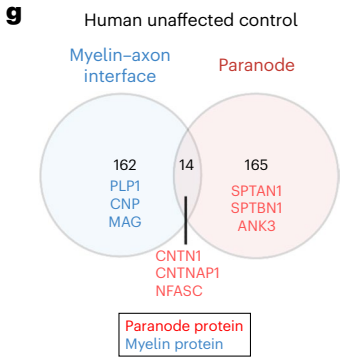

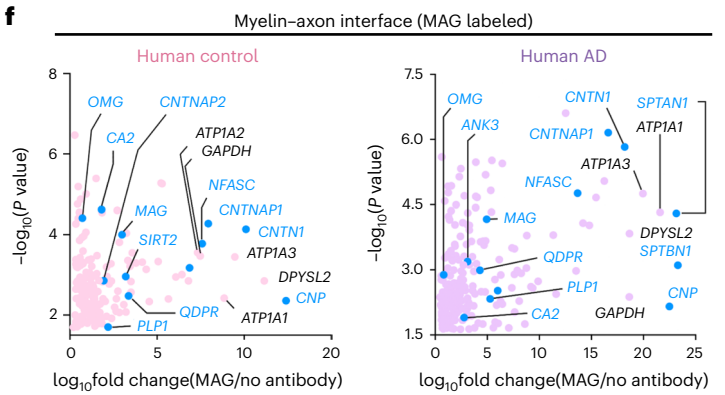

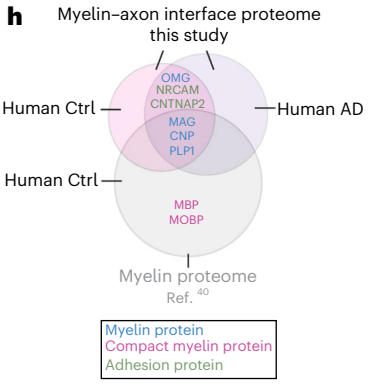

Fig. 3 | Subcellular paranode proteomics in AD human postmortem brains and mice. a, Schematic of the proximity labeling proteomics pipeline for paranodes in AD postmortem brains and 5XFAD mice. **b**, Protein detection and statistical cutoff in human AD, controls and 5XFAD mice. **c**, ROC curves for human AD, controls and 5XFAD mice. Proteins were ranked by fold change relative to no-antibody controls. True positives denote paranode-related proteins, while false positives include nuclear, mitochondrial and other non-paranode-related proteins. The ROC curve Wilson/Brown test showed $P < 0.0001$ for all groups. **d**, Venn diagram showing shared and unique proteomic hits among AD humans, controls and 5XFAD mice datasets. **e**,**f**, Volcano plots of paranode-enriched proteomics (**e**) and myelin–axon interface proteomics (**f**) in AD humans versus unaffected controls. The gene names of the top ten hits with greatest fold changes are labeled. In **e**, known paranode proteomic hits are highlighted in red, and in **f**, known myelin or myelin–axon interface proteins are highlighted in blue. Quantifications in panels **b**, **c**, **e** and **f** were performed two-sided. **g**, Venn diagrams comparing paranode-enriched proteomes (CASPR-labeled) with myelin–axon interface proteomes (MAG-labeled) in unaffected human controls. Selected known paranode proteins are shown in red, while known myelin paranode proteins are shown in blue. **h**, Venn diagrams comparing human control myelin–axon interface proteomes (MAG-labeled) with a previously published human myelin (white matter) proteome, highlighting selected unique and shared proteomics hits.

biotinylation (Fig. 2b,c). Immunofluorescence confirmed that MAG signal was myelin-restricted and CASPR signal was paranode-specific (Supplementary Fig. 2). Western blot and silver staining verified efficient and specific biotinylation of a broad protein range, including CASPR and MAG (Fig. 2d,e and Supplementary Figs. 3 and 4). We thus applied this approach to healthy and AD human brains and 5XFAD mice, enabling liquid chromatography–tandem mass spectrometry (LC–MS/MS) proteomic profiling of the myelin–axon interface with high molecular and subcellular specificity.

Uncovering the proteomes of the myelin–axon interface

To profile the myelin–axon interface proteomes, we obtained 34 human frontal cortex samples from Yale Alzheimer's Disease Research Center (Yale ADRC, 6 AD, 2 control), the Banner Institute (Banner, 11 AD, 10 control) and the National Institutes of Health (NIH) NeuroBioBank (NBB, 3 AD, 2 control). Clinical and neuropathological data were available for all samples (Supplementary Fig. 1). AD cases had high amyloid plaque burden, while controls exhibited minimal amyloid plaques. We performed MAG proximity labeling on five AD and five control brains to enrich internodal proteins, and CASPR proximity labeling on four AD and four controls brains to isolate paranodal proteins. Additionally, 14 AD and 13 control brains were used for immunofluorescence validation (Fig. 3a and Supplementary Fig. 1). Proximity labeling was performed with anti-CASPR or anti-MAG antibodies, followed by streptavidin bead protein enrichment and LC–MS/MS analysis (Fig. 3a). A no-antibody control excluded endogenous biotinylated proteins and nonspecific binders to the streptavidin beads (Fig. 3b).

In the unfiltered paranode-enriched dataset, we detected 2,804 proteins in AD and 2,772 in controls (Fig. 3b and Supplementary Table 1). Biological replicates were highly correlated (Extended Data Fig. 4), except for one excluded control (Pearson correlation $R^2 < 0.7$) (Extended Data Fig. 4). For stringent analysis, we applied both normalized total precursor intensity and normalized total spectral count for quantification, then filtered by statistical cutoff (false discovery rate (FDR) < 0.05, fold change > 3.5). The shared proteins of both methods were retained for downstream analysis (Fig. 3b). This approach identified differentially expressed proteins comparing CASPR-labeled paranodal samples and no-antibody controls (Fig. 3b), yielding 804 proteins in AD paranodes and 179 in unaffected controls (Fig. 3b and Supplementary Tables 1 and 2). To test for an optimal cutoff, we also applied cutoff analysis[39] (Supplementary Fig. 5 and Methods) and found highly similar results, and thus we proceeded with the statistical cutoff (FDR < 0.05, fold change > 3.5) for subsequent analyses. Receiver operating characteristic (ROC) analysis[39] showed that the top 20% of hits were primarily true positives (Fig. 3c and Methods), supporting the high specificity of the proteomics dataset (Supplementary Figs. 6a–d, 7c,d and 8c,d,g,h). Subcellular localization analysis showed detected proteins preferentially reside in the plasma membrane and cytoplasm rather than the extracellular space or nucleus (Supplementary Fig. 9b and Supplementary Table 3). These results highlight significant paranodal protein alterations in AD, underscoring molecular disruptions at the myelin–axon interface that may contribute to pathogenesis.

To assess whether similar patterns occur in AD-model mice, we performed proximity labeling in 5XFAD mice (Supplementary Tables 1 and 2). This analysis identified 747 proteins (Fig. 3a–d and Extended Data Fig. 5), 428 of which overlapped with human samples (Fig. 3d and Extended Data Fig. 5). Notably, eight of the top ten hits in human controls were paranode- or node of Ranvier-related proteins (Fig. 3e), underscoring the dataset specificity. We also identified several previously unrecognized paranodal proteins, expanding the known molecular composition of this critical myelin–axon domain (Fig. 3e, Extended Data Fig. 6a and Supplementary Fig. 10a).

Analysis of the MAG-labeled myelin–axon interface proteome provided additional insights. The unfiltered dataset detected 2,407 proteins in AD brains and 2,393 in controls. Applying a cutoff (FDR < 0.1, fold change > 1.5) yielded 229 proteins in AD and 176 in controls (Fig. 3b, Supplementary Figs. 6–9 and Supplementary Tables 1 and 2), with 106 shared between both groups (Fig. 3d). Many proteins were known components of internodes and paranodes (Fig. 3f), such as CNP, the top hit in controls. Additionally, several previously unrecognized myelin–axon interface proteins were identified (Fig. 3f, Extended Data Fig. 6b and Supplementary Fig. 10b).

We compared MAG- and CASPR-labeled proteomics data in controls to assess subcellular specificity. CASPR selectively detected paranode-enriched proteins, while MAG captured both internodal and paranodal proteins (Fig. 3g). Comparison of the MAG-labeled proteome with a recent bulk myelin proteomics study of normal human frontal cortex[40] showed that our myelin–axon interface proteome includes previously unidentified myelin and adhesion proteins. Notably, proteins such as MBP, confined to compact myelin, rather than the

Fig. 4 | Myelin–axon interface proteome reveals protein abnormalities in AD postmortem brains. a,**b**, Bar charts showing major themes from pathway enrichment analysis using the ActivePathways method, in paranode proteomes (**a**) and myelin–axon interface proteomes (**b**). Bar length represents the number of pathways identified in each theme, with colors indicating FDR values. The names of each bar are curated based on the main pathways of each subnetwork. Pie charts indicate the number of pathways in AD versus control datasets within each subnetwork. Themes related to paranode, myelin, axon and amyloid-β (**a**), as well as metabolism and myelin–axon (**b**), are highlighted in red, blue and magenta. **c**,**d**, Scatter plots of paranode-enriched proteomics (**c**) and myelin–axon interface proteomics (**d**) in AD human brains, ranked by the ratio of anti-bait protein samples versus no-antibody controls. The gene names of the top proteomic hits are labeled; novel top hits were further examined by immunofluorescence ExM (Fig. 6). **e**, Schematic outlining the statistical pipeline used to compare CASPR-labeled or MAG-labeled proteomes between AD human brains and unaffected controls (quantifications were performed two-sided). **f**,**g**, Scatter plots showing PAP (**f**) and MAP (**g**) hits that are up- or downregulated in AD compared with controls. Gene names of the top novel hits examined by ExM are shown (Fig. 6). **h**, Enrichment map of pathways and processes for differentially expressed PAP and MAP proteins. The network indicates pathways as nodes connected by edges and grouped into subnetwork themes if the pathways share many genes. **i**, IPA showing the top ten central nervous system-related signaling pathways enriched in PAP and MAP.

https://doi.org/10.1038/s41593-025-01973-8

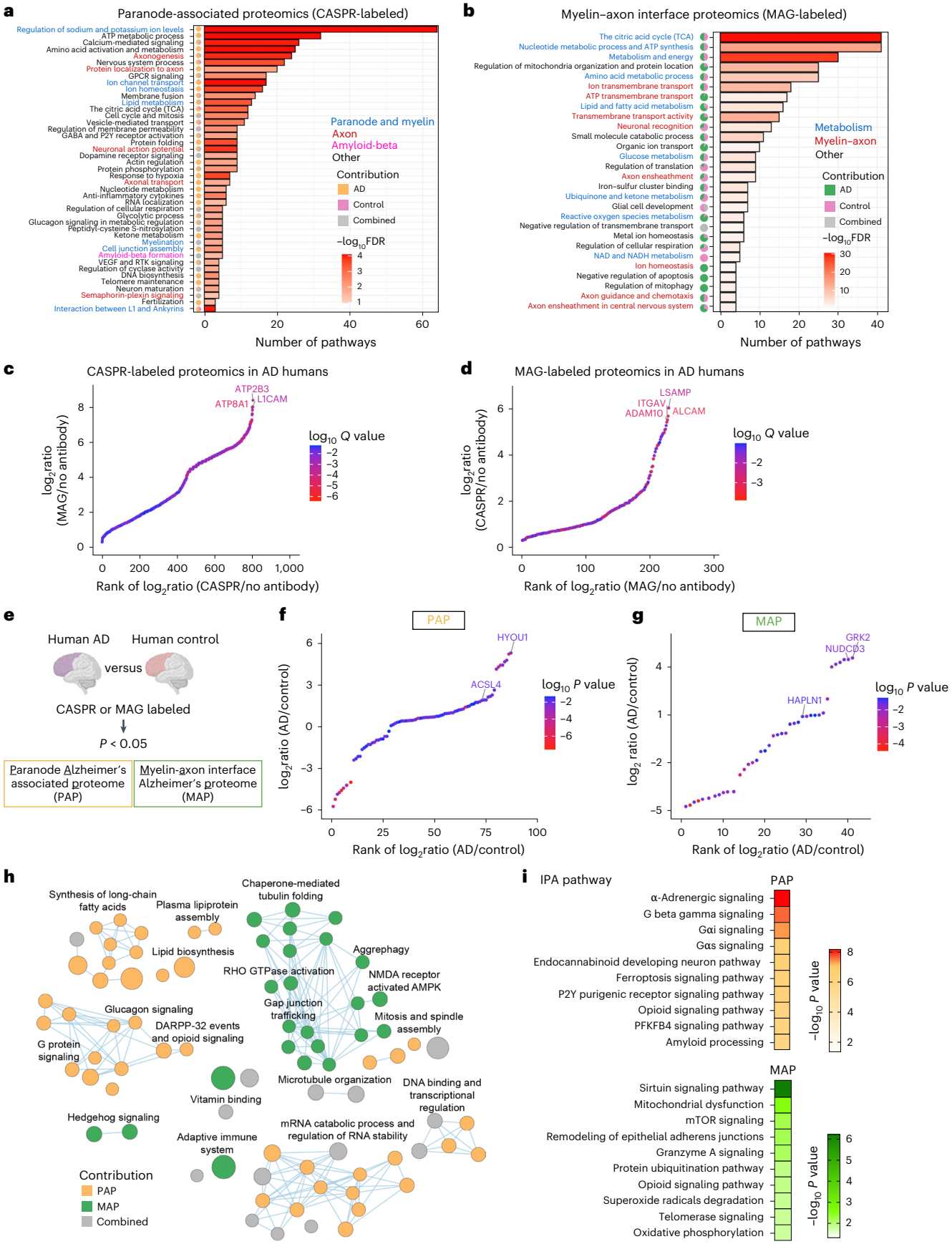

myelin–axon interface (Fig. 3h)[36,40], were not detected, confirming the selectivity of our approach.

Proteomic abnormalities at the myelin–axon interface in AD

To assess the biological functions underlying the identified proteomes, we performed an integrative pathway enrichment analysis using ActivePathways[41,42] to jointly prioritize proteins and pathways in the paranode and myelin–axon interface datasets (Fig. 4a,b, Extended Data Fig. 7 and Supplementary Table 4). In the paranode proteome, we identified biological processes related to paranodal function, such as neuronal action potential, cell junction assembly and interaction between L1 and Ankyrins (Fig. 4a and Extended Data Fig. 7a), as well as axonogenesis and amyloid-β formation pathways relevant to AD pathology (Fig. 4a and Extended Data Fig. 7a). For the myelin–axon interface, two major signaling pathway groups emerged: metabolism-related processes (for example, lipid and fatty acid metabolism) essential for myelin structure and function, and myelin–axon processes (for example, axon ensheathment, guidance and chemotaxis) (Fig. 4b and Extended Data Fig. 7b).

When ranking proteins by fold change to prioritize abundant true hits, many top hits were already known to be expressed at paranodes or within myelin (Fig. 3e,f). A ratio-based ranking of the CASPR- and MAG-labeled AD datasets highlighted proteins with minimal expression in controls (Fig. 4c,d), revealing novel proteins enriched in AD. In the CASPR-labeled AD dataset, novel hits included ATPase plasma membrane Ca^{2+} transporting 3 (ATP2B3), L1 cell adhesion molecule (L1CAM), which is important for axonal growth and myelination[43–45], and ATPase phospholipid transporting 8A1 (ATP8A1), alongside known proteins such as CNTNAP2, key for axo–glial contact at the juxtaparanode (Fig. 4c)[1]. In the MAG-labeled AD dataset, top hits included limbic system-associated membrane protein (LSAMP), activated leukocyte cell adhesion molecule (ALCAM), ADAM10 and (integrin subunit alpha V) ITGAV (Fig. 4d). ADAM10, a disintegrin and metalloproteinase expressed in both myelin and axons[46], is essential for myelination and axon targeting[47–49], and functions as an alpha secretase for amyloid precursor protein (APP)[48]. ITGAV, located at Schwann cell–axon contacts, is implicated in axo–glial interactions[47]. Both LSAMP[50] and ALCAM[51,52] regulate axonal outgrowth, with LSAMP also contributing to myelination[53]. Altogether, these findings align with the pathway enrichment analysis (Fig. 4a,b).

Next, we compared the CASPR-labeled (paranodal) and MAG-labeled (myelin–axon interface) proteomes between AD and control brains, using a cutoff $P < 0.05$ to define the paranode Alzheimer's-associated proteome (PAP) and the myelin–axon interface Alzheimer's proteome (MAP) (Fig. 4e–g and Supplementary Table 1). By ranking hits based on the AD-to-control ratio, we identified hypoxia up-regulated 1 (HYOU1) and Acyl-CoA synthetase long chain family member 4 (ACSL4) as top hits in PAP (Fig. 4f), and G protein-coupled receptor kinase 2 (GRK2), NudC domain containing 3 (NUDCD3) and hyaluronan and proteoglycan link protein 1 (HAPLN1) as top hits in MAP (Fig. 4g). Pathway enrichment analysis showed that PAP hits were associated with lipid synthesis, GPCR signaling and regulation of RNA stability, while MAP hits were enriched in gap junction trafficking, tubulin binding and Rho GTPase activation (Fig. 4h and Supplementary Table 4). Consistent with these results, ACSL4, a top PAP hit, catalyzes fatty acid activation and is essential for lipid synthesis[54] (Fig. 4e,f), whereas NUDCD3, a top MAP hit, regulates cytoskeletal stability[55] (Fig. 4g). Ingenuity Pathway Analysis (IPA) further highlighted activation of GPCR signaling and amyloid processing in PAP (Fig. 4i). Ferroptosis also emerged as a top pathway, where ACSL4 plays a crucial role in lipid peroxidation which accelerates this process[54]. In contrast, IPA analysis of the MAP proteome (Fig. 4f) revealed enrichment in pathways related to sirtuin signaling, mitochondrial dysfunction and protein ubiquitination (Fig. 4i), linking myelin–axon interface alterations in AD to metabolic and proteostatic dysregulation.

Cell–cell communication analysis uncovers potential myelin–axon signaling dysregulation

We investigated potential ligand–receptor interactions at the myelin–axon interface using a new computational pipeline that integrates our proteomics data with publicly available single-nucleus RNA sequencing (snRNA-seq) data to map subcellular proteomic hits to their respective cell types (Fig. 5a)[12,15]. First, we used snRNA-seq data along with cell–cell communication (CCC) methods, including CellPhoneDB[56], CellChat[57] and LIANA[58] (Fig. 5a), to assess ligand–receptor communication across different brain cells. Next, we performed enrichment analysis to confirm the cell-type-specificity of our proteomics results (Fig. 5a). Finally, we mapped out the ligand–receptor pairs that were identified by the myelin–axon interface proteomics and predicted their downstream signaling pathways (Fig. 5a).

Using this workflow, we reanalyzed a recent snRNA-seq dataset from the superior frontal gyrus in AD (Braak stage 6) and controls[12], similar to the specimens used for our subcellular proteomics. After single-cell clustering, cell-type annotation (Extended Data Fig. 8a,b) and CCC analysis, we evaluated the enrichment of candidate proteins from the MAG- and CASPR-labeled proteomes with ligand–receptor pairs from the snRNA-seq dataset (Extended Data Fig. 8c). Notably, the proteomic hits from both MAG- and CASPR-labeled datasets were highly enriched among the receptor–ligand interactions specific to neurons and oligodendrocytes compared with overall CCC analysis (Extended Data Fig. 8c), highlighting the cell-type specificity of the subcellular proteomics.

To identify ligand–receptor pairs and their potential downstream signaling pathways, we cross-referenced our proteomics data with ligand–receptor pairs from the CCC analysis in neurons and oligodendrocytes (Fig. 5b and Supplementary Table 5), revealing 45 pairs in AD and 26 in controls (Fig. 5b,c and Extended Data Fig. 8d,e). Among these, we identified several new cell-type-specific pairs at the myelin–axon interface, including NRXN3-NXPH1 and GRM3-CALM1 (Fig. 5c–e and Extended Data Fig. 8d,e), as well as established pairs such as CNTN2-NRCAM and the LGI3-ADAM23-Kv1.2 complex (Fig. 5c–e and Extended Data Fig. 8d,e). Some pairs were compartment-specific (for example, TF-TFRC detected at the paranode but not the internode), while others (for example, NRXN3-NXPH1, S100A1-RYR2 and GRM3-CALM1) were unique to AD (Fig. 5c–e, Extended Data Fig. 8d,e and Supplementary Table 5).

Next, we extracted the downstream biological processes modulated by these ligand–receptor interactions (Fig. 5f,g). To identify gene signatures associated with these processes, we integrated differential transcription factor activity analysis with CCC analysis and restricted

Fig. 5 | CCC analysis reveals potential AD-associated ligand–receptor interactions at the myelin–axon interface. a, Workflow of a new CCC analysis pipeline that integrates subcellular proteomics with snRNA-seq data to reveal ligand–receptor interactions at the myelin–axon interface in AD human brains and controls. **b**, Intersection of proteins from subcellular proteomics (paranode proteomics or myelin–axon interface proteomics) with neuron-oligodendrocyte CCC proteins. **c**, Subcellular proteomics-informed ligand–receptor pairs at the myelin–axon interface. Source and target cell types indicate the cells expressing the ligand or receptor. Pairs unique to AD are shown in purple, pairs in both AD and controls are in brown and pairs unique to controls are in pink. **d**, Examples of ligand–receptor pairs at the myelin–axon interface, with cell-type-specific RNA expression of each gene retrieved from the snRNA-seq dataset[12]. **e**, Schematic of selected ligand–receptor pairs at the myelin–axon interface: known pairs in blue, predicted pairs in yellow and predicted pairs detected only in AD in red (full list in Supplementary Table 4). **f**, Workflow for predicting downstream signaling influenced by the ligand–receptor interactions. **g**, Predicted downstream biological processes induced by ligand–receptor interactions at the myelin–axon interface in AD and controls.

https://doi.org/10.1038/s41593-025-01973-8

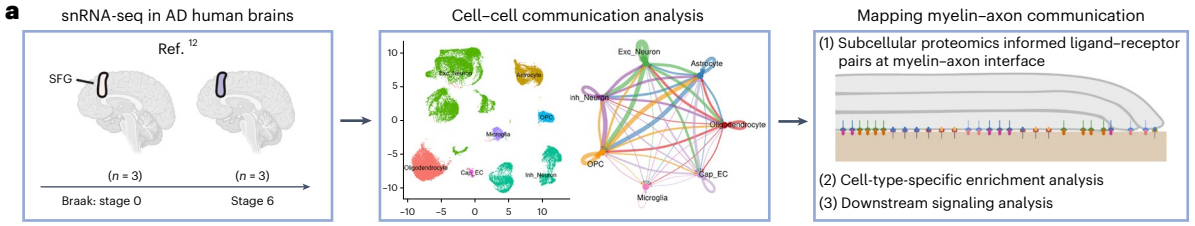

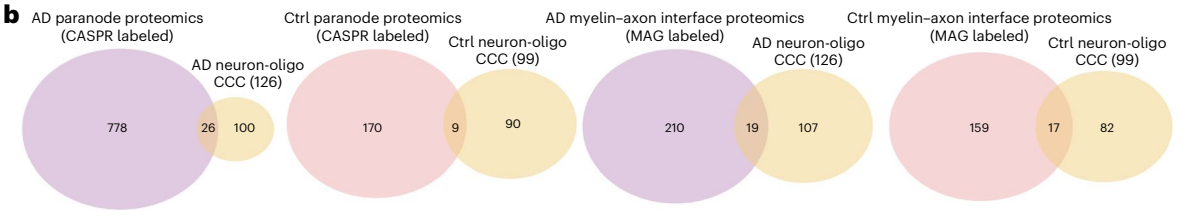

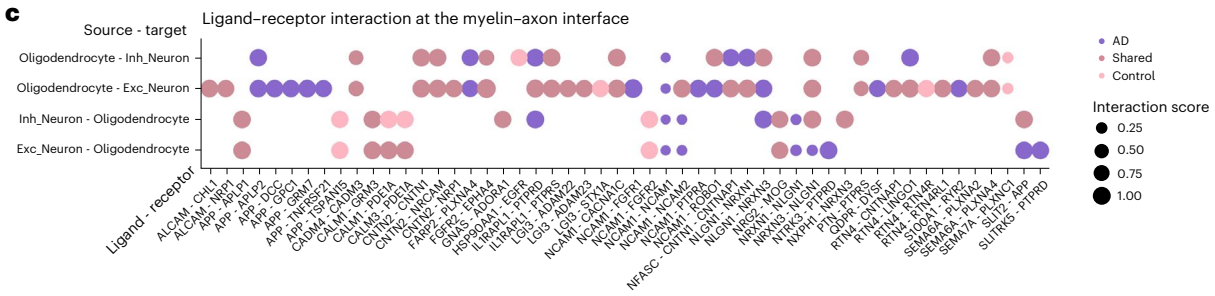

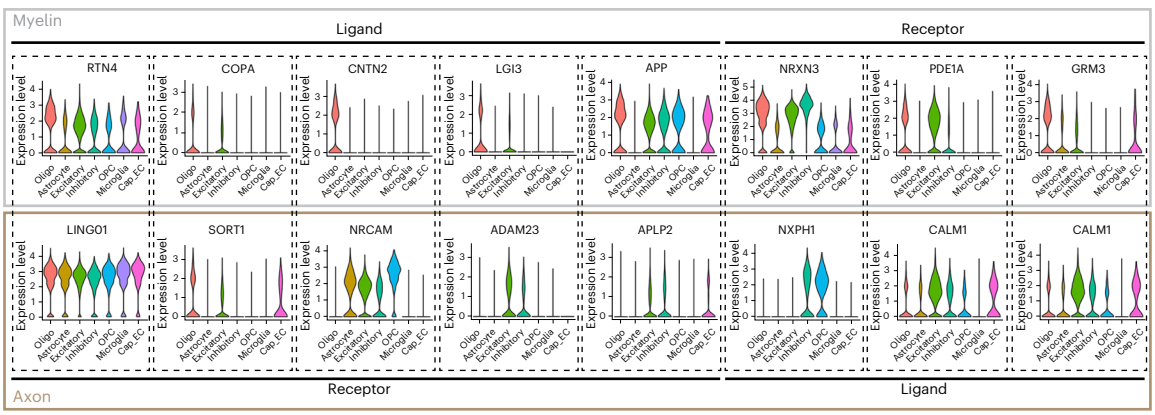

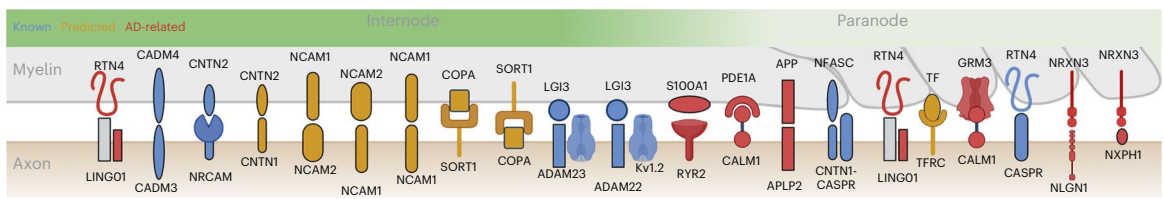

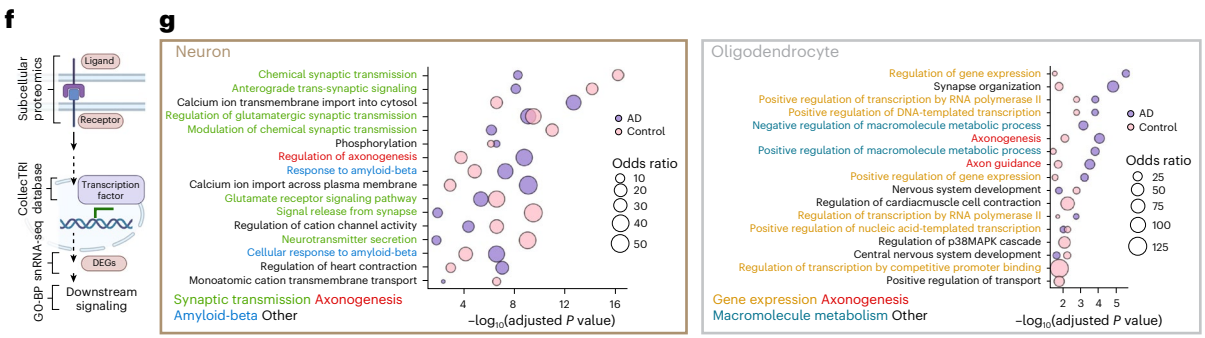

https://doi.org/10.1038/s41593-025-01973-8

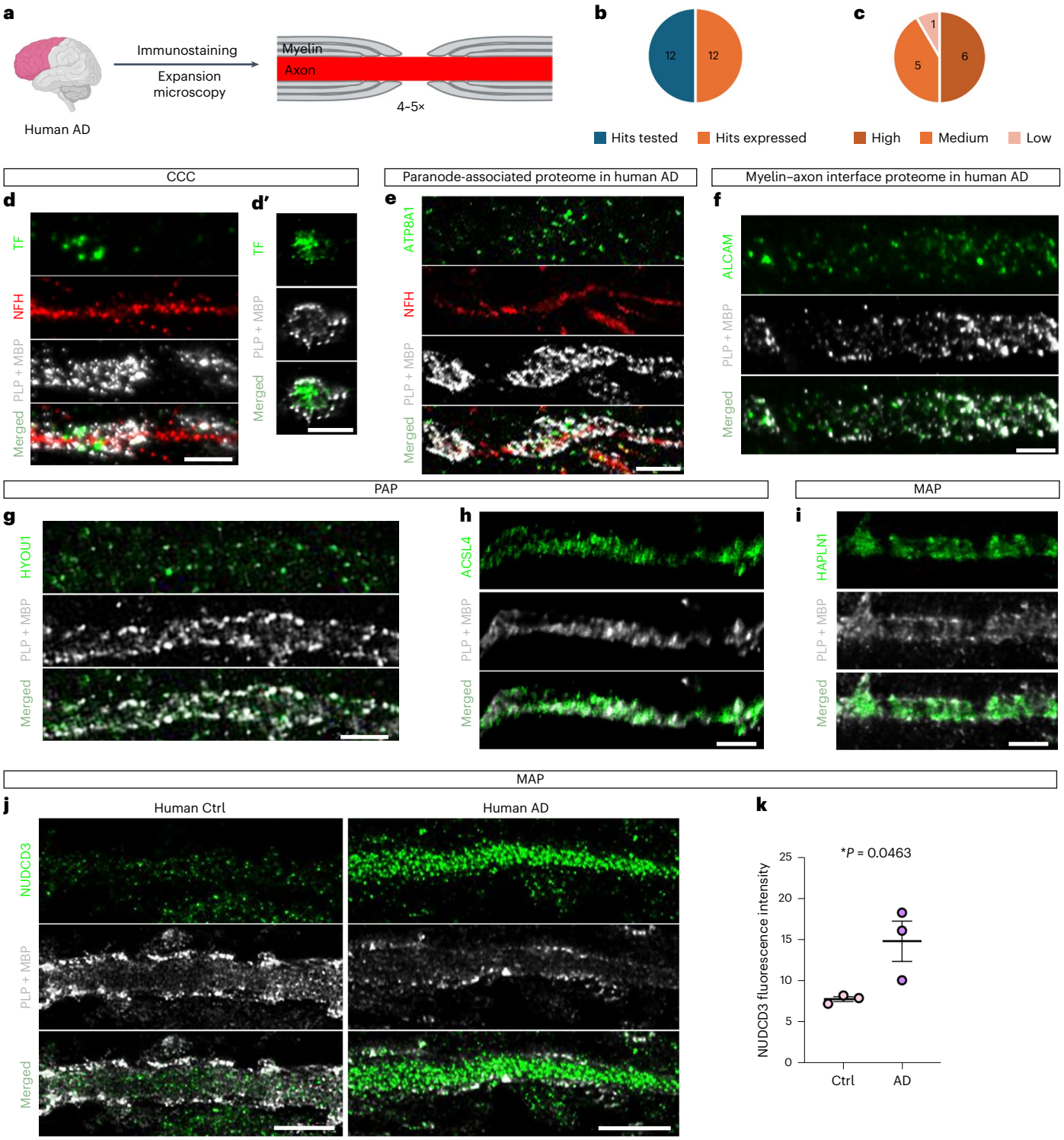

Fig. 6 | ExM demonstrates expression of proteomic hits at the myelin–axon interface. a, Schematic of the ExM pipeline applied to AD human frontal cortex. **b**,**c**, Pie charts showing that all 12 tested proteomics hits were detected at the myelin–axon interface (**b**), and among these, 6 had high expression, 5 medium and 1 low (**c**). **d**, ExM showing Transferrin (TF, green) with high expression at the paranode in AD brain (myelin (PLP and MBP, gray) and axon (NFH, red)). **d′**, Inset shows a coronal view of TF (green) within a myelin sheath (gray). **e**, ExM showing ATP8A1 (green) with medium expression at the paranode and along the internode. Myelin (PLP and MBP, gray) and axons (NFH, red). ATP8A1 was also detected on unmyelinated axons (red). **f**, ExM image showing ALCAM (green), a top hit from the MAG-labeled proteome in AD, with high expression within the myelin sheath (gray). **g**,**h**, ExM images of top PAP proteomic hits in AD: HYOU1 (green) with medium (**g**) and ACSL4 (green) with high (**h**) expression within myelin sheaths (PLP and MBP, gray). **i**,**j**, ExM images of top MAP proteomic hits in AD: HAPLN1 (green), with high expression in myelin (gray) (**i**), and NUDCD3 (green), with high expression in the axons (**j**). **j**, Representative ExM images showing NUDCD3 (green) in AD and controls within myelin and axons. **k**, Quantification shows significantly higher NUDCD3 expression in AD compared with controls ($n = 3$ brains per group; unpaired t-test, $P = 0.0463$). Error bars indicate s.e.m.; quantification was two-sided. Scale bars, 10 µm.

differentially expressed genes (DEGs) to functionally similar genes[59,60]. First, we identified the ligands and receptors that were found in both the snRNA-seq CCC analysis and our proteomics data, and the transcription factors that showed differential activity in oligodendrocytes and neurons from AD versus control conditions by snRNA-seq. These components formed the 'skeleton' of altered signaling processes in AD. We then incorporated downstream DEGs annotated with similar processes in the gene signatures (Fig. 5f and Methods). In neurons, this analysis revealed strong upregulation of axonogenesis, responses of amyloid-β and calcium ion transport, alongside reduced synaptic transmission in AD (Fig. 5g and Supplementary Table 6). Similarly, in oligodendrocytes, axonogenesis and axonal guidance were upregulated, along with increases in gene expression-related processes and macromolecule metabolism (Fig. 5g and Supplementary Table 6).

The combined analysis using proximity labeling proteomics and snRNA-seq demonstrates the power of integrating subcellular proteomics with multi-omics to uncover molecular and cellular mechanisms across scales. To examine proteins and gene expression patterns at different scales, we compared our MAPs and PAPs against previously reported bulk proteomic studies[16] and snRNA-seq data[11] from the same brain regions. Although some gene expression patterns were consistent across techniques, MAPs and PAPs contained many AD-dysregulated proteins not captured by bulk proteomics or snRNA-seq (Extended Data Fig. 9), underscoring the importance of subcellular proteomics in revealing potential myelin–axon signaling changes in disease.

ExM reveals expression patterns of proteomic hits

To validate the proteomics datasets, we examined 12 top hits in AD human postmortem brains using super-resolution ExM to assess their expression at the myelin–axon interface (Fig. 6a). We selected these hits based on their ranking and the availability of validated commercial antibodies. These included ATP2B3, L1CAM and ATP8A1 from the CASPR-labeled AD proteomes (Fig. 4c); LSAMP and ALCAM from the MAG-labeled AD proteomes (Fig. 4d); HYOU1 and ACSL4 from the PAP hits (Fig. 4f); GRK2, NUDCD3 and HAPLN1 from the MAP hits (Fig. 4g); and Transferrin and NRXN3 from the CCC-predicted candidates (Fig. 5e and Supplementary Table 5). In total, all 12 proteins were found to be expressed at the myelin–axon interface, with six showing high expression, five medium expression and one low expression (Fig. 6b,c and Supplementary Fig. 11).

CCC analysis predicted that Transferrin is a ligand expressed by myelin at the paranode, while its receptor TFRC is expressed by axons (Fig. 5e and Supplementary Tables 1 and 5). Proteomics showed Transferrin as a PAP hit downregulated in AD (Supplementary Table 1). Transferrin is known to be expressed in oligodendrocytes[61,62] and plays a crucial role in oligodendrocyte function and myelination[63–65], while TFRC is expressed in axons[66]. ExM revealed that Transferrin is highly expressed at the paranode, moderately expressed at the internode and primarily colocalizes with myelin (Fig. 6d,d′). Additionally, NRXN3, predicted by the CCC analysis to function as both a ligand and receptor on myelin and axons (Fig. 5c–e and Supplementary Table 5), was detected at medium levels along both myelin and axons (Supplementary Fig. 11f).

Next, we examined several top hits from the CASPR-labeled paranode-associated proteome. These included L1CAM, which mediates axonal growth and myelination[43–45]; ATP8A1, a catalytic component of a P4-ATPase flippase involved in phosphatidylserine transport[67,68]; and ATP2B3, essential for calcium homeostasis[69] (Fig. 4c). We observed medium expression of ATP8A1 at both paranodes and internodes (Fig. 6e and Supplementary Fig. 11a), and ATP8A1 was also present in unmyelinated axons, indicating expression in both axons and myelin (Fig. 6e). ATP2B3 showed medium expression at the paranode and internode (Supplementary Fig. 11a,b), while L1CAM was abundantly expressed at the myelin–axon interface (Supplementary Fig. 11a,c).

We also examined MAG-labeled hits, focusing on the top candidates, LSAMP and ALCAM (Figs. 4d and 6f, Supplementary Fig. 11d and Supplementary Table 1). LSAMP, an IgLON family adhesion molecule, is highly expressed in mouse neurons and oligodendrocytes[53]. LSAMP has been postulated as a negative regulator of myelination in the fimbria-fornix[53] and regulates neurite outgrowth and synapse formation[50]. ExM confirmed high LSAMP expression within myelin sheaths in AD brains (Supplementary Fig. 11a,d). ALCAM, a cell adhesion molecule linked to axonal growth[51,52] and blood-brain-barrier integrity[70], with its expression correlating with amyloid load in AD brains[71], was also highly expressed within myelin (Fig. 6f), consistent with our proteomic results.

We further examined the localization of top PAP and MAP hits (Figs. 4e–g and 6g–k and Supplementary Fig. 11e). HYOU1 and ACSL4, two top PAP hits, were upregulated in AD (Fig. 4f). HYOU1 prevents endoplasmic reticulum stress[72] and can reduce Abeta 42 formation when inhibited[73]. ACSL4, a key enzyme in fatty acid activation and ferroptosis[54], was elevated in AD, while free fatty acids were reduced in AD hippocampus, suggesting that upregulated ACSL4 may drive lipid peroxidation and ferroptosis[74,75]. ExM showed medium HYOU1 expression (Fig. 6g) and high ACSL4 expression in myelin (Fig. 6h). Among MAP hits, GRK2, NUDCD3 and HAPLN1 were upregulated in AD (Figs. 4g and 6i–k, Supplementary Fig. 11e and Supplementary Table 1). HAPLN1, an extracellular matrix protein, is upregulated in AD[76] with increased glycosylation[77]. NUDCD3 binds to the dynein complex and its depletion induces degradation of dynein intermediate chain[55]. ExM showed HAPLN1 was highly expressed along myelin segments (Fig. 6i and Supplementary Fig. 11a), while NUDCD3 was highly expressed in axons and also detected in myelin (Fig. 6j and Supplementary Fig. 11a). In contrast, GRK2 exhibited low expression in myelin (Supplementary Fig. 11a,e). Although ExM provided high-resolution imaging, variability in staining and heterogenous expansion between samples prevented precise quantification. Nonetheless, among MAP proteins, NUDCD3 was the most upregulated at the myelin–axon interface in AD compared with controls (Fig. 6j,k and Supplementary Fig. 11a).

Paranodal and periaxonal myelin regions are sites of amyloid-β accumulation

Given our findings that amyloid-β processing is dysregulated in the myelin–axon interface proteome (Figs. 4a,i and 5g and Extended Data Fig. 7a), we investigated possible amyloid deposition within myelinated axons. We used super-resolution ExM in Thy1-YFP neuronal reporter mice crossbred with 5XFAD mice, combined with immunolabeling of myelin–axon markers and amyloid-β (Fig. 7a). 4G8 antibody labeling revealed distinct amyloid patterns: amyloid-β aggregates formed spiral patterns along some YFP-positive axons (Fig. 7b,b′ and Supplementary Fig. 12a)[78] that terminated in dense helical loops (Fig. 7c,c′ and Supplementary Fig. 12b,c,f,g)[79]. We often observed pairs of adjacent loops separated by a gap, consistent with paranodal myelin regions across a node of Ranvier (Fig. 7c–c′). This paranodal localization was confirmed by CASPR (Fig. 7d,d′ and Supplementary Fig. 12b,c) and CNPase immunolabeling (Fig. 7e and Supplementary Fig. 12d). Quantification showed that ~20% of axons in the corpus callosum and supracallosal regions in 5XFAD mice had axonal amyloid spirals and paranodal coils (Fig. 7f). Co-staining with the juxtaparanode marker anti-Kv7.3 revealed that most dense amyloid coils originated at paranodes and extended into juxtaparanodes (Fig. 7g and Supplementary Video 2). The dense helical patterns likely represent amyloid-β accumulation within paranodal channels, while the less dense spirals may be extensions into periaxonal spaces at internodes. Interestingly, bulbous axonal enlargements were sometimes observed at these helical amyloid-β aggregation sites, with disrupted axonal cytoskeletal continuity indicated by neurofilament SMI34 labeling (Fig. 7h,h′ and Supplementary Video 2). In some cases, amyloid-β fibers were also detected outside myelinated structures, near nodes of Ranvier (Supplementary Fig. 12e). These findings in mice indicate that aggregation-prone proteins tend to accumulate within myelin and paranodal channels, possibly due to axonal secretion or

https://doi.org/10.1038/s41593-025-01973-8

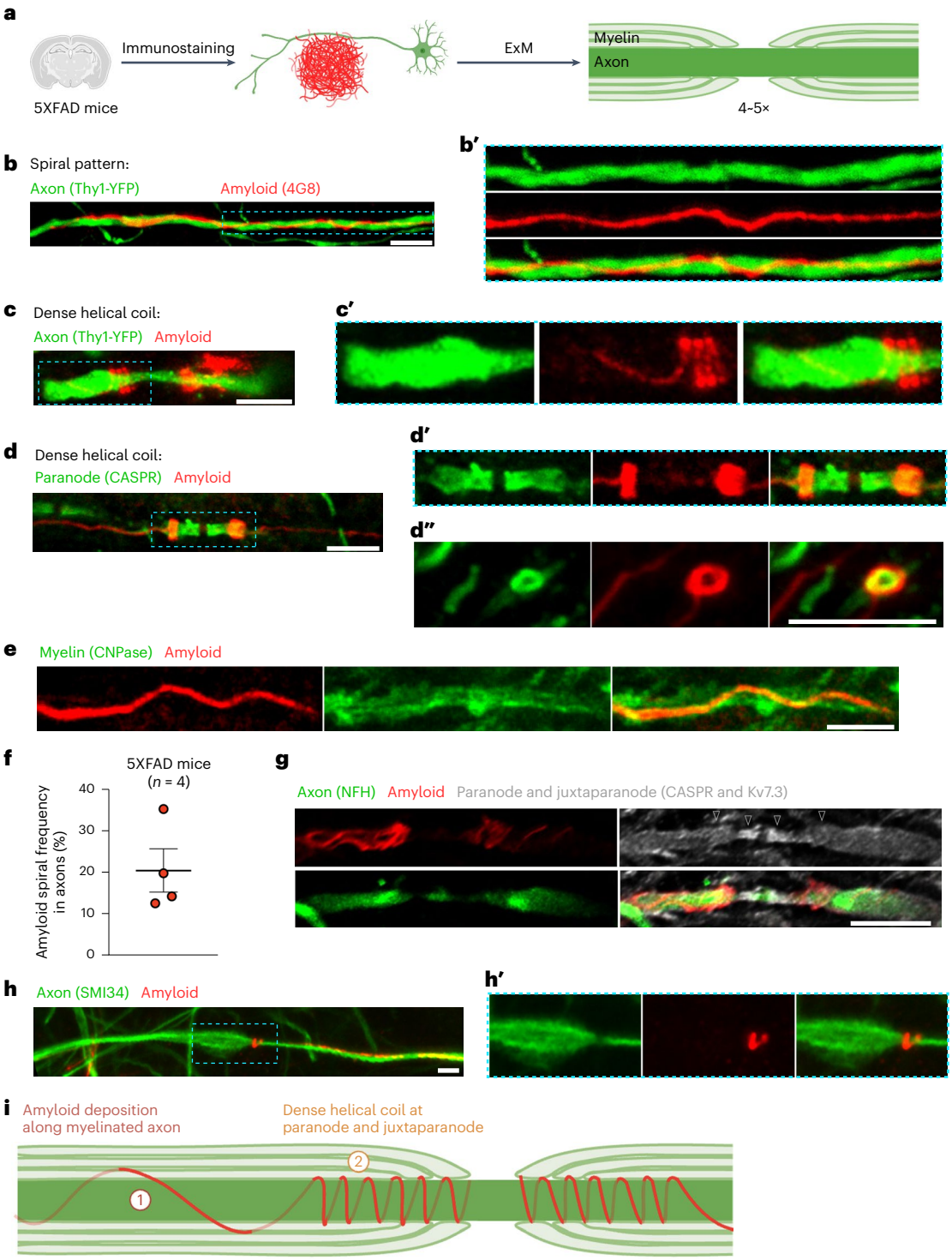

Fig. 7 | ExM reveals amyloid deposition at the paranode. **a**, Schematic of the ExM pipeline in AD-model mice. **b**, ExM image showing amyloid fibers (4G8, red) forming spirals along axons (Thy1-YFP, green) in Thy1-YFP-5XFAD mice. **b′**, Inset showing enlarged view of individual channels. **c**, ExM image showing amyloid fibers (4G8, red) that terminate in paired helical coils along axons (Thy1-YFP, green). **c′**, Inset showing enlarged view of each channel. **d**, ExM image showing a helical amyloid coil (4G8, red) at a myelin paranode (CASPR, green). **d′**, Inset showing enlarged view of each channel. **d″**, Inset showing sagittal view of the amyloid fiber wrapped around the CASPR-positive axon (green). **e**, ExM image showing an amyloid spiral (4G8, red) along a myelinated axon (CNPase, green). **f**, Quantification of the percentage of axons with amyloid spirals and coils in 5XFAD mice ($n = 4$; unpaired t-test; error bars indicate s.e.m. **g**, Confocal image showing an amyloid spiral and coil (4G8, red) along an axon (NFH, green) associated with paranodes (yellow arrowheads) and juxtaparanodes (blue arrowheads) (CASPR and Kv7.3, gray). **h**, ExM and zoom in (**h′**) images showing that amyloid paranodal coils (4G8, red) are sometimes associated with enlarged axons (SMI34, green). Scale bars, 5 µm (**b**–**e** and **h**) and 10 µm (**g**). **i**, Schematic summarizing the association of amyloid fibers at the internode (no. 1) and the paranode and juxtaparanode (no. 2) of myelinated axons, as revealed by ExM.

diffusion from the interstitial space (Fig. 7i). In human brains, helical paranodal aggregates were not observed; instead, fiber-like amyloid aggregates were detected at myelin internodes, albeit much less frequently than in mice (Supplementary Fig. 12h). Together with the proteomic abnormalities, these findings indicate that paranodal and internodal regions are particularly susceptible to disruption in AD, with potential consequences for axonal integrity and function.

Aberrant myelination of amyloid-plaque-associated axonal spheroids

Amyloid plaques in both humans and mice are surrounded by hundreds of axons with spheroid-like enlargements (dystrophic neurites) that disrupt action potential conduction and correlate with AD severity (Fig. 8a)[25]. Interestingly, we frequently observed myelination of these spheroids in both postmortem AD brains and 5XFAD mice (Fig. 8a–c). Myelinated spheroids were significantly larger than unmyelinated ones (Fig. 8c,d), suggesting that previously myelinated axons are more prone to form large spheroids or, alternatively, that larger spheroids promote de novo myelination. Most myelinated spheroids were partly covered by the paranodal marker CASPR (Fig. 8e–i), with abnormal paranodal architecture evident by both CASPR staining and transmission electron microscopy (TEM) (Fig. 8e,f,m′). Additionally, myelin, paranodal and juxtaparanodal markers, including CNP, CASPR and Kv 1.2, were frequently present within spheroids (Fig. 8j–l). TEM further revealed aberrant myelination frequently wrapping multiple spheroids together (Fig. 8m and Supplementary Fig. 13), likely explaining the atypical distribution of these markers within spheroids observed at lower-resolution imaging (Fig. 8j–l).

To determine whether spheroid-associated myelin reflects de novo myelination or originates from previously myelinated axons, we attempted to capture spheroid myelination by intravital imaging but were proved unsuccessful due to the temporal and spatial unpredictability of spheroid myelination events. Instead, we leveraged the fact that BCAS1 is expressed in newly formed but not mature myelin[53]. A combination of CNP and BCAS1 immunolabeling can thus distinguish de novo from mature myelination[80]. Using this approach in 12- to 15-month-old 5XFAD mice, we found that many spheroids were highly BCAS1-positive (Fig. 8n,o and Supplementary Fig. 14a). Approximately 4% of the spheroid halo around plaques was BCAS1-positive (Fig. 8p), and around 6% was CNP-positive (Fig. 8g,h,p), strongly suggesting active de novo myelination of spheroids in AD-like mice. However, despite substantial BCAS1-positive spheroids, only about 10% were ultimately CNP/PLP-positive in both mouse and human AD brains (Fig. 8g,h). Analysis of spheroid size relative to BCAS1 (de novo myelin) or CNP (mature myelin) labeling revealed that BCAS1-positive spheroids tended to be smaller, while CNP-positive/BCAS1-negative spheroids were significantly larger (Fig. 8q), suggesting continued spheroid enlargement post-myelination. Additionally, we and others found evidence of spheroids forming from previously myelinated axons[81], as indicated by small nascent spheroids, marked by endolysosome accumulation, within mature myelinated axons (Supplementary Fig. 12b,c), and similar to observations in mutant mice with myelin defects[81]. Together, these results indicate that while de novo myelination occurs on some spheroids, other instances arise from preexisting myelinated axons.

Discussion

Oligodendrocyte and myelin disruptions are important factors in AD, although the mechanisms remain unclear. We employed a multi-faceted approach to characterize the molecular and structural architecture of the myelin–axon interface in AD human brains and AD-like mice. To overcome the limitations of gradient fractionation-based proteomics, which often introduces contaminants from other subcellular compartments[82], we employed subcellular proximity labeling with antibody recognition[33,34]. This method allowed enrichment and mapping of proteins from distinct axonal subdomains, including paranodes, juxtaparanodes and internodes (Figs. 2 and 3, Extended Data Fig. 5 and Supplementary Table 1), which conventional purification techniques cannot achieve[28]. Integrating our proteomics with snRNA-seq data from AD brains identified ligand–receptor interactions and signaling pathways associated with early axonal pathology and myelin disruption, revealing molecular changes not detected in previous bulk proteomics and snRNA-seq studies (Extended Data Fig. 9).

Our findings show that the myelin–axon interface is highly vulnerable in AD, exhibiting reduced paranode numbers and enlargement of paranodal structures near amyloid deposits without overt myelin loss (Fig. 1 and Extended Data Fig. 2)[4,26,83]. This is further highlighted by our reanalysis of recent transcriptomics and proteomics studies[10,11,14,16] showing that myelin markers such as PLP1, CNP and MBP remain largely unchanged in AD (Extended Data Fig. 1). The patchy myelin density and altered white matter magnetic resonance imaging signals reported in AD[27–30,84,85] likely reflect microischemia and cerebral amyloid angiopathy[27–30] rather than primary demyelination.

Paranodal and juxtaparanodal vulnerability likely arise from two factors. First, the paranode's exposure to the interstitial space may increase its susceptibility to amyloid-β and protein aggregation (Fig. 1, Supplementary Fig. 12 and Supplementary Video 2). Second, axonal spheroid formation at paranodes appears to disrupt their architecture, impeding normal axonal trafficking and further promoting spheroid enlargement (Fig. 8). Notably, the presence of newly generated

Fig. 8 | Myelin paranode abnormalities associated with axonal pathology in AD humans and mice. a, Axonal spheroids (green) form around amyloid plaques (red) and are associated with markedly delayed or blocked axonal electrical conduction[25]. **b**, Myelin (green) wraps around an axonal spheroid in AD brain. Scale bar, 1 µm. **c**, In 5XFAD mice, myelin (Plp, gray) wraps around axonal spheroids (LAMP1, red); neurofilament (SMI312, green) and amyloid plaque (ThioS, blue) are also shown. Scale bar, 5 µm. **d**, Myelinated axonal spheroids are significantly larger than unmyelinated ones (paired *t*-test (parametric, two-tailed), $P < 0.008$, $n = 3$). **e**,**f**, Myelin (green) wraps around axonal spheroids (LAMP1, red) in Cnp-EGFP-5XFAD mice (**e**) and AD human brain (**f**) (PLP1). Paranode (CASPR, gray) is associated with spheroids in both humans and mice. Amyloid plaque (ThioS, blue). Scale bar, 5 µm. **g**, Approximately 80% of myelinated axonal spheroids (PAAS) are CASPR-positive ($n = 3$). **h**, Comparison of CASPR-positive versus -negative spheroid area in 5XFAD mice (CASPR-positive = 9.477, CASPR-negative = 90.523, s.d. = 1.801, $n = 3$) and AD humans (CASPR-positive = 11.20, CASPR-negative = 88.80, s.d. = 7.405, $n = 3$). **i**, Less than 3% of total paranodes are associated with spheroids in AD humans ($n = 3$). **j**–**l**, Images showing intrusion of CASPR-positive paranodes into axonal spheroids (red) in AD human brains (**j**) and mice (**k**,**l**). **l′**, Intruded myelin (green) is associated with paranodal marker CASPR (red) and juxtaparanodal marker Kv 1.2 (gray). **j**–**l**, Scale bar, 5 µm. **m**, Myelin (green) wraps around several spheroids (red) to form a large, myelinated spheroid cluster (related to Supplementary Fig. 13a). Scale bar, 5 µm. **m′**, Inset (blue box) shows a pair of paranodes (green) on a myelinated axonal spheroid (**m**): one half of the paranode (red arrow) is severely disrupted while the other half (blue arrow) remains intact; axonal cytoskeleton (yellow) extends into the spheroid. **m″**, Schematic of aberrant myelination of axonal spheroids. **n**, Newly formed oligodendrocytes (BCAS1-positive, gray; a large blue arrowhead indicates the cell body) myelinate spheroids (LAMP1, red, small blue arrowheads) in CNP-mEGFP-5XFAD mice; mature myelin is labeled by CNP-mEGFP (green). **o**, One large spheroid (LAMP1, red) is myelinated by mature myelin (CNP-positive, green, blue asterisk), while BCAS1-positive newly formed myelin wraps around an adjacent spheroid (LAMP1, red, yellow asterisk) and partially covers the CNP-positive spheroid (blue asterisk) as well as a small spheroid (LAMP1, red, blue arrowhead). Scale bars, 10 µm (**n**); 5 µm (**o**). **p**, Comparison of the proportion of BCAS1-positive versus CNP-positive spheroid area in 5XFAD mice ($n = 4$; unpaired *t*-test). **q**, Comparison of spheroid size as a function of BCAS1-positive versus CNP-positive myelin coverage in 5XFAD mice ($n = 4$; unpaired *t*-test). Error bars indicate s.e.m.; all quantifications were two-sided.

https://doi.org/10.1038/s41593-025-01973-8

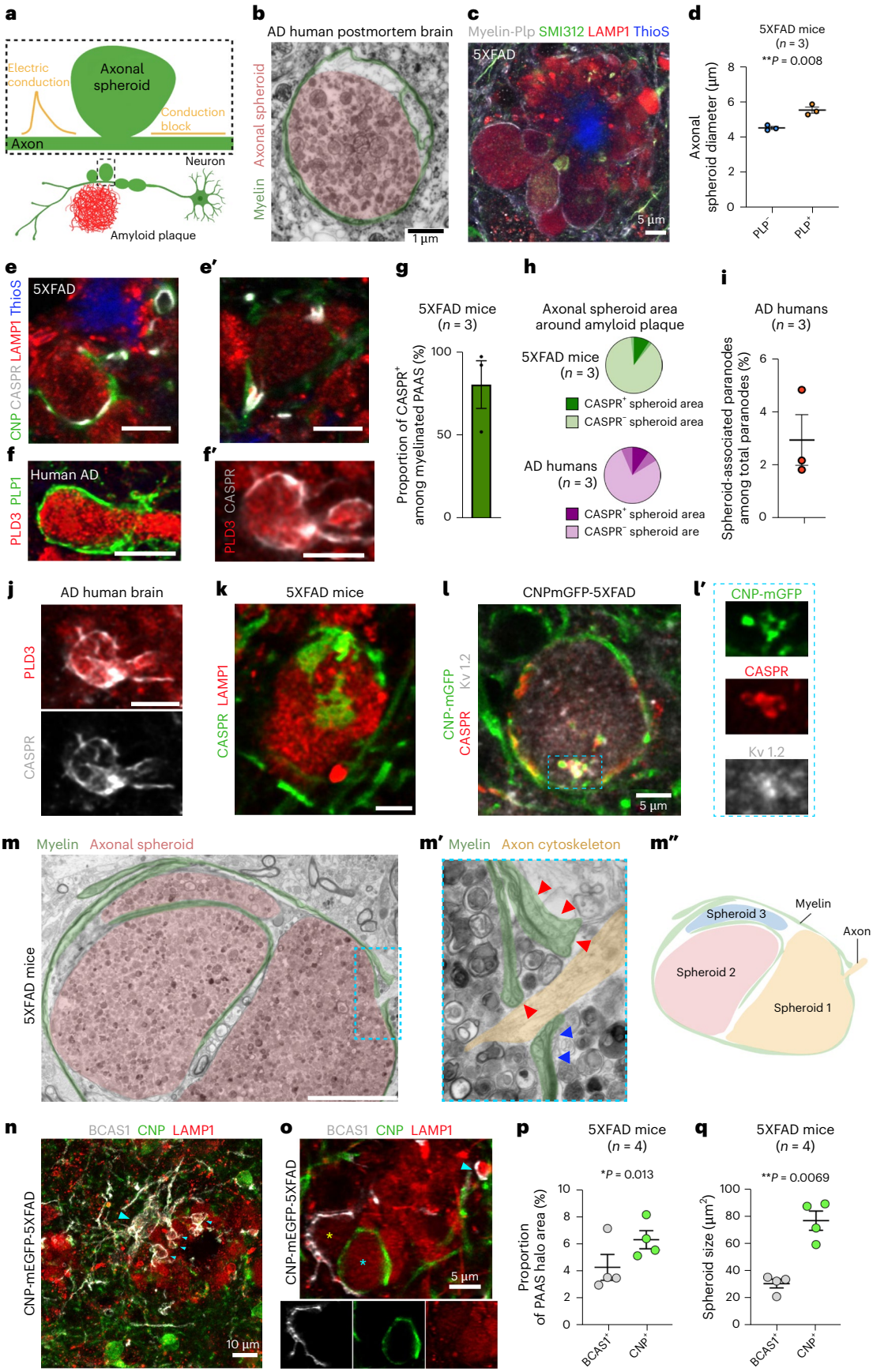

oligodendrocytes in AD-like mice[84,86] and potential elongation of remaining myelin internodes[87] suggest compensatory mechanisms[88] that could explain why overall myelin content remains unchanged in 5XFAD mice despite reduced paranode numbers.

Our analysis revealed disrupted AD-related signaling at the myelin–axon interface, including in lipid metabolism, axonogenesis and amyloid-β formation (Fig. 4 and Extended Data Fig. 7). Furthermore, proteomic data showed enrichment in lipid and fatty acid metabolism processes (Fig. 4b), underscoring key trophic interactions between myelin and axons (Fig. 4h,i). By integrating our subcellular proteomics with snRNA-seq to explore CCC (Fig. 5 and Extended Data Fig. 8), we uncovered previously unrecognized ligand–receptor pairs specific to the myelin–axon interface (Fig. 5c and Supplementary Table 5) that are enriched in both neurons and oligodendrocytes (Fig. 5d and Extended Data Fig. 8c–e). Our results indicate that these ligand–receptor interactions between myelin and axons may enhance axonogenesis, response to amyloid-β and calcium ion transport while reducing synaptic transmission in AD (Fig. 5f,g). In oligodendrocytes, we also observed upregulation of axonogenesis and axonal guidance pathways, along with enhanced gene expression and transcription-related processes (Fig. 5f,g). Collectively, these findings reveal potential molecular mechanisms underlying myelin–axon disruption and suggest that abnormal myelin–axon communication contributes to amyloid and axonal pathology in AD.

ExM revealed coil-like amyloid deposits in the paranodal/juxtaparanodal loops and myelin inner tongue loops in AD-model mice (Fig. 7 and Supplementary Fig. 12). These deposits likely represent amyloid peptides produced by neurons[89] or oligodendrocytes[90–93] that become trapped in periaxonal spaces or intracellularly at the inner tongue. Given that neurons are the predominant source of amyloid-β[92,93], our ligand–receptor interaction analysis supports upregulated responses to amyloid-β in neurons rather than in oligodendrocytes (Fig. 5g). Coil-like amyloid deposits were much less frequent in humans (Supplementary Fig. 12h) and in APP/PS1 mice[94] compared with 5XFAD mice, likely due to greater neuronal amyloid-β production driven by the Thy1 promoter in 5XFAD mice. Interestingly, these coils were sometimes associated with interrupted neurofilament staining and distal axonal enlargement, resembling spheroids (Fig. 7h and Supplementary Video 2). This suggests that protein accumulation and disruption of the myelin–axon interface may compromise periaxonal compliance and axonal trafficking, ultimately leading to spheroid formation.

We showed that some plaque-associated axonal spheroids were heavily myelinated and associated with disrupted paranode and juxtaparanode structures (Fig. 8 and Supplementary Fig. 13). While it is uncertain whether myelination precedes or follows spheroid formation, the presence of multiple spheroids encapsulated together by thin myelin sheaths (Fig. 8m and Supplementary Fig. 13) suggests that myelination occurs afterward, similar to myelin mistargeting of large neural structures such as cell bodies[95]. Indeed, many spheroids in AD-like mice were labeled with BCAS1, the transient marker for newly formed oligodendrocytes and myelin[96] (Fig. 8n,o and Supplementary Fig. 14). However, while about 4% of spheroids were BCAS1-positive at any one time, only around 10% matured to express CNP/PLP (Fig. 8g,h). This suggests that many newly formed oligodendrocytes fail to maintain their myelin sheaths, do not fully mature or die prematurely[86,97,98]. In addition, some spheroids appear to originate from preexisting myelinated axons (Supplementary Fig. 14b,c), with disrupted paranodal structures adjacent to them (Figs. 1n and 8e–m) suggesting that degeneration of myelin and paranodes may also promote spheroid formation[81,99]. However, these spheroids were generally small with thicker myelin sheaths (Supplementary Fig. 12b,c), compared with larger spheroids exhibiting thinner myelin sheaths (Fig. 8m,m′ and Supplementary Fig. 13), possibly reflecting myelin breakdown during spheroid growth. We previously demonstrated that axonal spheroid enlargement is associated with markedly delayed propagation of action potentials and impaired neuronal networks[25], with the severity of axonal spheroid pathology correlating with pre-mortem cognitive impairment in humans[25]. Our observation of disrupted paranode and node of Ranvier architecture suggests that, beyond spheroid formation, structural abnormalities at the myelin–axon interface may also contribute to axonal conduction deficits and neuronal network dysfunction in AD.

Our proteomics findings of enriched signaling pathways involved in axonal growth, vesicle fusion and dysregulated lipid metabolism (Figs. 4 and 5) may reflect the progression of axonal enlargement, endolysosomal vesicle accumulation at spheroids and concurrent spheroid myelination and myelin disruption (Extended Data Fig. 10). Notably, CASPR-labeled paranode-associated proteomics revealed striking differences between AD and controls in both humans and mice (Fig. 3a–d and Extended Data Fig. 5). In human AD, 804 proteins were detected versus 179 proteins in age-matched controls (Fig. 3b,d), with a similar pattern in 5XFAD mice (Fig. 3b,d and Extended Data Fig. 5). This marked increase likely reflects ongoing myelin–axon disruption, plasticity and repair processes[84,100,101], as supported by our observations of paranodal structural abnormalities and loss in AD (Fig. 1j–o). Furthermore, aberrant myelination and disrupted paranodal/juxtaparanodal structures in AD (Fig. 8) may lead CASPR-based proteomics to capture some proteins from adjacent regions. The detection of signaling pathways related to axonal spheroids, such as axonal outgrowth and vesicle fusion (Figs. 4 and 5), may therefore reflect the myelination of spheroids with associated CASPR expression (Fig. 8). However, paranodes associated with axonal spheroids represent only a small fraction of the total paranode population (less than 3%; Fig. 8i), indicating that the CASPR-labeled proteomic hits primarily reflect widespread paranodal disruption rather than solely the fraction associated with spheroids. Nonetheless, the paranode-enriched proteome included proteins specific to the juxtaparanode and the node of Ranvier, such as CNTN2 (juxtaparanode protein), TNR and NCAN (extracellular matrix proteins at the node of Ranvier) (Fig. 3e,f and Supplementary Table 1). This may result from minor protein intermixing at the juxtaparanode and node of Ranvier boundaries or reflect the limits of resolution of the biotinylation reaction, although STED imaging (at ~50-nm resolution) confirmed localized biotinylation (Extended Data Fig. 3).

Altogether, our study defined the molecular architecture and structural abnormalities of the myelin–axon interface at subcellular resolution, revealing striking differences in AD. We demonstrated that this interface is a critical site of protein aggregation and cellular vulnerability, with important implications for the progression of axonal pathology and neural circuit disruption. Furthermore, the altered signaling pathways and ligand–receptor interactions we uncovered offer new mechanistic and therapeutic insights for future investigation.

Online content

Any methods, additional references, Nature Portfolio reporting summaries, source data, extended data, supplementary information, acknowledgements, peer review information; details of author contributions and competing interests; and statements of data and code availability are available at https://doi.org/10.1038/s41593-025-01973-8.

References

1. Lubetzki, C., Sol-Foulon, N. & Desmazieres, A. Nodes of Ranvier during development and repair in the CNS. *Nat. Rev. Neurol.* **16**, 426–439 (2020).
2. Nave, K. A. & Werner, H. B. Ensheathment and myelination of axons: evolution of glial functions. *Annu. Rev. Neurosci.* **44**, 197–219 (2021).
3. Monje, M. Myelin plasticity and nervous system function. *Annu. Rev. Neurosci.* **41**, 61–76 (2018).
4. Hill, R. A., Li, A. M. & Grutzendler, J. Lifelong cortical myelin plasticity and age-related degeneration in the live mammalian brain. *Nat. Neurosci.* **21**, 683–695 (2018).

5. McKenzie, I. A. et al. Motor skill learning requires active central myelination. *Science* **346**, 318–322 (2014).
6. Pan, S. et al. Preservation of a remote fear memory requires new myelin formation. *Nat. Neurosci.* **23**, 487–499 (2020).
7. Snaidero, N. et al. Myelin replacement triggered by single-cell demyelination in mouse cortex. *Nat. Commun.* **11**, 4901 (2020).
8. Arancibia-Carcamo, I. L. et al. Node of Ranvier length as a potential regulator of myelinated axon conduction speed. *eLife* **6**, e23329 (2017).
9. Knowles, J. K. et al. Maladaptive myelination promotes generalized epilepsy progression. *Nat. Neurosci.* **25**, 596–606 (2022).
10. Chen, W. T. et al. Spatial transcriptomics and in situ sequencing to study Alzheimer's disease. *Cell* **182**, 976–991 e19 (2020).
11. Mathys, H. et al. Single-cell transcriptomic analysis of Alzheimer's disease. *Nature* **570**, 332–337 (2019).
12. Leng, K. et al. Molecular characterization of selectively vulnerable neurons in Alzheimer's disease. *Nat. Neurosci.* **24**, 276–287 (2021).
13. Lau, S. F. et al. Single-nucleus transcriptome analysis reveals dysregulation of angiogenic endothelial cells and neuroprotective glia in Alzheimer's disease. *Proc. Natl Acad. Sci. USA* **117**, 25800–25809 (2020).
14. Zhou, Y. et al. Human and mouse single-nucleus transcriptomics reveal TREM2-dependent and TREM2-independent cellular responses in Alzheimer's disease. *Nat. Med.* **26**, 131–142 (2020).
15. Grubman, A. et al. A single-cell atlas of entorhinal cortex from individuals with Alzheimer's disease reveals cell-type-specific gene expression regulation. *Nat. Neurosci.* **22**, 2087–2097 (2019).
16. Johnson, E. C. B. et al. Large-scale deep multi-layer analysis of Alzheimer's disease brain reveals strong proteomic disease-related changes not observed at the RNA level. *Nat. Neurosci.* **25**, 213–225 (2022).
17. Johnson, E. C. B. et al. Large-scale proteomic analysis of Alzheimer's disease brain and cerebrospinal fluid reveals early changes in energy metabolism associated with microglia and astrocyte activation. *Nat. Med.* **26**, 769–780 (2020).
18. Bai, B. et al. Proteomic landscape of Alzheimer's disease: novel insights into pathogenesis and biomarker discovery. *Mol. Neurodegener.* **16**, 55 (2021).
19. Askenazi, M. et al. Compilation of reported protein changes in the brain in Alzheimer's disease. *Nat. Commun.* **14**, 4466 (2023).
20. Mayer, M. C. & Meinl, E. Glycoproteins as targets of autoantibodies in CNS inflammation: MOG and more. *Ther. Adv. Neurol. Disord.* **5**, 147–159 (2012).
21. Chang, K. J. et al. Glial ankyrins facilitate paranodal axoglial junction assembly. *Nat. Neurosci.* **17**, 1673–1681 (2014).
22. Ho, T. S. et al. A hierarchy of ankyrin-spectrin complexes clusters sodium channels at nodes of Ranvier. *Nat. Neurosci.* **17**, 1664–1672 (2014).
23. Simons, M. & Nave, K. A. Oligodendrocytes: myelination and axonal support. *Cold Spring Harb. Perspect. Biol.* **8**, a020479 (2015).
24. Dutta, D. J. et al. Regulation of myelin structure and conduction velocity by perinodal astrocytes. *Proc. Natl Acad. Sci. USA* **115**, 11832–11837 (2018).
25. Yuan, P. et al. PLD3 affects axonal spheroids and network defects in Alzheimer's disease. *Nature* **612**, 328–337 (2022).
26. Safaiyan, S. et al. Age-related myelin degradation burdens the clearance function of microglia during aging. *Nat. Neurosci.* **19**, 995–998 (2016).
27. Dean, D. C. et al. Association of amyloid pathology with myelin alteration in preclinical Alzheimer disease. *JAMA Neurol.* **74**, 41–49 (2017).
28. Wang, Q. et al. Quantification of white matter cellularity and damage in preclinical and early symptomatic Alzheimer's disease. *Neuroimage Clin.* **22**, 101767 (2019).
29. Nasrabady, S. E. et al. White matter changes in Alzheimer's disease: a focus on myelin and oligodendrocytes. *Acta Neuropathol. Commun.* **6**, 22 (2018).
30. Araque Caballero, M. A. et al. White matter diffusion alterations precede symptom onset in autosomal dominant Alzheimer's disease. *Brain* **141**, 3065–3080 (2018).
31. Kramer-Albers, E. M. & Werner, H. B. Mechanisms of axonal support by oligodendrocyte-derived extracellular vesicles. *Nat. Rev. Neurosci.* **24**, 474–486 (2023).
32. Cai, Y. et al. Subcellular proteomics and iPSC modeling uncover reversible mechanisms of axonal pathology in Alzheimer's disease. *Nat. Aging* **5**, 504–527 (2025).
33. Hashimoto, N. et al. Proteomic analysis of ganglioside-associated membrane molecules: substantial basis for molecular clustering. *Proteomics* **12**, 3154–3163 (2012).
34. Bar, D. Z. et al. Biotinylation by antibody recognition—a method for proximity labeling. *Nat. Methods* **15**, 127–133 (2018).
35. Vallat, J. M. et al. Contactin-associated protein 1 (CNTNAP1) mutations induce characteristic lesions of the paranodal region. *J. Neuropathol. Exp. Neurol.* **75**, 1155–1159 (2016).
36. Bartsch, U., Kirchhoff, F. & Schachner, M. Immunohistological localization of the adhesion molecules L1, N-CAM, and MAG in the developing and adult optic nerve of mice. *J. Comp. Neurol.* **284**, 451–462 (1989).
37. Quarles, R. H. Myelin-associated glycoprotein (MAG): past, present and beyond. *J. Neurochem.* **100**, 1431–1448 (2007).
38. Erb, M. et al. Unraveling the differential expression of the two isoforms of myelin-associated glycoprotein in a mouse expressing GFP-tagged S-MAG specifically regulated and targeted into the different myelin compartments. *Mol. Cell. Neurosci.* **31**, 613–627 (2006).
39. Li, J. et al. Cell-surface proteomic profiling in the fly brain uncovers wiring regulators. *Cell* **180**, 373–386 e15 (2020).
40. Gargareta, V. I. et al. Conservation and divergence of myelin proteome and oligodendrocyte transcriptome profiles between humans and mice. *eLife* **11**, e77019 (2022).
41. Paczkowska, M. et al. Integrative pathway enrichment analysis of multivariate omics data. *Nat. Commun.* **11**, 735 (2020).
42. Slobodyanyuk, M. et al. Directional integration and pathway enrichment analysis for multi-omics data. *Nat. Commun.* **15**, 5690 (2024).
43. Tsuchimochi, R. et al. Viral delivery of L1CAM promotes axonal extensions by embryonic cerebral grafts in mouse brain. *Stem Cell Rep.* **18**, 899–914 (2023).
44. Schafer, M. K. & Frotscher, M. Role of L1CAM for axon sprouting and branching. *Cell Tissue Res.* **349**, 39–48 (2012).
45. Itoh, K. et al. Disrupted Schwann cell-axon interactions in peripheral nerves of mice with altered L1-integrin interactions. *Mol. Cell. Neurosci.* **30**, 131–136 (2005).
46. Guo, D. et al. A disintegrin and metalloproteinase 10 (ADAM10) is essential for oligodendrocyte precursor development and myelination in the mouse brain. *Mol. Neurobiol.* **60**, 1675–1689 (2023).
47. Chen, Y. Y. et al. Targeting of retinal axons requires the metalloproteinase ADAM10. *J. Neurosci.* **27**, 8448–8456 (2007).
48. Kuhn, P. H. et al. Systematic substrate identification indicates a central role for the metalloprotease ADAM10 in axon targeting and synapse function. *eLife* **5**, e12748 (2016).
49. Romi, E. et al. ADAM metalloproteases promote a developmental switch in responsiveness to the axonal repellant Sema3A. *Nat. Commun.* **5**, 4058 (2014).
50. Bregin, A. et al. Expression and impact of Lsamp neural adhesion molecule in the serotonergic neurotransmission system. *Pharmacol. Biochem. Behav.* **198**, 173017 (2020).

51. Thelen, K. et al. Translation of the cell adhesion molecule ALCAM in axonal growth cones – regulation and functional importance. *J. Cell Sci.* **125**, 1003–1014 (2012).
52. Thelen, K. et al. Depending on its nano-spacing, ALCAM promotes cell attachment and axon growth. *PLoS ONE* **7**, e40493 (2012).
53. Sharma, K. et al. Cell type- and brain region-resolved mouse brain proteome. *Nat. Neurosci.* **18**, 1819–1831 (2015).
54. Zhang, J. et al. ACSL4: a double-edged sword target in multiple myeloma, promotes cell proliferation and sensitizes cell to ferroptosis. *Carcinogenesis* **44**, 242–251 (2023).
55. Zhou, T. et al. A mammalian NudC-like protein essential for dynein stability and cell viability. *Proc. Natl Acad. Sci. USA* **103**, 9039–9044 (2006).
56. Efremova, M. et al. CellPhoneDB: inferring cell-cell communication from combined expression of multi-subunit ligand-receptor complexes. *Nat. Protoc.* **15**, 1484–1506 (2020).
57. Jin, S. et al. Inference and analysis of cell-cell communication using CellChat. *Nat. Commun.* **12**, 1088 (2021).
58. Dimitrov, D. et al. Comparison of methods and resources for cell-cell communication inference from single-cell RNA-seq data. *Nat. Commun.* **13**, 3224 (2022).
59. Weidemuller, P. et al. Transcription factors: bridge between cell signaling and gene regulation. *Proteomics* **21**, e2000034 (2021).
60. Browaeys, R., Saelens, W. & Saeys, Y. NicheNet: modeling intercellular communication by linking ligands to target genes. *Nat. Methods* **17**, 159–162 (2020).
61. Dwork, A. J., Schon, E. A. & Herbert, J. Nonidentical distribution of transferrin and ferric iron in human brain. *Neuroscience* **27**, 333–345 (1988).
62. Gerber, M. R. & Connor, J. R. Do oligodendrocytes mediate iron regulation in the human brain? *Ann. Neurol.* **26**, 95–98 (1989).
63. Cheli, V. T. et al. Transferrin receptor is necessary for proper oligodendrocyte iron homeostasis and development. *J. Neurosci.* **43**, 3614–3629 (2023).
64. Li, Y. et al. Transferrin receptor and ferritin-H are developmentally regulated in oligodendrocyte lineage cells. *Neural Regen. Res.* **8**, 6–12 (2013).
65. Espinosa de los Monteros, A. et al. Transferrin is an essential factor for myelination. *Neurochem. Res.* **24**, 235–248 (1999).
66. Mietto, B. S. et al. Schwann cells provide iron to axonal mitochondria and its role in nerve regeneration. *J. Neurosci.* **41**, 7300–7313 (2021).
67. Zhu, X. et al. Mutations in a P-type ATPase gene cause axonal degeneration. *PLoS Genet.* **8**, e1002853 (2012).
68. Kaneshiro, N. et al. Lipid flippase dysfunction as a therapeutic target for endosomal anomalies in Alzheimer's disease. *iScience* **25**, 103869 (2022).
69. Cali, T. et al. A novel mutation in isoform 3 of the plasma membrane Ca^{2+} pump impairs cellular Ca^{2+} homeostasis in a patient with cerebellar ataxia and laminin subunit 1α mutations. *J. Biol. Chem.* **290**, 16132–16141 (2015).
70. Lecuyer, M. A. et al. Dual role of ALCAM in neuroinflammation and blood-brain barrier homeostasis. *Proc. Natl Acad. Sci. USA* **114**, E524–E533 (2017).
71. Kunkle, B. W. et al. Novel Alzheimer disease risk loci and pathways in African American individuals using the African Genome Resources Panel: a meta-analysis. *JAMA Neurol.* **78**, 102–113 (2021).
72. Zhao, L. et al. Alteration of the unfolded protein response modifies neurodegeneration in a mouse model of Marinesco-Sjogren syndrome. *Hum. Mol. Genet.* **19**, 25–35 (2010).
73. Rao, S. et al. Biological function of HYOU1 in tumors and other diseases. *Onco Targets Ther.* **14**, 1727–1735 (2021).
74. Zhu, Z. Y. et al. Mitochondrial aldehyde dehydrogenase (ALDH2) rescues cardiac contractile dysfunction in an APP/PS1 murine model of Alzheimer's disease via inhibition of ACSL4-dependent ferroptosis. *Acta Pharmacol. Sin.* **43**, 39–49 (2022).
75. Jia, B. et al. ACSL4-mediated ferroptosis and its potential role in central nervous system diseases and injuries. *Int. J. Mol. Sci.* **24**, 10021 (2023).
76. Hohn, L. et al. Extracellular matrix changes in subcellular brain fractions and cerebrospinal fluid of Alzheimer's disease patients. *Int. J. Mol. Sci.* **24**, 5532 (2023).
77. Zhang, Q. et al. Human brain glycoform coregulation network and glycan modification alterations in Alzheimer's disease. *Sci. Adv.* **10**, eadk6911 (2024).
78. Chu, T. H. et al. Axonal and myelinic pathology in 5xFAD Alzheimer's mouse spinal cord. *PLoS ONE* **12**, e0188218 (2017).
79. Sarkar, D. et al. Revealing nanostructures in brain tissue via protein decrowding by iterative expansion microscopy. *Nat. Biomed. Eng.* **6**, 1057–1073 (2022).
80. Chapman, T. W. et al. Oligodendrocyte maturation alters the cell death mechanisms that cause demyelination. *J. Neurosci.* **44**, e1794232024 (2024).
81. Griffiths, I. et al. Axonal swellings and degeneration in mice lacking the major proteolipid of myelin. *Science* **280**, 1610–1613 (1998).
82. Ogawa, Y. & Rasband, M. N. Proteomic analysis of optic nerve lipid rafts reveals new paranodal proteins. *J. Neurosci. Res.* **87**, 3502–3510 (2009).
83. Bartzokis, G. Age-related myelin breakdown: a developmental model of cognitive decline and Alzheimer's disease. *Neurobiol. Aging* **25**, 5–18 (2004).
84. Chen, J. F. et al. Enhancing myelin renewal reverses cognitive dysfunction in a murine model of Alzheimer's disease. *Neuron* **109**, 2292–2307 e5 (2021).
85. Depp, C. et al. Myelin dysfunction drives amyloid-β deposition in models of Alzheimer's disease. *Nature* **618**, 349–357 (2023).
86. Kedia, S. et al. T cell-mediated microglial activation triggers myelin pathology in a mouse model of amyloidosis. *Nat. Neurosci.* **27**, 1468–1474 (2024).
87. Auer, F., Vagionitis, S. & Czopka, T. Evidence for myelin sheath remodeling in the CNS revealed by in vivo imaging. *Curr. Biol.* **28**, 549–559 e3 (2018).
88. Osso, L. A. & Hughes, E. G. Dynamics of mature myelin. *Nat. Neurosci.* **27**, 1449–1461 (2024).
89. Guo, Q. et al. Amyloid precursor protein revisited: neuron-specific expression and highly stable nature of soluble derivatives. *J. Biol. Chem.* **287**, 2437–2445 (2012).
90. Skaper, S. D. et al. Oligodendrocytes are a novel source of amyloid peptide generation. *Neurochem. Res.* **34**, 2243–2250 (2009).
91. Zheng, H. & Koo, E. H. The amyloid precursor protein: beyond amyloid. *Mol. Neurodegener.* **1**, 5 (2006).
92. Rajani, R. M. et al. Selective suppression of oligodendrocyte-derived amyloid beta rescues neuronal dysfunction in Alzheimer's disease. *PLoS Biol.* **22**, e3002727 (2024).
93. Sasmita, A. O. et al. Oligodendrocytes produce amyloid-β and contribute to plaque formation alongside neurons in Alzheimer's disease model mice. *Nat. Neurosci.* **27**, 1668–1674 (2024).
94. Jankowsky, J. L. et al. Mutant presenilins specifically elevate the levels of the 42 residue β-amyloid peptide in vivo: evidence for augmentation of a 42-specific γ secretase. *Hum. Mol. Genet* **13**, 159–170 (2004).
95. Almeida, R. G. et al. Myelination of neuronal cell bodies when myelin supply exceeds axonal demand. *Curr. Biol.* **28**, 1296–1305 e5 (2018).

96. Fard, M. K. et al. BCAS1 expression defines a population of early myelinating oligodendrocytes in multiple sclerosis lesions. *Sci. Transl. Med.* **9**, eaam7816 (2017).
97. Barres, B. A., Lazar, M. A. & Raff, M. C. A novel role for thyroid hormone, glucocorticoids and retinoic acid in timing oligodendrocyte development. *Development* **120**, 1097–1108 (1994).
98. Barres, B. A. et al. Cell death and control of cell survival in the oligodendrocyte lineage. *Cell* **70**, 31–46 (1992).
99. Garcia-Fresco, G. P. et al. Disruption of axo-glial junctions causes cytoskeletal disorganization and degeneration of Purkinje neuron axons. *Proc. Natl Acad. Sci. USA* **103**, 5137–5142 (2006).
100. Quintela-Lopez, T. et al. Aβ oligomers promote oligodendrocyte differentiation and maturation via integrin β1 and Fyn kinase signaling. *Cell Death Dis.* **10**, 445 (2019).
101. Chapman, T. W. et al. Oligodendrocyte death initiates synchronous remyelination to restore cortical myelin patterns in mice. *Nat. Neurosci.* **26**, 555–569 (2023).

[1]Department of Neurology, Yale University, New Haven, CT, USA. [2]European Molecular Biology Laboratory, European Bioinformatics Institute, Hinxton, UK. [3]Computational Biology Program, Ontario Institute for Cancer Research, Toronto, Ontario, Canada. [4]Department of Medical Biophysics, University of Toronto, Toronto, Ontario, Canada. [5]Keck MS & Proteomics Resource, Yale University, New Haven, CT, USA. [6]Department of Cell Biology, Yale University School of Medicine, New Haven, CT, USA. [7]Yale College, Yale University, New Haven, CT, USA. [8]Department of Pathology, Yale University, New Haven, CT, USA. [9]Department of Molecular Biophysics and Biochemistry, Yale University, New Haven, CT, USA. [10]Yale/NIDA Neuroproteomics Center, Yale University, New Haven, CT, USA. [11]Department of Molecular Genetics, University of Toronto, Toronto, Ontario, Canada. [12]Department of Psychiatry, Yale University, New Haven, CT, USA. [13]Department of Pharmacology, Yale University, New Haven, CT, USA. [14]Department of Neuroscience, Yale University, New Haven, CT, USA. [15]Wu Tsai Institute, Yale University, New Haven, CT, USA. [16]Present address: Department of Rehabilitation Medicine, Huashan Hospital, State Key Laboratory of Medical Neurobiology, Institute for Translational Brain Research, MOE Frontiers Center for Brain Science, MOE Innovative Center for New Drug Development of Immune Inflammatory Diseases, Fudan University, Shanghai, China. [17]These authors contributed equally: Iguaracy Pinheiro-de-Sousa, Mykhaylo Slobodyanyuk, Fuyi Chen. ✉e-mail: yifei.cai@yale.edu; jaime.grutzendler@yale.edu

Methods

Mice

All animal procedures were approved by the Institutional Animal Care and Use Committee at Yale University (IACUC protocol 2023-11438). Animals were housed at the Yale University Animal Facility, with a 12-h light/12-h dark cycle, temperature 18.3–23.9 °C and 40–60% humidity. Wild-type (WT) (C57BL/6J) mice, 5XFAD (Tg6799) mice[102], Thy1-YFP mice (JAX cat. no. 003709)[103] and CNP-EGPF mice (JAX cat. no. 026105) were obtained from the Jackson Laboratory. For proximity labeling proteomics, 15-month-old 5XFAD mice were euthanized followed by transcardial perfusion. Three male mice per genotype (WT and 5XFAD) were used. Animals used for immunofluorescence validation were euthanized at 12–15 months of age, with three biological replicates per experiment. Both male and female mice were used. Brain slices obtained from the mouse posterior somatosensory cortex were used for proteomics, immunofluorescence staining, ExM and electron microscopy experiments.

Human postmortem brain tissue

Fixed and snap-frozen postmortem human frontal cortices from patients with AD and age-matched controls were obtained from the Yale ADRC, the Banner Institute and the NIH NBB. Detailed demographic and clinical information can be found in Supplementary Fig. 1. Four AD cases and four age-matched unaffected controls were analyzed by proximity labeling proteomics. For immunofluorescence experiments, six to ten biological replicates of human AD and control specimens were used.

Antibodies

Anti-LAMP1 antibody (1:200, DSHB, 1D4B, RRID:AB_2134500) was used to label axonal spheroids in mice. Anti-PLD3 antibody (1:250, Atlas Antibodies, cat. no. HPA012800, RRID: AB_1855330) was used to label axonal spheroids in humans. SMI312 antibody (1:500, BioLegend, RRID:AB_2566782) or NFH (1:1,000, EnCor cat. no. CPCA-NF-H, RRID: AB_2149761) was used to label neurofilament in both humans and mice. CASPR antibody (1:600, abcam, cat. no. ab34151, RRID:AB_869934) was used to label paranodes in both humans and mice. Myelin PLP (1:1,000, Bio-Rad, cat. no. MCA839G, RRID:AB_2237198), PLP (1:200, abcam, cat. no. ab254363, RRID:AB_3095302), CNPase (1:1,000, BioLegend, cat. no. 836404, RRID:AB_2728547) and MBP (1:200, Millipore, cat. no. AB9348, RRID: AB_11213157) antibodies were used to label myelin in mice and humans. 4G8 antibody (1:200, BioLegend, cat. no. 800701, RRID:AB_2564633) and 6e10 antibody (1:200, BioLegend, cat. no. 803001, RRID: AB_2564653) were used to label amyloid plaques and amyloid fibers. Anti-GFP antibody (1:500, Aves Labs, RRID:AB_10000240) was used to label Thy1-YFP neurons or CNP-EGFP myelin in mice. BCAS1 antibody (1:1,000, Synaptic Systems, cat. no. 445 003, RRID: AB_2864793) was used to labeled newly formed myelinating oligodendrocytes. Kv 7.3 antibody (1:200, Synaptic Systems, cat. no. 368 003, RRID: AB_2620129) was used to label juxtaparanode. ATP8A1 (1:200, Atlas Antibodies, cat. no. HPA052935, RRID: AB_2681992), ATP2B3 (1:200, Atlas Antibodies, cat. no. HPA001583, RRID: AB_1079641), L1CAM (1:200, Millipore, cat. no. MAB5272, RRID: AB_2133200), TF (1:200, Proteintech, cat. no. 17435-1-AP, RRID: AB_2035023), NRXN3 (1:200, Atlas Antibodies, cat. no. HPA002727, RRID: AB_1079468), ALCAM (1:200, Novus, cat. no. AF1172, RRID: AB_354644), LSAMP (1:200, Atlas Antibodies, cat. no. HPA076122, RRID: AB_2686779), HAPLN1 (1:200, Atlas Antibodies, cat. no. HPA019105, RRID: AB_1850496), NUDCD3 (1:200, Atlas Antibodies, cat. no. HPA019136, RRID: AB_1852370), HYOU1 (1:200, Invitrogen, cat. no. PA5-27655, RRID: AB_2545131), ACSL4 (1:200, Invitrogen, cat. no. PA5-27137, RRID: AB_2544613) and GRK2 (1:200, Invitrogen, cat. no. MA5-15840, RRID: AB_11152830) antibodies were used to label top proteomic hits in humans postmortem brains. Alexa dye-conjugated secondary antibodies were used (1:600, ThermoFisher, cat. nos. A32790, A-31572, A-31573, A32773, A-31570, A-31571, A-21447). PLD3, PLP, MBP, Kv7.3, ATP8A1, TF, ATP2B3, L1CAM, NRXN3, ALCAM, LSAMP, HAPLN1, NUDCD3, HYOU1 and GRK2 antibodies require antigen retrieval treatment of human and mouse tissues. 4G8 and 6e10 antibodies require formic acid treatment before immunofluorescence staining. See the 'Immunofluorescence of fixed specimens' section.

Proximity labeling in human and mouse brain tissues

Paranodal proteins or myelin–axon interface proteins were proximity labeled using anti-CASPR or anti-MAG antibodies, respectively, in humans and mice. No-antibody was used as control in this study, except in Supplementary Fig. 12. Anti-HA tag antibody was used as another control, to compare with the results from no-antibody samples. Briefly, mouse brains were fixed in 4% paraformaldehyde at 4 °C for 22–24 h with shaking. For human tissue, frozen postmortem human brain specimens were fixed by submerging into ice-cold 4% paraformaldehyde, with shaking at 4 °C for 22–24 h. Mouse and human brain sections were vibratome sectioned at 50-µm thickness. Ten sections were used for each biological replicate. Four biological replicates of human AD or age-matched unaffected control samples were used. Three mouse biological replicates were used in each group. Sections were permeabilized by PBS with 0.5% Triton X-100 for 7 min, followed by rinsing with PBST (0.1% Tween-20 in PBS). Then, sections were incubated in 0.1% H_2O_2 for 10 min, followed by rinsing with PBST twice. Primary antibody in blocking buffer (0.1% Tween-20 with 1% BSA in PBS) was incubated for 12 h at 4 °C on a shaker, followed by PBST washes three times for 20 min per wash. Secondary antibody conjugated with HRP was incubated in blocking buffer for 1 h at room temperature, followed by PBST washes three times for ~40 min per wash. Proximity labeling was performed using Biotin-XX-Tyramide (ThermoFisher, cat. no. B40951) dissolved in 50 mM Tris-HCl buffer (pH 7.4) with H_2O_2 for 4 min. Biotinylation reactions were terminated by rinsing sections with freshly made 500 mM sodium ascorbate three times, followed by PBST washes three times.

Pull-down of biotinylated proteins

Brain sections from proximity labeling experiments were lysed and de-crosslinked in 100 mM Tris-HCl buffer (pH 8.0) with 2% SDS and protease inhibitor (Roche) at 95 °C for 45 min with constant shaking. For every ten brain sections, 500 µl of lysis buffer was used. Protein lysate was sonicated using a Sonic Dismembrator Model 500 (ThermoFisher) at 4 °C, 3 s per time, three times. Protein lysate was centrifuged at 12,000*g* for 5 min. Then, 450 µl of protein lysate supernatant was collected from each sample, incubated with 550 µl of PBST containing 200 µl of prewashed streptavidin magnetic beads (ThermoFisher, cat. no. 88817) and protease inhibitor (Roche, cat. no. 11836170001) and put on a 360° rotator at 4 °C overnight. The rest of the protein lysate was used for protein concentration measurement by BCA (ThermoFisher). Beads were then sequentially washed once with PBST, twice with PBST with 1 M NaCl and twice with PBS. Biotinylated proteins were then eluted with 20 µl of 20 mM dithiothreitol (DTT) and 2 mM biotin in 1 × LDS lysis buffer (ThermoFisher, cat. no. NP0007) with protease inhibitor at 95 °C for 5 min. Supernatant was collected and centrifuged at 12,000*g* for 1 min, followed by running into a 4–20% Tris-Glycine gel (Invitrogen, cat. no. XP04205BOX) at a constant voltage of 150 V until all the proteins had run into the gel (approximately 10 min). Gels were rinsed once in ultrapure water (AmericanBio) and incubated in ~50 ml of Coomassie blue R-250 staining solution (Bio-Rad) three times, for 30 min per incubation. Gels were de-stained with Coomassie blue R-250 destaining solution (Bio-Rad) for 2 h with three buffer changes. Gel pieces containing protein samples were visualized, cut with clean razor blades and kept at −20 °C before the next step.

Western blotting

For western blot, 4–20% Tris-Glycine gels (Invitrogen, cat. no. XP04205BOX) were used for protein electrophoresis following the

manufacturer's protocol. Proteins were transferred to nitrocellulose membranes (Bio-Rad). After blocking with 5% BSA in TBST (Tris-buffered saline with 0.1% Tween-20) for 1 h, membranes were incubated with primary antibodies diluted in 5% BSA in TBST on a shaker at 4 °C overnight, followed by three 5-min washes with TBST. Membranes were then incubated with HRP-conjugated secondary antibodies diluted in 3% BSA in TBST for 1 h at room temperature, followed by three 5-min washes with TBST. To blot biotinylated proteins, HRP-conjugated streptavidin was used. Clarity Western ECL blotting substrate (Bio-Rad) and a ChemiDoc MP imaging system (Bio-Rad) were used for chemiluminescence development and detection. Silver stain (Pierce, cat. no. 24612) was carried out after electrophoresis according to the user manual.

In-gel digestion

Gel slices were cut into small pieces and washed with 600 µl of water on a tilt-table for 10 min followed by a 20-min wash with 600 µl of 50% acetonitrile (ACN)/100 mM NH_4HCO_3 (ammonium bicarbonate, ABC). The samples were reduced by the addition of 100 µl of 4.5 mM DTT in 100 mM ABC with incubation at 37 °C for 20 min. The DTT solution was removed, and the samples were cooled to room temperature. The samples were alkylated by the addition of 100 µl of 10 mM iodoacetamide (IAN) in 100 mM ABC with incubation at room temperature in the dark for 20 min. The IAN solution was removed, and the gels were washed for 20 min with 600 µl of 50% ACN/100 mM ABC, then washed for 20 min with 600 µl of 50% ACN/25 mM ABC. The gels were briefly dried by SpeedVac, then resuspended in 100 µl of 25 mM ABC containing 500 ng of digestion-grade trypsin (Promega, cat. no. V5111), and incubated at 37 °C for 16 h. The supernatants containing the tryptic peptides were transferred to new Eppendorf tubes. Residual peptides in the gel bands were extracted with 250 µl of 80% ACN/0.1% trifluoroacetic acid (TFA) for 15 min, then combined with the original digests and dried in a SpeedVac. Peptides were dissolved in 24 µl of mass spectrometry (MS) loading buffer (2% ACN, 0.2% TFA), with 5 µl injected for LC–MS/MS analysis.

LC–MS/MS on the ThermoFisher Q Exactive Plus

LC–MS/MS analysis was performed on a ThermoFisher Q Exactive Plus equipped with a Waters nanoAcquity UPLC system utilizing a binary solvent system (A: 100% water, 0.1% formic acid; B: 100% ACN, 0.1% formic acid). Trapping was performed at 5 µl min^{-1}, 99.5% Buffer A for 3 min using an ACQUITY UPLC M-Class Symmetry C18 Trap Column (100 Å, 5 µm, 180 µm × 20 mm, 2 G, V/M; Waters, cat. no. 186007496). Peptides were separated at 37 °C using an ACQUITY UPLC M-Class Peptide BEH C18 Column (130 Å, 1.7 µm, 75 µm × 250 mm; Waters, cat. no. 186007484) and eluted at 300 nl min^{-1} with the following gradient: 3% buffer B at initial conditions; 5% B at 2 min; 25% B at 140 min; 40% B at 165 min; 90% B at 170 min; 90% B at 180 min; return to initial conditions at 182 min. MS spectra were acquired in profile mode over the 300–1,700 *m/z* range using 1 microscan, 70,000 resolution, automatic gain control (AGC) target of 3×10^6 and a maximum injection time of 45 ms. Data-dependent tandem MS (MS/MS) spectra were acquired in centroid mode on the top 20 precursors per MS scan using 1 microscan, 17,500 resolution, AGC target of 1×10^5, maximum injection time of 100 ms and an isolation window of 1.7 *m/z*. Precursors were fragmented by higher-energy collision-induced dissociation (HCD) activation with a collision energy of 28%. MS/MS spectra were collected on species with an intensity threshold of 1×10^4, charge states 2–6 and peptide match preferred. Dynamic exclusion was set to 30 s.

Peptide identification

Data were analyzed using Proteome Discoverer software v.2.2 (ThermoFisher). Data searching was performed using the Mascot algorithm (v.2.6.1) (Matrix Science) against the SwissProtein database with taxonomy restricted to human (20,368 sequences) or mouse (17,034 sequences) as well as a streptavidin sequence. The search parameters included tryptic digestion with up to two missed cleavages, 10-ppm precursor mass tolerance and 0.02-Da fragment mass tolerance, and variable (dynamic) modifications of methionine oxidation and carbamidomethyl cysteine. Normal and decoy database searches were run, with the confidence level set to 95% ($P < 0.05$). Scaffold v.5.1.2 (Proteome Software) was used to validate MS/MS-based peptide and protein identifications. Peptide identifications were accepted if they could be established at greater than 95.0% probability by the Scaffold Local FDR algorithm. Protein identifications were accepted if they could be established at greater than 99.0% probability and contained at least two identified peptides (one uniquely assignable to the protein). Proteins that contained similar peptides and could not be differentiated based on MS/MS analysis alone were grouped to satisfy the principles of parsimony. Proteins sharing significant peptide evidence were grouped into clusters. Label-free quantification was performed with Scaffold software. Spectral intensity values were used for protein quantification between groups.

Proteomic data analysis

To analyze the proteomic data, we first used Qlucore Omics Explorer v.3.6 (Qlucore) to calculate the fold changes, *P* values and FDRs. According to Qlucore, the fold change was calculated as 2 to the power of the average difference between two groups. For example, fold change (CASPR/noAb) = 2^[(average of CASPR) − (average of noAb)]. We also calculated the ratio between test and control using this formula: ratio (CASPR/noAb) = (average of CASPR)/(average of noAb). To calculate the ratio, a pseudo number of 0.1 was used to replace any spectra count that was detected as '0'. To obtain paranodal proteomes or myelin–axon interface proteomes, we first performed Pearson correlation analysis across samples using GraphPad Prism 9.5.0. Pearson correlation coefficient values were used to evaluate correlations. R^2 greater than 0.7 was set as the cutoff. We found that all the human AD, unaffected control and mouse samples passed the 0.7 cutoff, except an unaffected control human sample (Human no. 7) from the paranode dataset (Extended Data Fig. 4b). Therefore, we removed the sample Human no. 7 from the downstream paranode proteomic analysis. In the myelin–axon interface samples, we observed an unaffected control human specimen (Human no. 20) that showed a much lower correlation to other samples (R^2 between 0.73 and 0.80), whereas correlation among all other samples was much higher (R^2 between 0.83 and 0.98) (Extended Data Fig. 4a). To maximize the number of known true hits in the myelin–axon interface samples, the human unaffected control sample Human no. 20 was excluded from the downstream analysis. Next, differentially expressed proteins were analyzed by two steps: (1) a cutoff analysis and (2) a statistical cutoff. We performed the cutoff analysis as previously described[39]. Briefly, we defined the 'True positive proteins (TPs)', which are very likely to be expressed in paranodes, by extracting the genes that belong to these Gene Ontology Cellular Component terms (GeneOntology.org[104]): 'paranode region of axon', 'juxtaparanode region of axon', 'node of Ranvier', 'axon' and 'myelin sheath', as well as the axoglia-osome proteins that were detected in ref. 105. 'False positive proteins (FPs)' were defined as proteins unlikely to be expressed in paranodes, and were extracted from these Gene Ontology Cellular Component terms (GeneOntology.org[104]): 'nucleus', 'lysosome', 'mitochondria', 'ER', 'golgi', 'extracellular region', 'glial projection' and 'astrocytic projection'. A filter 'false positive protein list' was created by removing the TPs from the FPs (that is, FP − TP). Briefly, cutoff analysis was performed by: (1) comparing CASPR-labeled proteomic hits versus proteins pulled down from no-antibody controls, then calculating fold change and *P* value, and FDR using Qlucore Omics Explorer v.3.6 (Qlucore) with two group comparison; (2) ranking the list of proteins by fold change from the highest to the lowest; (3) defining each protein whether it is a true or false protein; true proteins (column E in Supplementary Fig. 15) were labeled as '1', while others were labeled as '0'; similarly, false proteins (column F in Supplementary Fig. 15), which were in the 'false positive

protein list', were labeled as '1', while others were labeled as '0'; (4) calculate 'true positive rate (TPR)' (column G in Supplementary Fig. 15) and 'false positive rate (FPR)' (column H in Supplementary Fig. 15), by calculating the cumulative number of TPs from the top to the current one, then dividing by the total number of TPs (or FPs) in the dataset; (5) calculating TPR minus FPR (column I in Supplementary Fig. 15); ROC analyses were plotted using TPR and FPR in the proteomic datasets; (6) cutoff analyses were plotted using 'TPR − FPR' and $\log_{10}$(fold change) (Supplementary Fig. 5). Cutoff point was set at the maximum value of 'TPR − FPR'. For statistical cutoff, FDR < 0.05 and fold change > 1 was further applied to the human proteomics datasets of AD and unaffected controls, while a statistical cutoff FDR < 0.1 and fold change > 1 was applied to the mouse proteomics dataset.

Principal component analysis (PCA) was performed using Qlucore Omics Explorer v.3.6 (Qlucore). Subcellular compartment location analysis was performed using the 'All channel integrated' human dataset downloaded from the COMPARTMENTS database[106]. Protein–protein interaction network analysis (Supplementary Fig. 10) was performed using STRING v.11 (ref. 107) and visualized using Cytoscape (v.3.9.1)[108]. Pathway enrichment analyses of biological process and molecular function were performed using the CASPR-labeled or MAG-labeled human unaffected control proteomics datasets. Briefly, biological process and molecular function signatures were analyzed using g:Profiler[109] with no electronic Gene Ontology (GO) annotations, and applied term size filter 5 to 350. For IPA (Fig. 4i), final proteomes (after comparing CASPR-labeled AD humans versus unaffected controls, $P < 0.05$) were imported into IPA software (QIAGEN, 2022 released version)[110] for canonical pathway analysis. The top IPA pathways were retrieved with the lowest FDRs. For comparison of the PAPs or MAPs with the bulk brain tissue protein expression[16] and single-cell RNA expression[11] (Extended Data Fig. 9), upregulated and downregulated proteomic hits ($P < 0.05$) in AD human paranode compared with unaffected controls were used for retrieval of protein expression in bulk proteomics of prefrontal cortex of AD humans and controls, as well as cell-type-specific RNA expressions from snRNA-seq of prefrontal cortex of humans with or without AD pathology.

Additionally, in human brain we noticed that we did not detect MCT1 (SLC16A1) or MCT2 (SLC16A7) in our proteomic datasets, despite these molecules having been reported to be expressed at the myelin–axon interface in mouse brains[111,112], which could be partly explained by the low levels of expression of MCTs in humans[113]. Additionally, both MCT1 and MCT2 may not be compatible with MS detection, based on the peptide sequence annotation from the Uniprot database. Given that MCT1 and MCT2 have very intricate transmembrane tertiary structures, they are low in solubility and this could hinder the MS detection. Furthermore, the cytoplasmic/cellular regions of these two proteins are very short, and therefore would likely generate short tryptic peptides which may have been missed by the mass spectrometer data acquisition settings (for example, fragmentation of 2+ (or higher) peptide charge state in the method setting).

Integrative pathway enrichment analysis of proteomes

To interpret the potential significance of the differentially expressed proteins in the internodal and paranodal myelin–axon interfaces (Fig. 4a,b and Extended Data Fig. 7), we performed an integrative pathway enrichment analysis using the ActivePathways method (FDR < 0.05)[41,42]. As the input to ActivePathways, we used a matrix of *P* values consisting of 3,008 protein-coding genes across two datasets that compose the internode and paranode differential expression analyses between AD and unaffected individuals. Gene sets comprising biological processes and molecular functions of GO[114] and molecular pathways of Reactome[115] were downloaded from the g:Profiler website[116] on 27 March 2023. ActivePathways was run using the following parameters: gene sets with 5 to 300 genes were used, the FDR method was utilized for multiple testing correction and a conservative background set of 3,008 genes was applied to account for proteins detected in the MS experiments. Otherwise, the default parameters of ActivePathways were used. Pathways were visualized as an enrichment map[108] in Cytoscape using standard protocols[117]. Subnetworks were manually organized as functional themes of related pathways. Significant genes in individual pathways were visualized as dot plots with fold change and *P* values.

Public single-cell transcriptomics data analysis

The single-cell data analyzed here[13,16] were analyzed using standard procedures[118], as follows. We applied data pre-processing steps, including filtering out cells expressing fewer than 200 genes and genes expressed in fewer than three cells. Additionally, cells with unique gene counts exceeding 8,000 or falling below 750 were excluded. Cells exhibiting over 10% mitochondrial gene expression, indicating potential poor quality, were also removed. To reduce dimensionality, we conducted PCA on the scaled data. For refined cell clustering, we utilized the FindNeighbors() and FindClusters() functions on the PCA space, computing Euclidean distances between cells to iteratively group those with similar expression patterns. The resulting clusters were visualized using Uniform Manifold Approximation and Projection. To identify cluster markers, we employed the FindMarkers() function, which compared each cluster against all others through differential expression analysis. We selected gene markers with a *P* value of ≤0.05 and an average |$\log_2$Foldchange| of ≥0.25. We used the top cell markers for cell-type annotation combined with the cell markers used from the publications[13,16]. It is worth noting that the primary results and downstream CCC analysis presented in this study were primarily based on the dataset in ref. 13. This dataset contained a considerably larger number of single cells sequenced (42,528 cells from the entorhinal cortex and 63,608 cells from the superior frontal gyrus) and was matched regionally with our proteomics data.

CCC analysis

The CCC analysis aimed to identify ligand–receptor interactions for mapping our subcellular proteomics data. To predict these interactions across various brain cell types, we leveraged multiple resources, including OmniPath, a comprehensive intercellular database[119], CellChatDB[57] and CellPhoneDB database[120]. Our approach involved integrating the results from three distinct methods: CellPhoneDB v.2 (ref. 56), CellChat[57] and LIANA[58]. The input for these methods was the seurat R object containing all the annotated cell types[120]. They assigned probabilities to each interaction through permutation tests. For the three methods, we conducted 1,000 permutations, calculating *P* values for interactions with mean expression levels higher than those expected by random chance. Interactions with *P* values of ≤0.05 were considered significant. To enhance the coverage of our analysis and increase the likelihood of identifying novel ligand–receptor interactions, we merged the outputs of these three methods. This integration was essential due to the diverse databases and resources employed in each method.

Integrated ligand–receptor subcellular proteomics analysis

We conducted an enrichment analysis using the Fisher test to verify whether the protein abundance at the paranode and myelin–axon interface was enriched specifically in CCC processes involving oligodendrocytes and neurons, as opposed to other cell types identified through single-cell-type annotation. For this analysis, we considered all ligand–receptor pairs identified in the CCC results as the universe of proteins. In our contingency table, we categorized proteins as either present in interactions between oligodendrocytes and neurons or present in interactions involving all other cell types. A positive enrichment for oligodendrocyte–neuron specificity was indicated by a *P* value of ≤0.05 and positive residuals (Extended Data Fig. 8c). Subsequently, we refined our subcellular proteomics dataset using the ligand–receptor predictions specific to oligodendrocyte–neuron interactions (Fig. 5b).

To calculate transcription factor activity, we utilized the latest collection of transcription regulatory interactions from CollecTRI[59], applying it to the DEGs in oligodendrocytes and neurons under both AD and control conditions. Subsequently, we performed two rounds of pathway enrichment analysis using the Kyoto Encyclopedia of Genes and Genomes and Gene Ontology of Biological Processes databases. In the first round, we focused on receptors and TFs predicted for each cell type in each condition. The enriched pathways from this analysis were then used to select the DEGs within their respective cell types that belonged to these pathways. In the second round of enrichment analysis, we considered the receptors, TFs and filtered DEGs, aiming to enhance signal quality and reduce noise, instead of using the full list of DEGs (refer to Fig. 5f,g). Pathways were considered enriched if they had an adjusted $P \leq 0.05$, using Benjamini–Hochberg to correct for multiple tests.

Immunofluorescence of fixed specimens

Immunofluorescence staining was performed as we previously described[25,32]. Briefly, mouse brains were fixed in 4% paraformaldehyde at 4 °C for 22–24 h with shaking. For human tissue, frozen postmortem human brain specimens were fixed by submerging into ice-cold 4% paraformaldehyde, and with shaking at 4 °C for 22–24 h. Mouse and human brain sections were vibratome sectioned at 50-µm thickness. Primary antibody incubations were 12 h to 2 d at 4 °C in blocking buffer (PBS with 0.1% Tween-20 and 1% BSA) and then secondary antibodies in blocking buffer for 2 h at room temperature or 4 °C overnight on a shaker. Thioflavin S (Sigma-Aldrich, cat. no. T1892, 2% w/v stock solution, 1:10,000 staining) was used for labeling amyloid deposits before mounting on slides with PermaFluor (ThermoFisher, cat. no. TA-030-FM). Heat-induced sodium citrate antigen retrieval was performed for PLD3 and PLP antibody staining with the following protocol: tissue was boiled in 50 mM sodium citrate with 0.05% Tween-20 at 95 °C for 45 min and washed three times with PBS. Formic acid treatment was performed for 4G8 antibody staining before proceeding to antigen retrieval or other immunofluorescence staining procedures. Briefly, brain sections were submerged into 70% formic acid for 10 min, then rinsed three times with PBS.

ExM

ExM was performed as we previously described[25]. Before expansion, brain sections were placed in PBS and exposed to blue light overnight to quench autofluorescence. The plates with brain sections were placed on a temperature control device to keep the brain section cold at around 4 °C. Next, immunofluorescence staining was performed using mouse or human brain sections according to the methods in the 'Immunofluorescence of fixed specimens' section. Then, brain sections were processed for gelation, digestion and expansion. Briefly, brain sections were first incubated with monomer solution (1 × PBS, 2 M NaCl, 8.625% (w/w) sodium acrylate, 2.5% (w/w) acrylamide, 0.15% (w/w) *N*,*N*′-methylenebisacrylamide) at 4 °C for 45 min. The sections were then transferred into a gel chamber and incubated in gelling solution (concentrated stocks (10%, w/w) of ammonium persulfate initiator and tetramethyl-ethylenediamine accelerator added to the monomer solution up to 0.2% (w/w) each and the inhibitor 4-hydroxy-2,2,6,6-tetramethylpiperidin-1-oxyl added up to 0.01% (w/w) from a 0.5% (w/w) stock) at 37 °C for 2.5 h exactly for gelation. Gels were then digested with digestion buffer (50 mM Tris pH 8.0, 1 mM EDTA, 0.5% Triton X-100, 0.8 M guanidine HCl with protease K 8 units per ml) for 30 min exactly at 37 °C. Next, gel was placed in excess volumes of double-deionized water (double-distilled H_2O) for 10 min to expand. This step was repeated 3–5 times in double-distilled H_2O, until the size of the expanding sample plateaued. Samples were then processed to confocal imaging.

Confocal microscopy

Confocal imaging was performed as we previously described[25,32]. Briefly, a Leica SP8 confocal microscope was used to generate all images. Laser and detector (the GaAsP hybrid detection system, photon counting mode) settings were maintained constant. For all analyses, tiled imaging using a motorized stage was used to image across brain specimens in humans and mice. Human or mouse brain slices were imaged using a ×63 oil immersion objective (NA 1.4) or ×25 water immersion objective (NA 0.95) at 1,024 × 1,024 pixel resolution, *z*-step size of 1 mm (ref. 121). Images were processed with FIJI (ImageJ) software.

TEM

TEM was performed as we previously described[25]. Briefly, 12–15-month-old 5XFAD mice were perfused with PBS and 4% PFA. Fixed human postmortem or mouse brains were sectioned into 50-µm slices using a vibratome (VT1000S, Leica). The slices were refixed in 2% glutaraldehyde in 0.1 M cacodylate buffer (pH 7.4) for 1 h, then post-fixed in 1% OsO_4 in the same buffer at room temperature for 1 h. After en bloc staining with 2% aqueous uranyl acetate for 30 min, tissues were dehydrated in a graded series of ethanol to 100%, followed by propylene oxide, and finally embedded in EMBed 812 resin. Tissue blocks were polymerized overnight in an oven at 60 °C. Thin sections (60 nm) were cut by a Leica ultramicrotome (UC7) and post-stained with 2% uranyl acetate and lead citrate. Sample grids were examined on the FEI Tecnai transmission electron microscope with an accelerating voltage of 80 kV, and digital electron micrographs were recorded with an Olympus Morada CCD camera and iTEM imaging software.

STED imaging

STED imaging was performed as we previously described[122]. Briefly, human postmortem brain tissues were processed with immunofluorescence staining and proximity labeling as described in the 'Proximity labeling in human and mouse brain tissues' and 'Immunofluorescence of fixed specimens' sections, till the point of secondary antibodies and streptavidin labeling. We used STED compatible secondary antibody Atto594 (Sigma-Aldrich) (1:100 dilution) and Atto647N-streptavidin (Sigma-Aldrich) (1:100 dilution) to label the paranodes, internodes and biotinylated proteins, respectively. Tissues were then mounted using Prolong Gold (ThermoFisher) according to the user manual, and kept in the dark at room temperature for 24–72 h before imaging. STED imaging was performed using a Leica SP8 STED 3X equipped with a pulsed white light laser (SuperK Extreme EXW-12; NKT Photonics) for excitation and a 775-nm pulsed laser for depletion (Onefive Katana-08HP). Alignment of the excitation and STED beams was achieved using 200-nm Crimson Fluospheres (ThermoFisher, cat. no. F8782). Sample imaging was performed using the following parameters: Sequence 1: 594 nm at 4% confocal, and laser power was 1.15 µW. The baseline was 0.032 µW. Delta (difference) was around 1.15 µW. Sequence 2: 647 N at 15% confocal, and laser power delta was 6.4 µW. Sequence 3: 647 N at 80% STED, and laser power delta was 34 µW. Sequence 4: 594 nm at 50% STED, and laser power delta was 14 µW.

Statistics and reproducibility

We analyzed myelin, axon and paranode density and size in postmortem human AD brains, age-matched controls and mice using Aivia 11.0.1 (Leica) in an automated and unbiased fashion. Confocal images were deconvolved for better resolution before analysis. Raw images were imported into the software, with scale parameters adjusted based on metadata. Experts classified paranodes and undesirable regions, training machine learning models for accurate recognition. Three-dimensional reconstruction of myelin, axons and paranodes was performed, with pixel segmentation tools and adjustments for optimal segmentation. Parameters such as volume and axis lengths were exported. We applied statistical filters to ensure accurate selection and analysis of paranodes, focusing on size and shape criteria. Final three-dimensional objects were evaluated for statistical significance, with volume and surface area normalized to their respective regions of interest.

Quantification of myelin- or paranode-associated axonal dystrophy size was performed using Fiji ImageJ. Briefly, LAMP1- or PLD3-positive axonal spheroids were circled using the freehand tool, then area and perimeter were measured. Similarly, quantification of the number for paranode-associated axonal dystrophy versus the rest of the paranodes was performed using Fiji ImageJ and the number was manually counted using the 'multi-point' function.

No statistical methods were used to determine sample sizes, but our sample sizes were similar to those generally employed in the field. The experiments were not randomized. Data collection and analysis were not performed blind to the conditions of the experiments; however, we applied high-throughput AI-guided automated image quantification whenever we could. All experiments have been repeated independently in at least three animals or three human samples. No animals or data points were excluded from the analyses, unless specified in the Results and Methods sections. All quantifications of results derived from this study were performed two-sided. Data distribution was assumed to be normal but this was not formally tested. Excel (Microsoft), Prism (GraphPad), Avia (Leica), Qlucore Omics Explorer v.3.6 (Qlucore) and RStudio (v.4.0.2) were used for data analysis and plotting. Statistical methods used are described in the figure legend for each relevant panel.

Reporting summary

Further information on research design is available in the Nature Portfolio Reporting Summary linked to this article.

Data availability

Raw proteomics data are provided in Supplementary Table 1. The mass spectrometry proteomics datasets were deposited to the ProteomeXchange Consortium via the PRIDE partner repository with the dataset identifier PXD045861. For proteomics sample information see Supplementary Table 2. SwissProt database can be accessed here: https://www.uniprot.org/uniprotkb?query=*&facets=reviewed%3Atrue%2Cmodel_organism%3A9606. GeneOntology.org database can be accessed here: https://geneontology.org/. g:profiler database can be accessed here: https://biit.cs.ut.ee/gprofiler/gost. OmniPath, a comprehensive intercellular database, can be accessed here: https://omnipathdb.org/. CellChat database can be accessed here: http://www.cellchat.org/. CellPhoneDB database can be accessed here: https://www.cellphonedb.org/. CollecTRI can be accessed here: https://github.com/saezlab/CollecTRI. Axogliaosome proteins were cited from ref. 105 (PMID: 20830807). The myelin human proteome was cited from ref. 40 (PMID: 35543322). Bulk brain tissue protein expression was cited from ref. 16 (PMID: 35115731) and ref. 17 (PMID: 32284590). Single-cell RNA expression was cited from ref. 11 (PMID: 31042697), ref. 14 (PMID: 31932797) and ref. 12 (PMID: 33432193).

Code availability

Code for STED imaging data analysis is available at https://github.com/bewersdorflab/Yifei-Lukas-Collab. R codes for the analysis of paranode size distribution can be accessed at the following location: https://github.com/ShawnQin/calcium_trace.

References

102. Oakley, H. et al. Intraneuronal β-amyloid aggregates, neurodegeneration, and neuron loss in transgenic mice with five familial Alzheimer's disease mutations: potential factors in amyloid plaque formation. *J. Neurosci.* **26**, 10129–10140 (2006).
103. Feng, G. et al. Imaging neuronal subsets in transgenic mice expressing multiple spectral variants of GFP. *Neuron* **28**, 41–51 (2000).
104. Harris, M. A. et al. The Gene Ontology (GO) database and informatics resource. *Nucleic Acids Res.* **32**, D258–D261 (2004).
105. Dhaunchak, A. S. et al. A proteome map of axoglial specializations isolated and purified from human central nervous system. *Glia* **58**, 1949–1960 (2010).
106. Binder, J. X. et al. COMPARTMENTS: unification and visualization of protein subcellular localization evidence. *Database (Oxford)* **2014**, bau012 (2014).
107. Szklarczyk, D. et al. STRING v11: protein-protein association networks with increased coverage, supporting functional discovery in genome-wide experimental datasets. *Nucleic Acids Res.* **47**, D607–D613 (2019).
108. Merico, D. et al. Enrichment map: a network-based method for gene-set enrichment visualization and interpretation. *PLoS ONE* **5**, e13984 (2010).
109. Raudvere, U. et al. g:Profiler: a web server for functional enrichment analysis and conversions of gene lists (2019 update). *Nucleic Acids Res.* **47**, W191–W198 (2019).
110. Kramer, A. et al. Causal analysis approaches in Ingenuity Pathway Analysis. *Bioinformatics* **30**, 523–530 (2014).
111. Saab, A. S. et al. Oligodendroglial NMDA receptors regulate glucose import and axonal energy metabolism. *Neuron* **91**, 119–132 (2016).
112. Micu, I. et al. The molecular physiology of the axo-myelinic synapse. *Exp. Neurol.* **276**, 41–50 (2016).
113. Yang, A. C. et al. A human brain vascular atlas reveals diverse mediators of Alzheimer's risk. *Nature* **603**, 885–892 (2022).
114. Ashburner, M. et al. Gene ontology: tool for the unification of biology. The Gene Ontology Consortium. *Nat. Genet.* **25**, 25–29 (2000).
115. Gillespie, M. et al. The reactome pathway knowledgebase 2022. *Nucleic Acids Res.* **50**, D687–D692 (2022).
116. Reimand, J. et al. g:Profiler–a web-based toolset for functional profiling of gene lists from large-scale experiments. *Nucleic Acids Res.* **35**, W193–W200 (2007).
117. Reimand, J. et al. Pathway enrichment analysis and visualization of omics data using g:Profiler, GSEA, Cytoscape and EnrichmentMap. *Nat. Protoc.* **14**, 482–517 (2019).
118. Heumos, L. et al. Best practices for single-cell analysis across modalities. *Nat. Rev. Genet.* **24**, 550–572 (2023).
119. Turei, D. et al. Integrated intra- and intercellular signaling knowledge for multicellular omics analysis. *Mol. Syst. Biol.* **17**, e9923 (2021).
120. Butler, A. et al. Integrating single-cell transcriptomic data across different conditions, technologies, and species. *Nat. Biotechnol.* **36**, 411–420 (2018).
121. Yuan, P. et al. TREM2 haplodeficiency in mice and humans impairs the microglia barrier function leading to decreased amyloid compaction and severe axonal dystrophy. *Neuron* **92**, 252–264 (2016).
122. Schroeder, L. K. et al. Dynamic nanoscale morphology of the ER surveyed by STED microscopy. *J. Cell Biol.* **218**, 83–96 (2019).
123. Voas, M. G. et al. αII-spectrin is essential for assembly of the nodes of Ranvier in myelinated axons. *Curr. Biol.* **17**, 562–568 (2007).
124. Zhang, C. et al. Membrane domain organization of myelinated axons requires βII spectrin. *J. Cell Biol.* **203**, 437–443 (2013).
125. Susuki, K. et al. Glial βII spectrin contributes to paranode formation and maintenance. *J. Neurosci.* **38**, 6063–6075 (2018).
126. Colakoglu, G. et al. Contactin-1 regulates myelination and nodal/paranodal domain organization in the central nervous system. *Proc. Natl Acad. Sci. USA* **111**, E394–E403 (2014).
127. Boyle, M. E. et al. Contactin orchestrates assembly of the septate-like junctions at the paranode in myelinated peripheral nerve. *Neuron* **30**, 385–397 (2001).
128. Rasband, M. N. et al. Dependence of nodal sodium channel clustering on paranodal axoglial contact in the developing CNS. *J. Neurosci.* **19**, 7516–7528 (1999).

129. Sherman, D. L. et al. Neurofascins are required to establish axonal domains for saltatory conduction. *Neuron* **48**, 737–742 (2005).
130. Rasband, M. N., Taylor, C. M. & Bansal, R. Paranodal transverse bands are required for maintenance but not initiation of Nav1.6 sodium channel clustering in CNS optic nerve axons. *Glia* **44**, 173–182 (2003).
131. Cousin, M. A. et al. Pathogenic SPTBN1 variants cause an autosomal dominant neurodevelopmental syndrome. *Nat. Genet.* **53**, 1006–1021 (2021).
132. Dolapchieva, S., Eggers, R. & Kuhnel, W. Expression of neural cell adhesion molecule (NCAM) in the peripheral nerve fibers demonstrated by postembedding immunogold method on ultrathin sections. A preliminary study. *Ann. Anat.* **184**, 137–140 (2002).
133. Liu, C. H. et al. Nodal β spectrins are required to maintain Na^+ channel clustering and axon integrity. *eLife* **9**, e52378 (2020).
134. Brunner, C. et al. Differential ultrastructural localization of myelin basic protein, myelin/oligodendroglial glycoprotein, and 2′,3′-cyclic nucleotide 3′-phosphodiesterase in the CNS of adult rats. *J. Neurochem.* **52**, 296–304 (1989).
135. Roth, A. D. et al. Septin 7: actin cross-organization is required for axonal association of Schwann cells. *Biol. Res.* **46**, 243–249 (2013).
136. Pavlou, O. et al. Analysis of interactions of the adhesion molecule TAG-1 and its domains with other immunoglobulin superfamily members. *Mol. Cell. Neurosci.* **20**, 367–381 (2002).
137. Kozar-Gillan, N. et al. LGI3/2-ADAM23 interactions cluster Kv1 channels in myelinated axons to regulate refractory period. *J. Cell Biol.* **222**, e202211031 (2023).
138. Patzig, J. et al. Septin/anillin filaments scaffold central nervous system myelin to accelerate nerve conduction. *eLife* **5**, e17119 (2016).
139. Sukhanov, N. et al. Differential contribution of Cadm1-Cadm3 cell adhesion molecules to peripheral myelinated axons. *J. Neurosci.* **41**, 1393–1400 (2021).
140. Martens, A. K. et al. Targeted inactivation of the Septin2 and Septin9 genes in myelinating Schwann cells of mice. *Cytoskeleton (Hoboken)* **80**, 290–302 (2023).
141. Yoshimura, T. et al. GSK-3β regulates phosphorylation of CRMP-2 and neuronal polarity. *Cell* **120**, 137–149 (2005).
142. Oliver, D. et al. Integrins have cell-type-specific roles in the development of motor neuron connectivity. *J. Dev. Biol.* **7**, 17 (2019).
143. Apostolo, N. et al. Synapse type-specific proteomic dissection identifies IgSF8 as a hippocampal CA3 microcircuit organizer. *Nat. Commun.* **11**, 5171 (2020).
144. Ray, A. & Treloar, H. B. IgSF8: a developmentally and functionally regulated cell adhesion molecule in olfactory sensory neuron axons and synapses. *Mol. Cell. Neurosci.* **50**, 238–249 (2012).
145. Vardar, G. et al. Distinct functions of syntaxin-1 in neuronal maintenance, synaptic vesicle docking, and fusion in mouse neurons. *J. Neurosci.* **36**, 7911–7924 (2016).
146. De Rossi, P. et al. Neuronal BIN1 regulates presynaptic neurotransmitter release and memory consolidation. *Cell Rep.* **30**, 3520–3535 e7 (2020).
147. Barrecheguren, P. J. et al. SNARE proteins play a role in motor axon guidance in vertebrates and invertebrates. *Dev. Neurobiol.* **77**, 963–974 (2017).
148. Parcerisas, A. et al. The hidden side of NCAM family: NCAM2, a key cytoskeleton organization molecule regulating multiple neural functions. *Int. J. Mol. Sci.* **22**, 10021 (2021).
149. King, R. H. et al. Ndrg1 in development and maintenance of the myelin sheath. *Neurobiol. Dis.* **42**, 368–380 (2011).
150. Marechal, D. et al. N-myc downstream regulated family member 1 (NDRG1) is enriched in myelinating oligodendrocytes and impacts myelin degradation in response to demyelination. *Glia* **70**, 321–336 (2022).
151. Higurashi, M. et al. Localized role of CRMP1 and CRMP2 in neurite outgrowth and growth cone steering. *Dev. Neurobiol.* **72**, 1528–1540 (2012).
152. Ishimoto, T. et al. Mice lacking BCAS1, a novel myelin-associated protein, display hypomyelination, schizophrenia-like abnormal behaviors, and upregulation of inflammatory genes in the brain. *Glia* **65**, 727–739 (2017).
153. Meschkat, M. et al. White matter integrity in mice requires continuous myelin synthesis at the inner tongue. *Nat. Commun.* **13**, 1163 (2022).
154. Thomas, R. et al. LGI1 is a Nogo receptor 1 ligand that antagonizes myelin-based growth inhibition. *J. Neurosci.* **30**, 6607–6612 (2010).
155. Balaji, V. et al. Pathological missorting of endogenous MAPT/Tau in neurons caused by failure of protein degradation systems. *Autophagy* **14**, 2139–2154 (2018).
156. Aparicio, G. I. et al. Endogenous glycoprotein GPM6a is involved in neurite outgrowth in rat dorsal root ganglion neurons. *Biomolecules* **13**, 594 (2023).
157. Schneider, F. et al. Mutual functional dependence of cyclase-associated protein 1 (CAP1) and cofilin1 in neuronal actin dynamics and growth cone function. *Prog. Neurobiol.* **202**, 102050 (2021).
158. Thakurela, S. et al. The transcriptome of mouse central nervous system myelin. *Sci. Rep.* **6**, 25828 (2016).

Acknowledgements

This project was supported by National Institutes of Health (NIH) grants no. RF1AG058257, no. R01NS115544 and no. R01NS111961 (J.G.), a Cure Alzheimer's Fund Research Grant (J.G.), a Yale/NIDA Neuroproteomics Center Pilot Project Grant 2019 (Y.C.), a BrightFocus Foundation Postdoctoral Fellowship Program in Alzheimer's Disease Research (grant no. A2021003F) (Y.C.), a Yale ADRC Research Scholar Award (Y.C.), an Alzheimer's Association Research Fellowship (grant no. 23AARF-1020552) (Y.C.), an EMBL Corporate Partnership Programme Fellowship (Y.C.) and Yale ADRC grant no. P30 AG066508 (A.C.N). I.P.-d.-S. and E.P. were supported by EMBL-EBI Core funding. EMBL IT Support is acknowledged for provision of computer and data storage servers. M.S. and J.R. were supported by the Investigator Award to J.R. from Ontario Institute for Cancer Research (OICR), an NSERC Discovery Grant no. RGPIN-2023-04646 to J.R. and a CIHR Catalyst Grant no. DV1-197665 to J.R. Funding to OICR is provided by the Government of Ontario. We thank the Yale/NIDA Neuroproteomics Center (grant no. P30 DA018343) for providing experimental design advice, technical support and funding opportunities. We thank F. Collin from the Keck MS & Proteomics Resource at the Yale School of Medicine for processing the LC–MS/MS experiments. We also thank the Keck MS & Proteomics Resource at the Yale School of Medicine for providing the necessary mass spectrometers and the accompanying biotechnology tools funded in part by the Yale School of Medicine and by the Office of The Director, NIH (grants no. S10OD02365101A1, no. S10OD019967 and no. S10OD018034). The funders had no role in study design, data collection and analysis, decision to publish or preparation of the manuscript. We thank the Yale ADRC (grant no. P30 AG066508) and D. Davis and the University of Miami Brain Endowment Bank, an NIH NeuroBioBank, for providing human postmortem AD and control brain tissues. We thank S. Qin (Flatiron Institute) for performing the quantile–quantile plot data analysis. We thank the staff at the Center for Cellular and Molecular Imaging, Electron Microscopy Facility at Yale Medical School for assistance with the electron microscopy experiments. We thank M. Rasband (Baylor College of Medicine) and R. Hill (Dartmouth College) for critical comments and suggestions on this project. Schematic figures were created with BioRender.com (Figs. 1a,p, 2a, 3a,b,d,g,h, 4e, 5a,e–g, 6a, 7a,i and 8a,m).

Author contributions

Y.C. and J.G. conceived and designed the study. Y.C. performed proximity labeling proteomics and western blotting and proteomics

data analysis. J.K. and T.T.L. performed LC–MS/MS and data analysis. A.C.N. supervised the proteomics experiments and analysis. M.S., Y.C. and J.R. performed the integrative pathway enrichment analysis. I.P.-d.-S., Y.C. and E.P. performed the cell–cell communication analysis. A.H. performed pathological evaluation of human brain specimens and provided the tissues. Y.C., P.T., A.B. and T.H. performed immunofluorescence and confocal imaging. P.T., T.H. and P.Y. performed myelin analysis. F.C., Y.C., T.H. and L.T. performed expansion microscopy and imaging. L.A.F., Y.C. and T.H. performed STED imaging, image analysis and quantification. T.H., P.T., A.B. and R.W. performed quantifications. Y.C. performed electron microscopy sample preparation. Y.C., T.H., P.T., A.B. and R.W. performed statistical analysis. Y.C. and J.G. prepared the manuscript. J.G. supervised the study.

Competing interests

The authors declare no competing interests.

Additional information

Extended data is available for this paper at https://doi.org/10.1038/s41593-025-01973-8.

Supplementary information The online version contains supplementary material available at https://doi.org/10.1038/s41593-025-01973-8.

Correspondence and requests for materials should be addressed to Yifei Cai or Jaime Grutzendler.

Peer review information *Nature Neuroscience* thanks Junmin Peng and the other, anonymous, reviewer(s) for their contribution to the peer review of this work.

https://doi.org/10.1038/s41593-025-01973-8

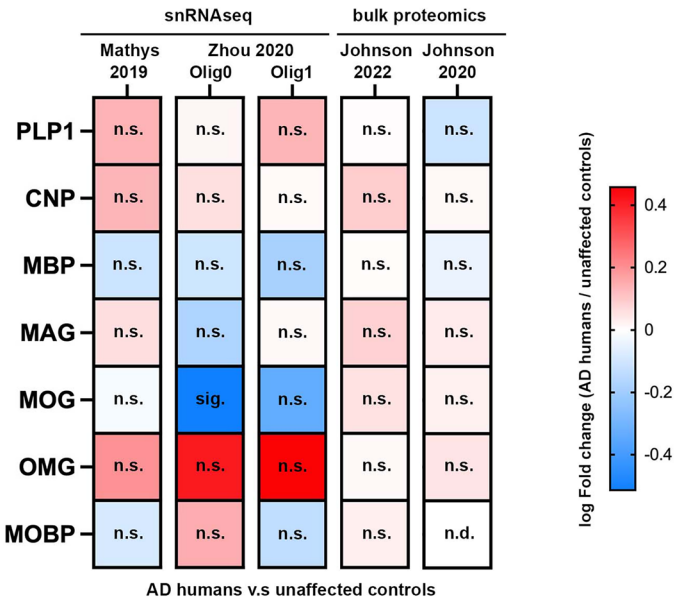

Extended Data Fig. 1 | Expression of myelin marker proteins in AD versus controls from snRNAseq and bulk proteomics studies. Fold changes in myelin marker protein expression in human AD frontal cortex (including prefrontal cortex and frontal gyrus) were extracted from recent snRNA-seq and bulk proteomics datasets[11,14,16,17]. RNA and protein expression levels in oligodendrocyte clusters are shown in the three left columns and two right columns, respectively. Abbreviation: n.s. = not significant, sig. = significant.

https://doi.org/10.1038/s41593-025-01973-8

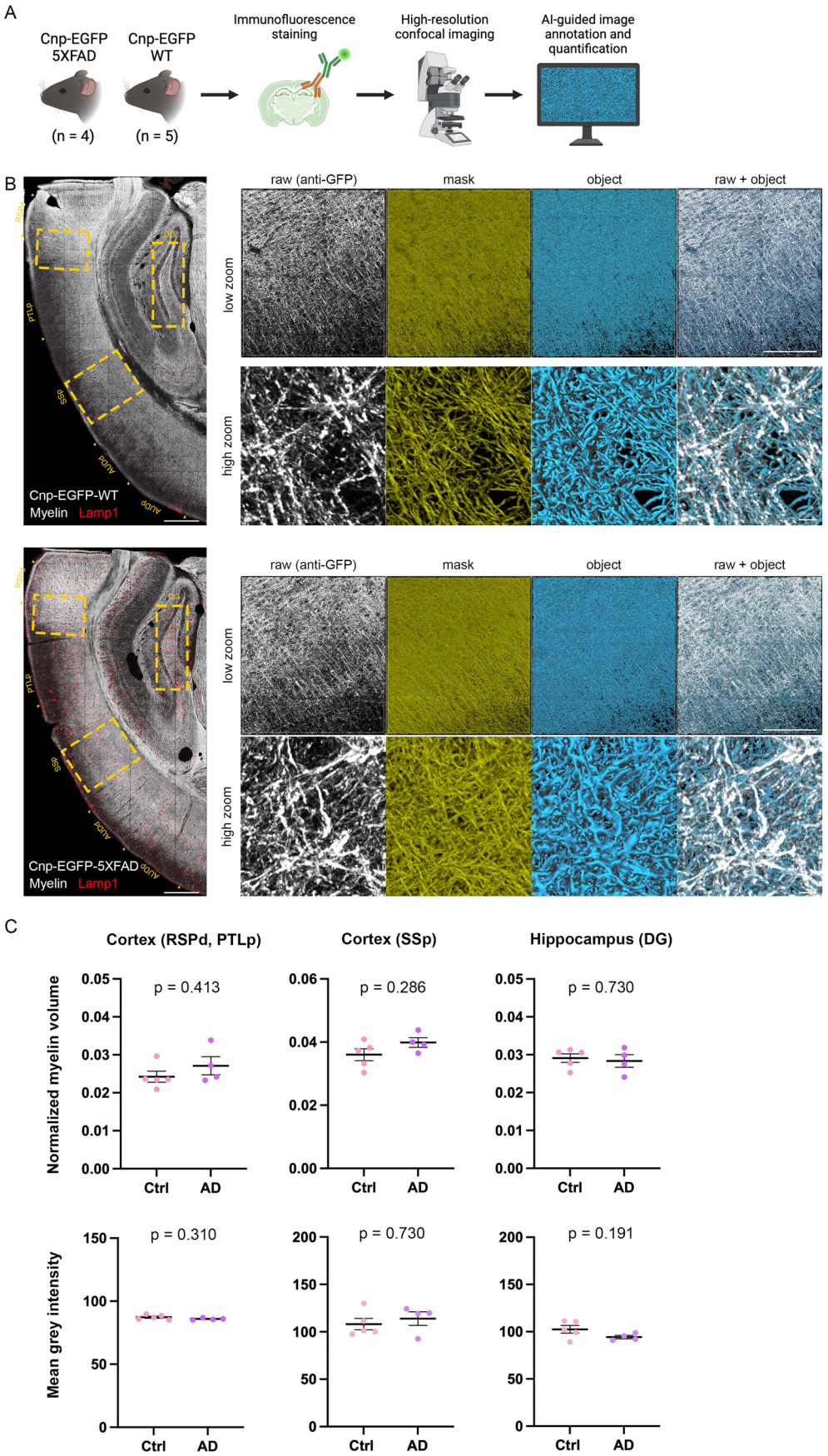

Extended Data Fig. 2 | See next page for caption.

https://doi.org/10.1038/s41593-025-01973-8

Extended Data Fig. 2 | AI-guided myelin quantification in Cnp-EGFP-5XFAD and Cnp-EGFP-WT mice. a. Myelin in Cnp-EGFP-5XFAD mice and Cnp-EGFP-WT mice was quantified using AI-guided segmentation of immunofluorescence confocal images. **b**. Representative images showing tiled confocal images of brains from Cnp-EGFP-WT and Cnp-EGFP-5XFAD mice. Myelin (grey) was labeled by anti-GFP, and lysosomes/dystrophic neurites (red) were labeled by anti-Lamp1. Brain regions used for quantification are marked by yellow boxes. Low zoom and high zoom representative images with myelin (anti-GFP), AI-generated masks and objects. Scale bars: full-tiled images = 500 µm; low zoom myelin images = 100 µm; high zoom images = 5 µm. **c**. Quantification of myelin volume and mean fluorescence intensity in regions of interest for Cnp-EGFP-5XFAD mice (n = 4) and Cnp-EGFP-WT mice (n = 5); (Mann Whitney test, two-tailed). Abbreviations: RSPd = Retrosplenial area, dorsal part; PTLp = Posterior parietal association areas; DG = dentate gyrus. Error bars indicate SEM.

https://doi.org/10.1038/s41593-025-01973-8

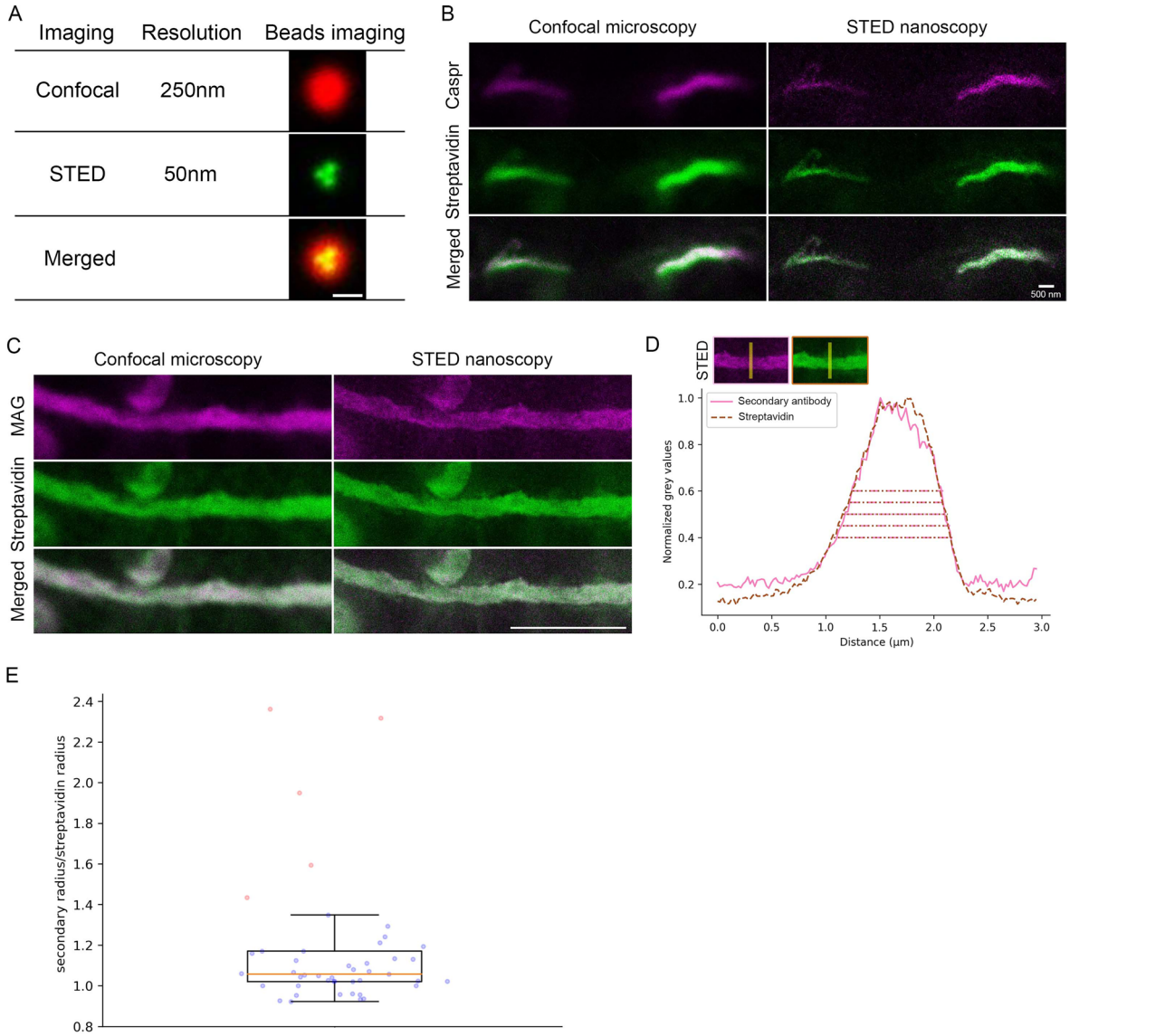

Extended Data Fig. 3 | Super-resolution STED microscopy demonstrates spatial precision of proximity labeling. a. Bead imaging illustrates the resolution difference between confocal microscopy (250 nm) and STED microscopy (50 nm). Scale bar = 250 nm. **b-c**. Representative confocal and STED images of proximity labeling in human postmortem brains showing (**B**) paranodes (anti-CASPR, magenta) and (**C**) internodes (anti-MAG, magenta), with biotinylated proteins detected by streptavidin (green); scale bars: (**B**) 500 nm, (**C**) 5 µm. **d**. A representative line plot shows the radius measurements of signals from the secondary antibody channel (magenta) and the streptavidin channel (green). **e**. A dot plot showing the radius ratio between the secondary antibody (magenta) and streptavidin (green). The average radius ratio is 1.07 (SD= 0.1); the orange line indicates the median, with the lower and upper edges representing the 25th (Q1) and 75th (Q3) percentiles. Whiskers extend to the minimum and maximum values within 1.5 times the interquartile range, and outliers (pink circles) are plotted individually (and excluded from analysis). Each dot represents a myelin segment (n = 45).

https://doi.org/10.1038/s41593-025-01973-8

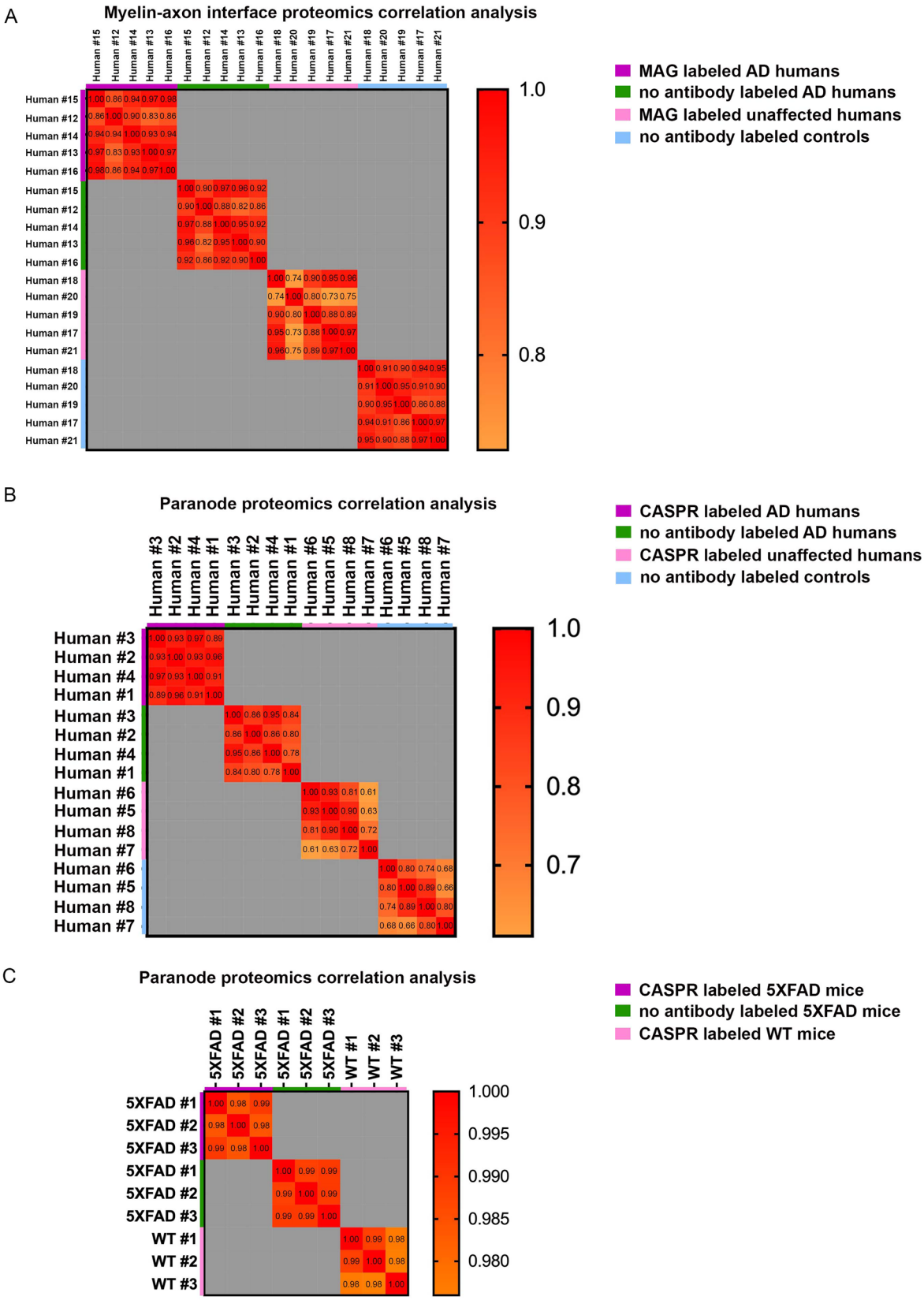

Extended Data Fig. 4 | Correlation analysis of proteomics samples in humans and mice. Correlation analysis for biological replicates of (**a**) MAG-labeled and (**b**) CASPR-labeled samples, along with the no-antibody labeled proteomic controls in (**A**-**B**) human brains and (**C**) in mice. Pearson correlation coefficient (R^2) values are provided in each comparison box.

https://doi.org/10.1038/s41593-025-01973-8

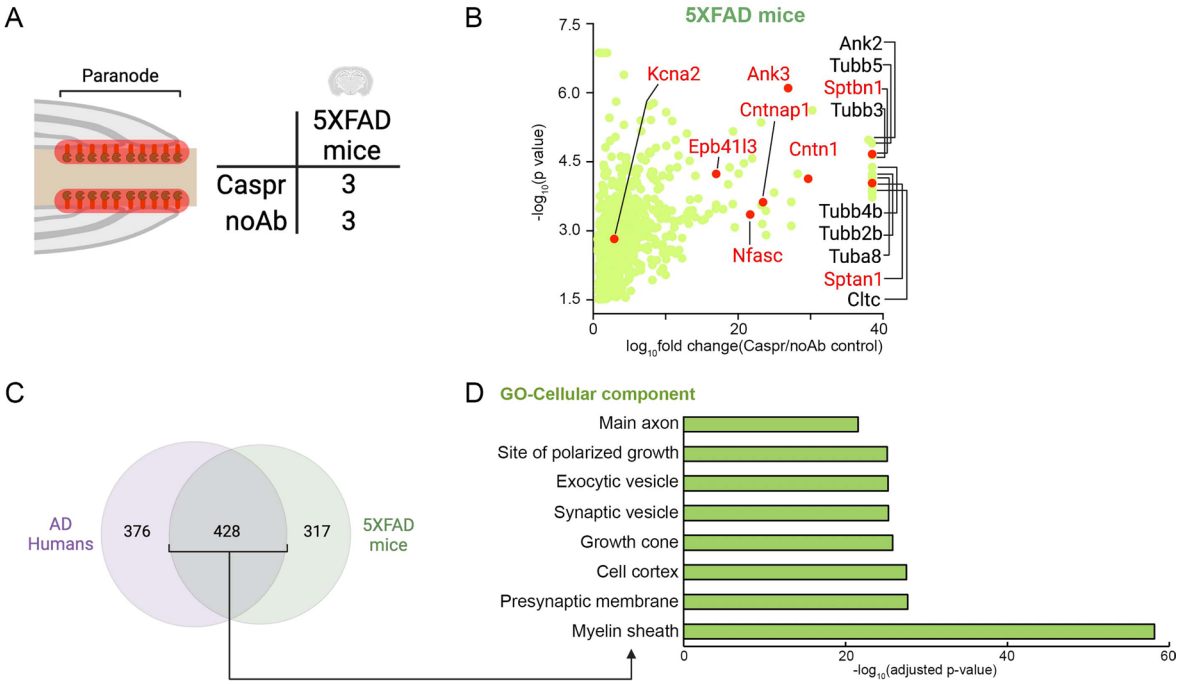

Extended Data Fig. 5 | Caspr-labeled paranode-enriched proteomes in 5XFAD mice. A. Schematic illustrating the experimental design. **B.** Partial volcano plot of proteomic hits in paranode-enriched samples from 5XFAD mice. Known paranode-related hits are shown in red and other hits in green. The gene names of the top 10 proteomic hits and known paranodal proteins are indicated. **C.** Venn diagram showing the number of paranode-enriched proteomic hits shared between AD humans and 5XFAD mice. **D.** Gene Ontology cellular component (GO-CC) analysis of the shared hits between AD humans and mice, displaying the top 8 GO-CC terms. Quantifications in panels B and D were performed two-sided.

https://doi.org/10.1038/s41593-025-01973-8

A

Top 100 paranodal enriched proteins in unaffected human brains

1	CLTC		MYH9		RYR2		SCN2A*		STIP1
	SPTAN1*		VCAN#		TLN2		USP9X		KIF21A
	SPTBN1*		ATP2B1		CADPS		ACLY		SYNJ1
	CNTN1*		FASN#		PDCD6IP		ADD1		GDI2
	CNTNAP1*		NCAM1#		ROCK2		EEF2		GNB4
	MAP1A		DMXL2		ALDOA		SPTB#		TLN1
	ANK3*		ANXA6		PACSIN1		KIF5C		PREP
	SPTBN2		CYFIP2		GDI1		AAK1		PGD
	NFASC*		HSP90AB1		DPYSL3		SLC8A2		AP2M1
10	TNR#	30	TNC	50	HK1	70	ATP6V0A1	90	ATP6V1H
	MACF1		GNAO1		ATP2A2		IPO5		NAPB
	DST		ATP2B3		SBF1		PTPRZ1		AHCYL1
	STXBP1		NCKAP1		C3		SIRPA		HAPLN2#
	POTEE		CNTNAP2#		EEA1		KIF1A		SLC4A4
	ACTN1		PLCB1		DCTN1		WDR7		HUWE1
	ACTN4#		DNM2		NCDN		CCT2		NCAN#
	MYO5A		CAND1		DNM1L		PLXNA1		EPB41L2#
	ATP2B4		ACTN2		UBR4		CNTN2#		SLC12A5
	SPTBN4#		AARS1		PLXNA4		GNAI3		RAP1GDS1
20	ATP2B2	40	L1CAM	60	IGSF8	80	ATP8A1	100	CKAP5

B

Top 100 myelin-axon interface proteins in unaffected human brains

1	CNP*		GSN		CNTN2*		LDHA		FSCN1
	DPYSL2#		GDI2		GNAI1		NCAN*		NPEPPS
	CNTN1*		VCAN*		ATP1B1		PTPRZ1		KCNAB2#
	ATP1A3		VCP		PLP1*		RDX#		SLC44A1
	ATP1A1		HAPLN2		NDRG1#		BCAS1#		CNDP2
	CNTNAP1*		QDPR		MDH1		PRDX4		VAT1
	NFASC*		DPYSL3		GNAI2		CADM4*		CD81
	ATP1A2		IGSF8#		MVP		A2M		PRDX6
	GAPDH		BCAN*		CNTNAP2*		PIP4K2A		LGI1#
10	TNR*	30	SIRT2	50	VSNL1	70	CCT3	90	MAPT#
	INA#		STX1B#		PRDX1		NCAM2#		SEPTIN2*
	ANXA6		MAG*		CCT7		RAP1A		GNAS
	NCAM1*		SEPTIN7*		CBR1		MSN		ANXA11
	GNAO1		TKT		CRMP1#		ATP6V1C1		GPM6A#
	ENO1		FTH1		CA2		CFL2		PGM1
	PKM		BIN1#		HSPA4		ANXA7		CAP1
	ALDOA		GNB1		LGI3*		PLS3		SEPTIN4*
	HSPA8		LDHB		SEPTIN8*		GNAQ		PLEKHB1#
	GDI1		NRCAM*		CCT2		ADAM22*		CLIC4
20	MOG*	40	SNAP25#	60	UBB	80	CFL1	100	PFKM

Extended Data Fig. 6 | Top 100 hits in the CASPR-labeled paranode-enriched proteome and MAG-labeled myelin-axon interface proteome in unaffected human brains. (**a**) The top 100 proteomic hits identified in the paranode-enriched proteome. Proteins known to be expressed in the paranode are marked with an asterisk ('*'): SPTAN1[123], SPTBN1[124,125], CNTN1[126,127], CNTNAP1[35], ANK3[21,128], NFASC[129], and SCN2A[130]. Proteins known to be expressed in the node of Ranvier and juxtaparanode are marked with a hash ('#'): TNR[1], ACTN4[131], SPTBN4[1], VCAN[1], NCAM1[132], CNTNAP2[129], SPTB[133], CNTN2[1], HAPLN2[1], NCAN[1], EPB41L2[1]. (**b**) The top 100 proteomic hits identified in the myelin-axon-interface proteome. Proteins known to be expressed at the myelin-axon interface are marked with an asterisk ('*'): CNP[134], CNTN1[126,127], CNTNAP1[35], NFASC[129], NCAM1[132], MOG[134], MAG[36–38], SEPTIN7[135], NRCAM[136], CNTN2[36–38], PLP1[20], CNTNAP2[1], LGI3[137], SEPTIN8[138], CADM4[20,139], ADAM22[137], SEPTIN2[138,140], SEPTIN4[138]. Proteins known to be related to myelin or axon are marked with a hash ('#'): DPYSL2[141], INA1[142], IGSF8[143,144], STX1B[145], BIN1[146], SNAP25[147], NCAM2[148], NDRG1[149,150], CRMP1[151], BCAS1[152], KCNAB2[153], LGI1[154], MAPT[155], GPM6A[156], CAP1[157], PLEKHB1[158].

https://doi.org/10.1038/s41593-025-01973-8

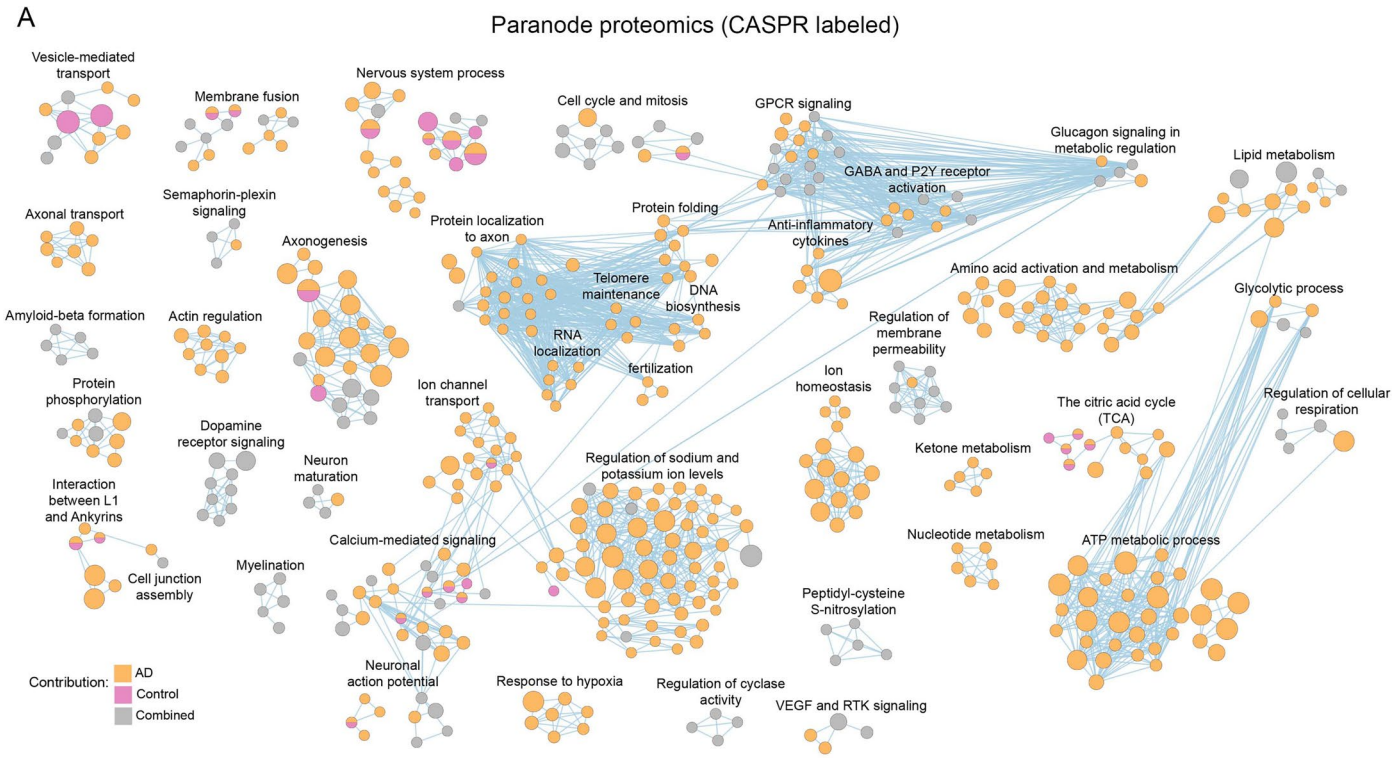

Extended Data Fig. 7 | Integrative pathway enrichment analysis of paranode and myelin-axon interface proteomes using the ActivePathways method. (**a-b**) The Enrichment Map depicts a network of pathways (FDR < 0.05) where edges connect pathways sharing many genes. Node size reflects the number of genes in each pathway, and node color indicates the dataset contribution (combined AD and control). Theme labels were curated based on the main pathways represented in each subnetwork. Only subnetworks with at least four pathways connected by edges are shown. Grey nodes indicate combined evidence of pathway enrichment in which the respective pathways were detected in the integrative analysis but not detected in either the AD or Control proteomes alone.

https://doi.org/10.1038/s41593-025-01973-8

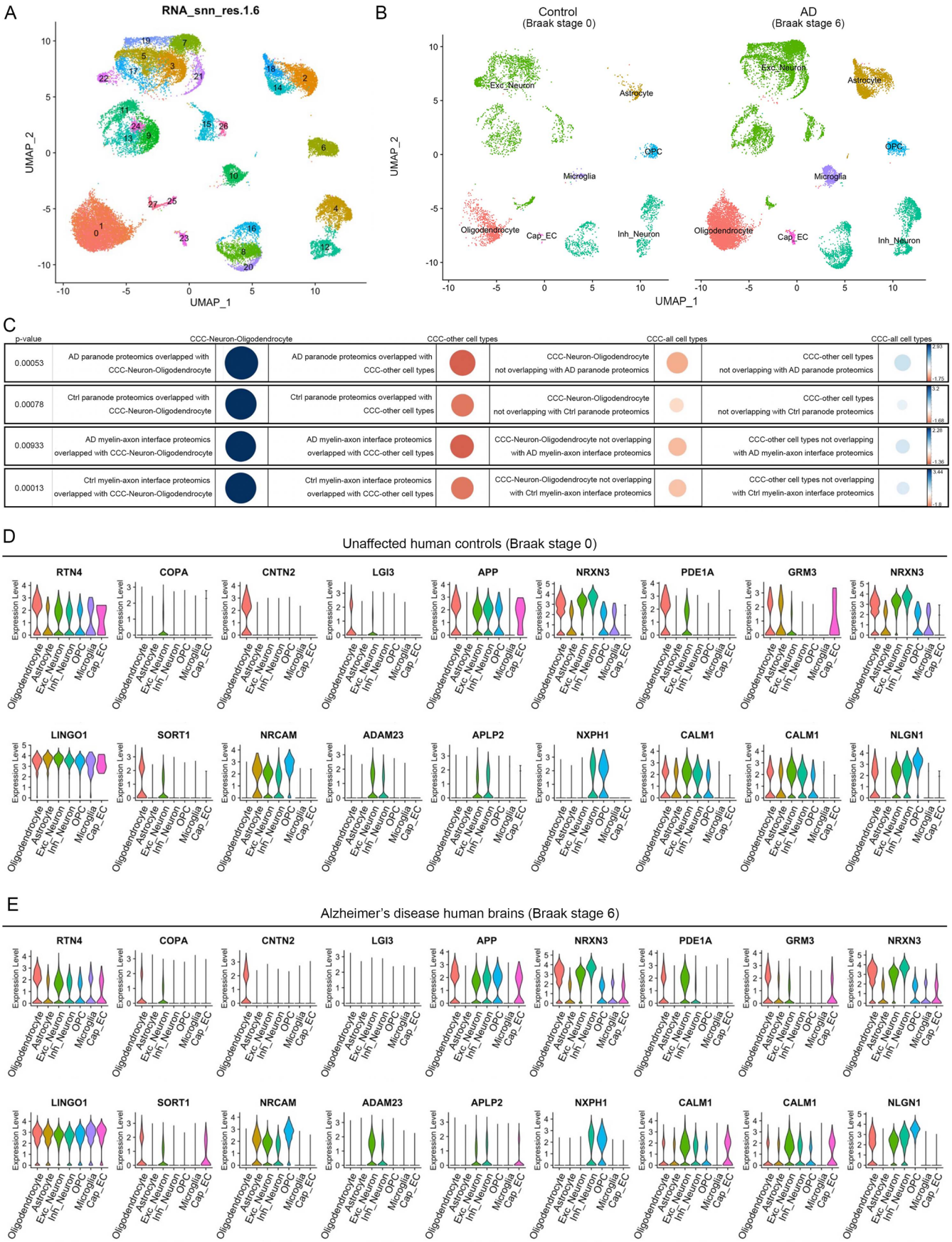

Extended Data Fig. 8 | See next page for caption.

https://doi.org/10.1038/s41593-025-01973-8

Extended Data Fig. 8 | Cell-cell communication analysis revealing ligand-receptor interaction at the myelin-axon interface. a-b. (**A**) Cell clustering and (**B**) cell type annotation of snRNAseq data from AD human frontal cortex (Braak stage 6) and controls (Braak stage 0). **c.** Enrichment analysis shows that myelin-axon interface proteomics (MAG or CASPR-labeled) are highly enriched in neurons and oligodendrocytes, but not in other cell types (related to Fig. 5b). Each row depicts contingency tables for each hypergeometric test (from top to bottom: p-values: 0.0005275, 0.0007784, 0.009328, 0.0001295). In these rows, values with two decimal places indicate residuals and the size of the circles; positive residuals denote that the observed values were more frequent than expected, while negative residuals indicate lower-than-expected frequencies. Quantifications were performed two-sided. **d-e.** Violin plots showing RNA expression levesl of ligand-receptor pairs in (**D**) control human postmortem brains (Braak stage 0) and (**E**) AD human postmortem brains (Braak stage 6).

https://doi.org/10.1038/s41593-025-01973-8

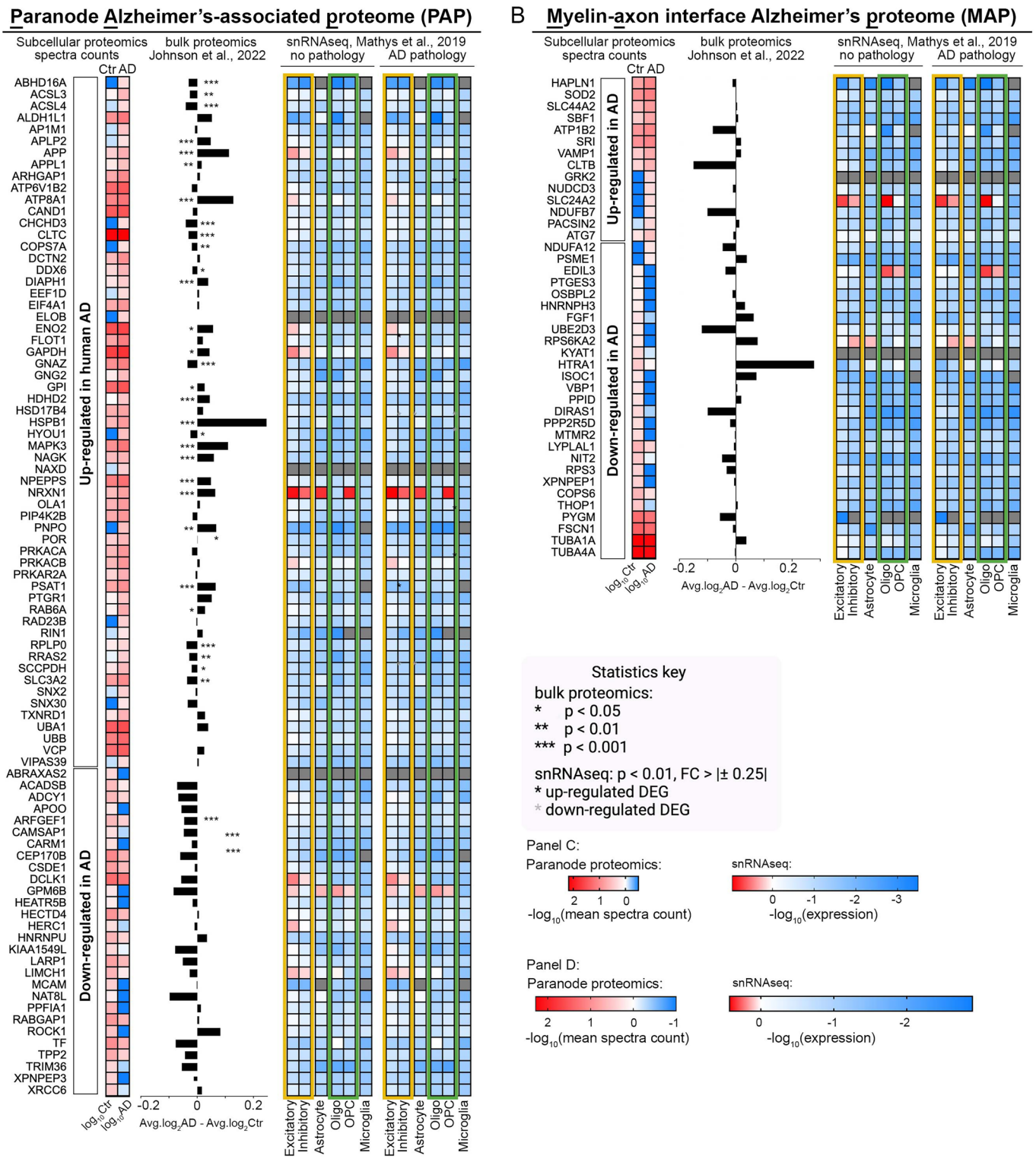

Extended Data Fig. 9 | Paranode-enriched and myelin-axon interface Alzheimer's disease proteomes reveal unique subcellular changes not observed by bulk proteomics or single cell RNA transcriptomics. Heatmaps display (**a**) Paranode Alzheimer's-associated proteomes (PAPs) and (**b**) Myelin-axon interface Alzheimer's proteomes (MAPs). Heatmap denotes $\log_{10}$ (spectral counts). Comparison between PAPs or MAPs and bulk proteomics data (middle panel, Johnson et al.[16]), or single nuclei RNA sequencing transcriptomics (right panels, Mathys et al.[11]) were performed. Both bulk proteomics and snRNAseq data were obtained from their original studies. Neuronal cell types (yellow box) and oligodendrocyte/OPC (green box) were highlighted in the snRNAseq data. Abbreviations: FC = fold change; DEG = differentially expressed genes. (**A** and **B**) Quantifications of subcellular proteomic data derived from this study were performed two-sided.

https://doi.org/10.1038/s41593-025-01973-8

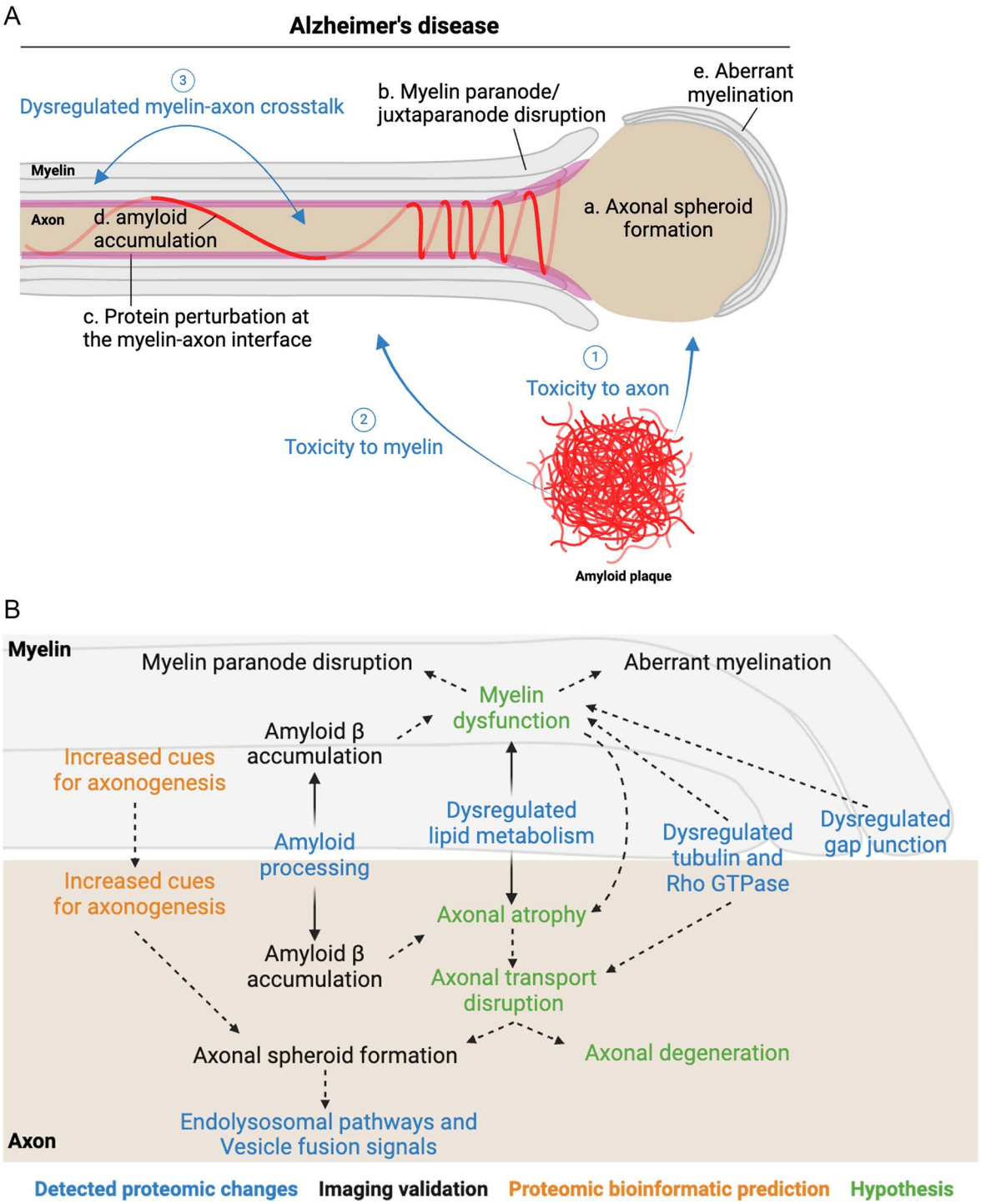

Extended Data Fig. 10 | Diagram of myelin-axon disruption in AD. a. Diagram illustrating how amyloid toxicity to axons and myelin (#1 and #2) may lead to axonal spheroid formation (a), myelin paranode/juxtaparanode disruption (b), protein perturbation at the myelin-axon interface (c) and amyloid accumulation at the interface (d). Together, these events may create a vicious cycle of dysregulated myelin-axon crosstalk and degeneration (#3). **b.** Diagram outlining potential signaling pathways that contribute to myelin-axon disruption, based on findings from myelin-axon interface proteomics and imaging validations.

nature portfolio

Corresponding author(s): Yifei Cai, Jaime Grutzendler

Last updated by author(s): 03/12/2025

Reporting Summary

Nature Portfolio wishes to improve the reproducibility of the work that we publish. This form provides structure for consistency and transparency in reporting. For further information on Nature Portfolio policies, see our Editorial Policies and the Editorial Policy Checklist.

Statistics

For all statistical analyses, confirm that the following items are present in the figure legend, table legend, main text, or Methods section.

n/a	Confirmed	
☐	☒	The exact sample size (*n*) for each experimental group/condition, given as a discrete number and unit of measurement
☐	☒	A statement on whether measurements were taken from distinct samples or whether the same sample was measured repeatedly
☐	☒	The statistical test(s) used AND whether they are one- or two-sided *Only common tests should be described solely by name; describe more complex techniques in the Methods section.*
☐	☒	A description of all covariates tested
☐	☒	A description of any assumptions or corrections, such as tests of normality and adjustment for multiple comparisons
☐	☒	A full description of the statistical parameters including central tendency (e.g. means) or other basic estimates (e.g. regression coefficient) AND variation (e.g. standard deviation) or associated estimates of uncertainty (e.g. confidence intervals)
☐	☒	For null hypothesis testing, the test statistic (e.g. *F*, *t*, *r*) with confidence intervals, effect sizes, degrees of freedom and *P* value noted *Give P values as exact values whenever suitable.*
☒	☐	For Bayesian analysis, information on the choice of priors and Markov chain Monte Carlo settings
☒	☐	For hierarchical and complex designs, identification of the appropriate level for tests and full reporting of outcomes
☐	☒	Estimates of effect sizes (e.g. Cohen's *d*, Pearson's *r*), indicating how they were calculated

Our web collection on statistics for biologists contains articles on many of the points above.

Software and code

Policy information about availability of computer code

Data collection	All imaging data were collected using default software on the Leica confocal SP8 microscopy (Leica). All the LC-MS-MS data were collected using default software on a Thermo Scientific Q Exactive Plus system (Thermo Scientific).
Data analysis	Excel (v16.77.1, Microsoft), Prism (GraphPad v10), Avia (Leica, v11.0.1), Qlucore Omics Explorer v3.6 (Qlucore AB, Lund, Sweden), Proteome Discoverer software v2.2 (Thermo Scientific), Mascot algorithm (version 2.6.1) (Matrix Science), Scaffold v5.1.2 (Proteome Software Inc., Portland, OR) and RStudio (4.0.2) were used for data analysis and plotting. The enrichment map was visualized in Cytoscape (v3.9.1). Pathway analysis was performed using Ingenuity Pathway Analysis (IPA) software (QIAGEN, 2022 release version). Code for STED imaging data analysis is available at https://github.com/bewersdorflab/Yifei-Lukas-Collab.

For manuscripts utilizing custom algorithms or software that are central to the research but not yet described in published literature, software must be made available to editors and reviewers. We strongly encourage code deposition in a community repository (e.g. GitHub). See the Nature Portfolio guidelines for submitting code & software for further information.

Data

Policy information about availability of data

All manuscripts must include a data availability statement. This statement should provide the following information, where applicable:

- Accession codes, unique identifiers, or web links for publicly available datasets
- A description of any restrictions on data availability
- For clinical datasets or third party data, please ensure that the statement adheres to our policy

Raw proteomics data is provided in Table S1. The mass spectrometry proteomics datasets were deposited to the ProteomeXchange Consortium via the PRIDE partner repository with the dataset identifier PXD045861. Proteomics sample information see Table S2.

SwissProt database can be accessed here:https://www.uniprot.org/uniprotkb?query=*&facets=reviewed%3Atrue%2Cmodel_organism%3A9606.
GeneOntology.org database can be accessed here: https://geneontology.org/.
g:profiler database can be accessed here: https://biit.cs.ut.ee/gprofiler/gost
OmniPath, a comprehensive intercellular database, can be accessed here: https://omnipathdb.org/,
CellChat database can be accessed here: http://www.cellchat.org/.
CellphoneDB database can be accessed here: https://www.cellphonedb.org/.
CollecTRI can be accessed from here: https://github.com/saezlab/CollecTRI.

Axogliaosome proteins that were cited from this paper: Dhauchak et al., Glia, 2010 (PMID: 20830807).
Myelin human proteome was cited from this paper: Gargareta et al., Elife, 2022 (PMID: 35543322).
Bulk brain tissue protein expression was cited from these papers: Johnson et al., Nat Neurosci, 2022 (PMID: 35115731) and Johnson et al., Nat Med, 2020 (PMID: 32284590).
Single-cell RNA expression were cited from these papers: Mayths et al., Nature, 2019 (PMID: 31042697), Zhou et al., Nat Med, 2020 (PMID: 31932797) and Leng et al., Nat Neurosci, 2021 (PMID: 33432193).

Research involving human participants, their data, or biological material

Policy information about studies with human participants or human data. See also policy information about sex, gender (identity/presentation), and sexual orientation and race, ethnicity and racism.

Reporting on sex and gender	The use of postmortem samples is considered 'non-human subject' research. Fixed and snap-frozen postmortem human frontal cortices from AD patients and age-matched controls were obtained from the Yale Alzheimer's Disease Research Center, the Banner Institute and the NIH NeuroBioBank. Detailed demographic and clinical information can be found in Supplentary Figure S1. Four AD cases and four age-matched unaffected controls were analyzed by proximity labeling proteomics. For immunofluorescence experiments, six to ten biological replicates of human AD and control specimens were used.
Reporting on race, ethnicity, or other socially relevant groupings	The use of postmortem samples is considered 'non-human subject' research. Fixed and snap-frozen postmortem human frontal cortices from AD patients and age-matched controls were obtained from the Yale Alzheimer's Disease Research Center, the Banner Institute and the NIH NeuroBioBank. Detailed demographic and clinical information can be found in Supplentary Figure S1. Four AD cases and four age-matched unaffected controls were analyzed by proximity labeling proteomics. For immunofluorescence experiments, six to ten biological replicates of human AD and control specimens were used.
Population characteristics	The use of postmortem samples is considered 'non-human subject' research. Fixed and snap-frozen postmortem human frontal cortices from AD patients and age-matched controls were obtained from the Yale Alzheimer's Disease Research Center, the Banner Institute and the NIH NeuroBioBank. Detailed demographic and clinical information can be found in Supplentary Figure S1. Four AD cases and four age-matched unaffected controls were analyzed by proximity labeling proteomics. For immunofluorescence experiments, six to ten biological replicates of human AD and control specimens were used.
Recruitment	No donors were recruited by this study.
Ethics oversight	The use of postmortem samples is considered 'non-human subject' research.

Note that full information on the approval of the study protocol must also be provided in the manuscript.

Field-specific reporting

Please select the one below that is the best fit for your research. If you are not sure, read the appropriate sections before making your selection.

☒ Life sciences ☐ Behavioural & social sciences ☐ Ecological, evolutionary & environmental sciences

For a reference copy of the document with all sections, see nature.com/documents/nr-reporting-summary-flat.pdf

Life sciences study design

All studies must disclose on these points even when the disclosure is negative.

Sample size	No statistical power analysis was used to determine sample sizes, but our sample sizes were similar to those generally employed in the field. Three to six biological replicates were used for animal experiments, and three to ten biological replicates were used for human postmortem brain tissue studies (Yuan et al., Nature, 2022; Yuan et al., Neuron 2016).
Data exclusions	No data were excluded from analysis, except stated in the proteomics sample data analysis method section, as below: To obtain paranodal proteomes or myelin-axon interface proteomes, we first performed Pearson Correlation Analysis across samples using GraphPad Prism 9.5.0. Pearson Correlation Coefficient values were used to evaluate correlations. R2 greater than 0.7 was set as the cutoff. We found that all the human AD, unaffected control and mice samples passed the 0.7 cutoff, except an unaffected control human specimens (Human #7) from the paranode dataset (see Result and Method sections). Therefore, we removed the sample Human #7 from the downstream paranode proteomic analysis. In the myelin-axon interface samples, we observed an unaffected control human specimens (Human #20) that showed a much lower correlation to other samples (R2 between 0.73 ~ 0.80), whereas correlation among all other samples were much higher (R2 between 0.83 ~ 0.98) (see Result and Method sections). To maximize the number of known true hits in the myelin-axon interface samples, the human unaffected control sample Human #20 was excluded from the downstream analysis.
Replication	For proximity labeling proteomics, 9 AD human cases with intermediate to high AD level and 9 age-matched unaffected controls were used. For mice proximity labeling proteomics, 3 5XFAD mice and 3 age-matched wildtype mice were used. For immunofluorescence proteomic validations, 5 severe AD human cases and 5 unaffected control cases were used. 3 5XFAD mice and 3 age-matched wildtype mice were used. For expansion microscopy, 3 AD mice and 3 control mice, 3 AD mice and 3 control human postmortem brains were used. For electron microscopy, 3 AD mice and 3 AD human postmortem brains were used. No biological replicates were excluded, except an unaffected control human sample (Hct16HDMA001) from the paranode proteomics dataset, which did not pass the correlation cutoff 0.7, therefore be excluded for downstream data analysis, as described in the "Proteomic data analysis" method section.
Randomization	For proximity labeling proteomics, 9 AD cases with intermediate to high AD level and 9 age-matched unaffected controls were used. To reduce inter-sample variability and maximize signal-to-noise by avoiding brains with low-density amyloid deposition, we carefully inspected ~ 40 individual postmortem brains using microscopy and selected for proteomic analysis 9 AD brains with the highest density of amyloid plaques and axonal spheroids within the frontal cortex.
Blinding	Although sample preparation and processing were not performed blindly due to the different condition of treatments, all samples and data were processed in a high-throughput or automated fashion. For the non-automated steps of sample and data processing, all samples and data were processed in a consistent manner.

Reporting for specific materials, systems and methods

We require information from authors about some types of materials, experimental systems and methods used in many studies. Here, indicate whether each material, system or method listed is relevant to your study. If you are not sure if a list item applies to your research, read the appropriate section before selecting a response.

Materials & experimental systems

n/a	Involved in the study
☐	☒ Antibodies
☒	☐ Eukaryotic cell lines
☒	☐ Palaeontology and archaeology
☐	☒ Animals and other organisms
☒	☐ Clinical data
☒	☐ Dual use research of concern
☒	☐ Plants

Methods

n/a	Involved in the study
☒	☐ ChIP-seq
☒	☐ Flow cytometry
☒	☐ MRI-based neuroimaging

Antibodies

Antibodies used	Anti-Lamp1 antibody (1:200, DSHB, 1D4B, RRID:AB_2134500) was used to label axonal spheroids in mice. Anti-PLD3 antibody (1:250, Atlas Antibodies, HPA012800, RRID: AB_1855330) was used to label axonal spheroids in humans. SMI312 antibody (1:500, BioLegend, RRID:AB_2566782) or NFH (1:1000, EnCor #CPCA-NF-H, RRID: AB_2149761) were used to label neurofilament in both humans and mice. CASPR antibody (1:600, abcam, ab34151, RRID:AB_869934) was used to label paranodes in both humans and mice. Myelin PLP (1:1000, Biorad MCA839G, RRID:AB_2237198), PLP (1:200, abcam, ab254363, RRID:AB_3095302) and CNPase (1:1000, BioLegend #836404, RRID:AB_2728547), MBP (1:200, Millipore AB9348, RRID: AB_11213157) antibodies were used to label myelin in mice and humans. 4G8 antibody (1:200, BioLegend, 800701, RRID:AB_2564633) and 6e10 antibody (1:200, BioLegend 803001, RRID: AB_2564653) were used to label amyloid plaques and amyloid fibers. Anti-GFP antibody (1:500, Aves Labs, RRID:AB_10000240) was used to label Thy1-YFP neurons or CNP-EGFP myelin in mice. BCAS1 antibody (1:1000, Synaptic System 445 003, RRID: AB_2864793) was used to labeled newly formed myelinating oligodendrocyte. Kv 7.3 antibody (1:200, Synaptic Systems 368 003, RRID: AB_2620129) was used to labeled juxtaparanode. ATP8A1 (1:200, Atlas Antibodies, HPA052935, RRID: AB_2681992), ATP2B3 (1:200,

Atlas Antibodies, HPA001583, RRID: AB_1079641) , L1CAM (1:200, Millipore, MAB5272, RRID: AB_2133200) , TF (1:200, Proteintech 17435-1-AP, RRID: AB_2035023) , NRXN3 (1:200, Atlas Antibodies, HPA002727, RRID: AB_1079468), ALCAM (1:200, Novus AF1172, RRID: AB_354644) , LSAMP (1:200, Atlas Antibodies, HPA076122, RRID: AB_2686779), HAPLN1 (1:200, Atlas Antibodies, HPA019105, RRID: AB_1850496) , NUDCD3 (1:200, Atlas Antibodies, HPA019136, RRID: AB_1852370), HYOU1 (1:200, Invitrogen PA5-27655, RRID: AB_2545131), ACSL4 (1:200, Invitrogen PA5-27137, RRID: AB_2544613), GRK2 (1:200, Invitrogen MA5-15840, RRID: AB_11152830) antibodies were used to label top proteomic hits in humans postmortem brains. Alexa dye conjugated secondary antibodies were used (1:600, ThermoFisher Scientific, A32790, A-31572, A-31573, A32773, A-31570, A-31571, A-21447).

Validation

All antibodies were commercially available and have been tested by the manufacturers with immunofluoresence or western blot applications, and also have been cited by other publications (references are available on the manufacturers websites). We further validated all the antibodies for immunofluoresence or western blot applications in human brains or mice brains, depending on the purposes of each experiment.

Animals and other research organisms

Policy information about studies involving animals; ARRIVE guidelines recommended for reporting animal research, and Sex and Gender in Research

Laboratory animals	All animal procedures were approved by the Institutional Animal Care and Use Committee at Yale University ((IACUC protocol 2023-11438).). WT (C57BL/6J) (12-15 months old), 5XFAD (Tg6799) mice (12-15 months old), Thy1-YFP mice (JAX #003709) (6-12 months old), and CNP-EGPF mice (JAX #026105)(12-15 months old) were obtained from the Jackson Laboratory and maintained at the Yale animal facility.
Wild animals	No wild animals were used.
Reporting on sex	Both sex of male and female animals have been used for proteomics analysis (3 male and 3 female mice).
Field-collected samples	No field-collected samples were used.
Ethics oversight	Yale University IACUC 2023-11438.

Note that full information on the approval of the study protocol must also be provided in the manuscript.

Plants

Seed stocks	n/a
Novel plant genotypes	n/a
Authentication	n/a